

CONSTITUTIVE MODELS FOR POLYMERS AND SOFT BIOLOGICAL TISSUES

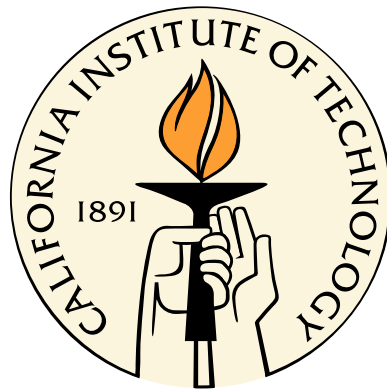
Thesis by

Tamer Magdy El Sayed

In Partial Fulfillment of the Requirements

for the Degree of

Doctor of Philosophy



California Institute of Technology

Pasadena, California

2008

(Defended October 8, 2007)

© 2008

Tamer Magdy El Sayed

All Rights Reserved

To Yara.

Acknowledgments

A few years ago, I would have never thought that I could end up at one of the world's finest academic institutions, nevertheless earn the highest attainable degree from that very same place. For that, I would like to thank God for guiding me through the adversities of life prior to my arrival at Caltech. It is indeed true that whatever does not break you, only makes you stronger.

On a different note, this work would not have been possible without the guidance and supervision of my advisor, Professor Michael Ortiz, whom I started to work with four years ago by mere coincidence and only later realized how lucky I was to be in such good hands. His constant support and encouragement have been a driving force in the course of this work.

I want to thank Professor Guruswami Ravichandran, Professor Kaushik Bhattacharya, and Professor Chiara Daraio for agreeing to serve on my thesis committee, especially Professor Ravichandran for providing me with advice over the past four years on how to reach this point of my academic career.

Many people apart from my advisor have contributed to my advancement throughout my graduate studies at Caltech. First and utmost, Dr. Alejandro Mota; my interactions with him have increased my knowledge and driven me to achieve my best. His patience and availability to answer all of my questions, no matter how minor, have been a cornerstone in my ability to produce this work. He is truly an amazing colleague and a remarkable friend.

Also, I must thank Professor Fernando Fraternali, whose enthusiasm and cheerful personality have made our collaboration fruitful and enjoyable. He is certainly a unique person whose company I truly enjoyed in both professional and social settings.

I am also indebted to Dr. Fehmi Cirak, who was the first person I collaborated with at Caltech. He contributed a great deal to enhancing my research tools, which I utilized during my graduate studies and will continue to use for the rest of my professional career.

I would like to thank the Office of Naval Research (ONR) for the invaluable financial support of this work. I am also grateful to Professor Sia Nemat-Nasser and Ali Amirkhizi from UCSD; Mike Roland from the Naval Research Laboratory, Washington, D.C., for providing the polyurea experimental data; Professor Franceschini and Professor Bigoni for their indispensable brain experimental data; and Bill Mock, Jr., from the research gas gun facility at the Naval Surface Warfare Center (Dahlgren Division) for providing the composite plate shot experimental data, and Luigi Perotti for his help in the collection of the PVC H100 foam data.

I would like to thank Tomonori Honda, Rick Burns, and Vaughan Thomas for the good times we spent together at Caltech. I will forever cherish our friendship.

I would like to sincerely thank Lydia Suarez and Marta Kahl for providing crucial administrative and technical help essential to my studies. Lydia has been a voice of wisdom on matters just as important as my doctoral research.

Last, but not least, I am grateful to my wife Sarai for providing me with the peace and tranquility I so desperately needed during my stressful first year at Caltech, and for giving me our beautiful daughter Yara, whose smile has always lifted my spirits.

Abstract

Soft materials such as polymers and biological tissues have several engineering and biomechanical applications. These materials exhibit complex mechanical behavior, characterized by large strains, hysteresis, rate sensitivity, stress softening (*Mullins effect*), and deviatoric and volumetric plasticity. The need to accurately predict the behavior of such materials has been a tremendous challenge for scientists and engineers.

This thesis presents a seamless, fully variational constitutive model capable of capturing all of the above complex characteristics. Also, this work describes a fitting procedure based on the use of Genetic Algorithms, which proves to be necessary for the multi-modal, non-convex optimization required to identify fitting material parameters.

The capabilities of the presented model are demonstrated via several fits of experimental tests on a wide range of materials. These tests involve monotonic and cyclic loading of polyurea, high-density polyethylene, and brain tissue, and also involve cyclic hysteresis, softening, rate effects, shear, and cavitation plasticity.

Application to ballistic impact on a polyurea retrofitted DH36 steel plate is simulated and validated, utilizing the soft material model presented in this thesis for the polymer and a porous plasticity model for the metal. Localization elements are also included in this application to capture adiabatic shear bands. Moreover, computational capability for assessing the blast performance of metal/elastomer composite shells utilizing the soft material model for the elastomer is also presented.

Another implemented application is in the area of traumatic brain injuries under impact/acceleration loading. Clinically observed brain damage is reproduced utilizing the model presented in this work and a predictive capability of the distribution, intensity, and

reversibility/irreversibility of brain tissue damage is demonstrated.

Contents

Acknowledgments	iv
Abstract	vi
1 Introduction	1
2 Model formulation	5
2.1 Free energy	5
2.2 Ogden-type hyperelasticity	6
2.3 Deviatoric and volumetric plasticity	8
2.3.1 Deviatoric plasticity	9
2.3.2 Volumetric plasticity	9
2.4 Thermodynamic forces	11
2.5 Evolution laws—Rate effects	12
2.6 Microinertia	13
2.7 Variational formulation of the rate problem	14
2.8 Incremental constitutive updates	16
2.9 Predictor-corrector implementation	17
2.10 Stress update	20
3 Validation	22
3.1 Parameter identification	22
3.2 High strain rate compression tests on polyurea	24

3.3	Tension tests on polyurea	33
3.4	Tensile tests on high-density polyethylene	37
3.5	Monotonic and cyclic uniaxial tests on brain tissue	42
4	Application to ballistic and blast impact on composite plates and shells	51
4.1	Introduction	51
4.2	Ballistic impact on composite plates	53
4.2.1	Localization elements	53
4.2.2	Modeling contact forces	54
4.2.3	Composite plate shot experimental setup	57
4.2.4	Validation	59
4.3	Blast impact on composite shells	70
4.3.1	Subdivision thin-shell elements	70
4.3.2	Shell fracture and fragmentation	71
4.3.3	DH36 steel/Polyurea composite hull	72
4.3.4	Aluminum/PVC foam H100/Aluminum composite hull	77
4.3.5	PVC foam - Divinycell H100	78
5	Application to brain trauma	89
5.1	Introduction	89
5.2	Finite element model of the human head	92
5.3	Impact simulations	97
5.3.1	Frontal impact	97
5.3.2	Oblique impact	105
6	Conclusions	113
6.1	Summary	113
6.2	Outlook	114
6.2.1	Polymeric applications	114
6.2.2	Medical applications	115

6.2.3	Neuromuscular applications	116
6.3	A concluding remark	117
	Bibliography	118

List of Figures

3.1	Alireza et al. experimental confined compression curves [5] vs. GAs fits. Fitting curves correspond to one set of material parameters (cf. Tab. 3.1).	30
3.2	Alireza et al. experimental unconfined compression curves [5] vs. GAs fits. Fitting curves correspond to one set of material parameters (cf. Tab. 3.1).	32
3.3	Tension tests on polyurea. Cauchy stress vs. true strain (all corrected for inertial forces), with the corresponding strain rates as indicated. The model Cauchy stresses are also shown for the same strain rates.	36
3.4	SEM observation of cavitation mechanisms in HDPE during plastic deformation (tensile axis is vertical). Interspherulitic decohesion for $\epsilon_{33r} = 0.71$ (axial residual strain) [4]	40
3.5	Predicted and experimental axial stress-axial strain curves for a tensile uniaxial test by [4] on high-density polyethylene (strain rate: $\dot{\epsilon} = 0.001\text{s}^{-1}$)	40
3.6	Total experimental volumetric strain in HDPE [4] used as input and model volumetric plastic strain-axial strain. The difference between the curves is the volumetric elastic strain. This shows the ability of the model to distinguish between elastic and plastic volumetric strain (strain rate: $\dot{\epsilon} = 0.001\text{s}^{-1}$).	41
3.7	Illustration of the uniaxial tests on short cylindrical samples of brain tissue by [57]	42
3.8	Independent tension-compression viscoelastic fits of experiments in [57]	44
3.9	Global viscoelastic (ve) and viscoelastic/elastoplastic (ve/ep) fits of experiments in [57]	46

3.10 Fits of Franceschini et al. one-cycle compression-tension (a) and tension-compression (b) tests on specimens of white matter (cf. [30], Fig. 1) 49

3.11 Fits of Franceschini et al. cyclic tests on a specimen of white matter (cf. [30], Fig. B.3, first three cycles) 50

4.1 Localization surface in a three-dimensional body. S^+ and S^- are the top and bottom (smooth) surface of band attached to the sub-body B^+ and B^- , respectively. T is the traction acting on the mid-surface S 53

4.2 Naval Surface Warfare Center (Dahlgren Division) Research Gas Gun Facility (Courtesy of Bill Mock et al. [60]) 57

4.3 Impactor (right) about to strike target composite plate (left) 58

4.4 Polyurea release wave experiment set up by Clifton et al. [22] 59

4.5 Microstructure of the damaged area in polyurea as a result of the release wave experiment [22] 60

4.6 T-x diagram of the release wave experiment [22] 60

4.7 Free surface normal velocity vs. time [22] 61

4.8 Composite plate positions at different times. Each color/symbol represents a time frame. 65

4.9 Experimental and computational displacements at various times 66

4.10 Experimental (top) and computational (bottom) final configurations 67

4.11 Plastic strain (a), volumetric strain (b), and temperature (c) contour plots from the impact side of the composite plate 68

4.12 Plastic strain (a), volumetric strain (b), and temperature (c) contour plots across the thickness of the composite plate 69

4.13 Support of shape functions of a subdivision element (central triangle) 70

4.14 One cohesive edge and the two adjacent subdivision shell elements with their one-neighborhoods 72

4.15 Composite shell formulation 73

4.16 Hull mesh (2880 elements) 74

4.17	Hull front, side, and dimetric views (top to bottom)	75
4.18	Composite hull views during blast impact. Views are front (a) and side (b).	76
4.19	Hull kinetic energy vs. time for different configurations	77
4.20	Composite shell formulation	78
4.21	Cells structure of Divinycell H45 (top) and H130 (bottom)[7]	79
4.22	Photographs of a specimen of H200 foam sectioned along its mid-plane. Views are undeformed and uniaxially compressed to 10% from left to right.[25]	79
4.23	Foam uniaxial compressive behavior	80
4.24	Schematic uniaxial stress-strain curve for Divinycell H100	81
4.25	Variation of peak stress with foam density from quasi-static to high strain rate [86]	84
4.26	Coarse (a,b,c) and fine (d,e,f) hulls during blast impact. Views are front (a,d), back (b,e), and side (c,f).	87
4.27	Shell kinetic energy vs. time for different configurations	88
5.1	Coup-contrecoup injury (adapted from Kleiven [46])	90
5.2	Mid-sagittal and mid-coronal sections of the adopted head finite element model: (1) skull without facial bones; (2) CSF; (3) gray matter; (4) white matter; (5) cerebellum; (6) corpus callosum; (7) telencephalic nuclei; (8) brain stem; (9) ventricles.	94
5.3	Frontal impact injury	98
5.4	Animation of the translational head motion following frontal impact ($t =$ 2, 4, 6, 8 ms)	98
5.5	Predicted vs. experimental intracranial pressure time-histories (Nahum et al. [63], experiment no. 37)	99
5.6	Frontal impact: intracranial pressure contours (Pa)	101
5.7	Frontal impact: cavitation damage predictions	102
5.8	Frontal impact: shear stress contours (Pa)	104
5.9	Frontal impact: viscous shear deformation predictions	105

5.10	Oblique impact injury	106
5.11	Animation of the translational-rotational head motion following oblique im- pact ($t = 2, 4, 5, 6, 7, 8$ ms)	106
5.12	Oblique impact: intracranial pressure contours (Pa)	107
5.13	Oblique impact: cavitation damage predictions	108
5.14	Oblique impact: shear stress contours (Pa)	110
5.15	Oblique impact: permanent shear damage predictions	111
5.16	Oblique impact: viscous shear deformation predictions	112

List of Tables

3.1	GAs material parameter estimates for UCSD compression tests on polyurea [5]	32
3.2	Model parameter estimates for tension tests on polyurea at various strain rates	37
3.3	GAs material parameter estimates for a tensile uniaxial test in [4] on high-density polyethylene (strain rate: $\dot{\epsilon} = 0.001\text{s}^{-1}$)	39
3.4	GAs material parameter estimates for monotonic tests on brain tissue in [57]	45
3.5	GAs material parameter estimates for [30] tests on specimens of brain white matter	48
4.1	Shot parameters	58
4.2	Material parameter estimates for release wave experiment on polyurea [22]	62
4.3	Material parameter estimates for DH36 steel via fits to data in [64]	64
4.4	Thermal parameter estimates for polyurea	64
4.5	DH36 steel and polyurea fracture parameters	74
4.7	Soft material model parameter estimates for PVC H100 foam	82
4.6	Divinycell H100 material properties	82
4.8	Material parameters for aluminum	83
4.9	Aluminum and PVC H100 fracture parameters	83
5.1	Soft tissue material properties. GM = Gray Matter; WM = White Matter; BSCC = Brain Stem and Corpus Callosum	96
5.2	Skull and CSF properties	97

Chapter 1

Introduction

Phenomenological modeling which describes the behavior of a particular material by adapting mathematical equations to experimental data has been a cornerstone in computational solid mechanics. Concerned with capturing the macroscopic behavior, this type of modeling has been most effective in describing the response of a wide range of materials. On their own, however, the fundamental phenomenological equations are incapable of determining how a specific material behaves under both static and dynamic loading [40], and therefore, the need for more effective and general constitutive equations arises.

Many materials of relevant interest for engineering and biomechanical applications exhibit a complex mechanical behavior, characterized by large strains, hysteresis, rate-sensitivity, stress softening (*Mullins effect*), and deviatoric and volumetric plasticity.

In thermoplastic polyurethanes (TPUs), for instance, the periodic repetition of hard and soft microstructures determines a morphological complex phase separation that is responsible for a multi-faceted macroscopic behavior combining elastic, viscous, and plastic responses. One example is the macroscopic behavior of the elastomer thermoset polyurea [99, 80], which is currently being assessed together with TPUs for retrofitting steel structures.

By contrast, in amorphous polymers—typically used to form impact-resistant components (helmets, eyeglasses, shatterproof glass, etc.)—intramolecular resistance to chain-segment rotation due to rate-activated molecular motions contributes to the macroscopic

response together with chain-alignment resistance. In these materials, the yield transition is experimentally found to be rate and temperature dependent [62].

Boyce et al. [80] have recently proposed constitutive models for thermoplastic polymers that decompose the material behavior into a rate-independent equilibrium part and a collection of rate-dependent viscoelastic-plastic parts [80, 62]. The first accounts for chain-alignment resistance and Mullins effect, while the second describes hard domain deformation (TPUs) or intramolecular resistance (glassy polymers). Furthermore, viscoelastic modeling of polyurea based on experimental observations has recently been proposed by [5], and several combinations of rheological models have been considered by [52] to describe strain-rate effects in inelastic polymeric materials. Also, variationally consistent finite viscoelastic models have been proposed by [34], [81], and [28].

Mullins effect, hysteresis, and residual strain are also characteristics of particle-reinforced rubbers, such as carbon-black filled elastomers used in vehicle tires, vibration isolators, earthquake bearings, and other engineering components. Several authors have modeled this behavior through suitable damage theories [36, 35, 66, 26]. In addition, time-dependent multi-network approaches have been proposed by [8] and [9].

Some glassy and amorphous polymers exhibit *crazing*, i.e., the formation of microvoids in yielding regions, which can grow and coalesce and lead to the nucleation of cracks [77, 61]. In crystalline or semi-crystalline polymers such as polypropylene and high-density polyethylene, shear yielding is instead accompanied by cavitation, either below or above the glass transition temperature. This phenomenon (volumetric plasticity) is visible as whitening at the macroscale, under tensile uniaxial loadings (*micronecking*) or hydrostatic tensile stresses. Cavitation has recently received the attention of several research groups ([77, 61, 4] and references therein).

Likewise, soft biological tissues exhibit complex mechanical behavior, and have been the subject of intensive research in engineering, physics, biology, medicine, and applied mathematics (refer to [41] for a research overview in the field). One important example is brain tissue, which exhibits extremely soft behavior and is often modeled using hyperelas-

tic or hyperviscoelastic constitutive equations [79, 56, 57, 58, 54, 11, 10, 91]. Plasticity, hysteresis, permanent deformation, and biphasic (solid/fluid) behavior of soft biological tissues have been analyzed by [9], [32], and [30].

Taking into account all of the previously mentioned requirements in the modeling of soft materials, herein this thesis presents a fully variational constitutive model with the ability to capture all of the following:

- Void growth and shrinkage during the process of cavitation
- Rate and microinertia effects
- Complex viscous behavior via a flexible number of viscoelastic mechanisms capable of representing finite viscosity
- Hysteresis, strong non-linearity, different behavior in tension and compression, pre-conditioning, and cyclic softening
- Thermal softening and adiabatic heating via thermal updates.

By virtue of a multiple multiplicative decomposition of the deformation gradient, the rheological representation of the model consists of an elastoplastic network acting in parallel with several viscoelastic networks. Quasi-incompressible Ogden-type potentials govern the elastic behavior, both in the elastoplastic (which accounts for both deviatoric and volumetric plasticity) and viscoelastic branches. Cyclic stress softening is reproduced through a combination of elastoplastic and viscoelastic responses, while volumetric plasticity is related to the expansion of spherical voids or bubbles in a plastically incompressible matrix. As the pressure reaches a critical value in tension, the material is allowed to yield and exhibit volumetric strain softening. Microinertia due to expanding bubbles is also taken into account [70, 95, 94].

The number of model parameters is a function of the number of active Ogden terms and relaxation mechanisms, and therefore a significant number of variables may need to be identified. This requires the use of advanced techniques for the calibration of model

parameters based on experimental data, hence this thesis proposes a procedure based on Genetic Algorithms, which have been proven to be well-suited for multimodal nonconvex optimization [87]. Several sets of experimental data are compared with model predictions, showing the ability of the model to reproduce the observed behavior of polymers and soft biological tissues. Monotonic and cyclic tests on polyurea, high-density polyethylene, and brain tissue, which involve complex behavior such as cyclic hysteresis, cyclic softening, rate effects, shear, and cavitation plasticity are examined.

The order of presentation of topics within this thesis is as follows: The formulation of the constitutive model of polymers and soft biological tissues is presented in Chapter 2. Chapter 3 describes a fitting procedure based on the use of Genetic Algorithms, which are useful for multimodal nonconvex optimization. Several carefully chosen fits of experimental tests are presented in order to demonstrate the model's versatility in reproducing complex behavior of polymers and soft biological tissues. Monotonic and cyclic tests on polyurea, high-density polyethylene, and brain tissue are examined. These tests involve cyclic hysteresis, softening, rate effects, shear, and cavitation plasticity. In chapter 4, application to ballistic impact on a polyurea retrofitted composite plate is simulated and validated, utilizing the soft material model presented in this thesis for the polymer and a porous plasticity model for the metal. Moreover, computational capability for assessing the blast performance of metal/elastomer composite shells is also presented. An underwater blast load on a composite hull is simulated by assigning the proper model, material properties, and cohesive law to the corresponding metal/polymer across-the-thickness integration points. In Chapter 5, the simulation of axonal damage due to head injury through shearing plastic deformation, and focal damage through the volumetric plastic deformation induced by the *tension tail* of an impact wave is demonstrated. Finally, in Chapter 6, conclusions are drawn from the findings in the previous chapters, with recommendations about possible future directions.

Chapter 2

Model formulation

2.1 Free energy

Let \mathbf{F} denote the deformation gradient at an arbitrary point of the material, and let

$$\mathbf{F} = \mathbf{F}^e \mathbf{F}^p = \mathbf{F}_1^e \mathbf{F}_1^v = \dots = \mathbf{F}_M^e \mathbf{F}_M^v \quad (2.1)$$

be its multiple multiplicative decomposition, where M is a positive integer that defines the number of viscoelastic (Maxwell-type) relaxation networks that the model possesses, which act in parallel with an elastoplastic equilibrium network; \mathbf{F}^e , \mathbf{F}_1^e , ..., \mathbf{F}_M^e are the elastic parts of \mathbf{F} ; \mathbf{F}^p is the plastic deformation gradient; and \mathbf{F}_1^v , ..., \mathbf{F}_M^v are the viscous deformation gradients.

The thermo-mechanical behavior of the material derives from the additive potential

$$A = A^{ep}(\mathbf{F}, \mathbf{F}^p, \mathbf{Z}^p, T) + A^{ve}(\mathbf{F}, \mathbf{F}_i^v, \mathbf{Z}_i^v), \quad (2.2)$$

where A^{ep} and A^{ve} are elastoplastic and viscoelastic contributions, correspondingly; \mathbf{Z}^p is a vector of plastic internal variables; \mathbf{Z}_i^v are vectors of viscous internal variables ($i = 1, \dots, M$); and T is the absolute temperature.

The first Piola-Kirchhoff stress \mathbf{P} , and the thermodynamic forces \mathbf{Y}^p and \mathbf{Y}_i^v conjugate

to \mathbf{Z}^p and \mathbf{Z}_i^v follow from

$$\mathbf{P} = \frac{\partial A}{\partial \mathbf{F}}, \quad (2.3)$$

$$\mathbf{Y}^p = - \frac{dA}{d\mathbf{Z}^p}, \quad (2.4)$$

$$\mathbf{Y}_i^v = - \frac{dA}{d\mathbf{Z}_i^v}. \quad (2.5)$$

The free energy is assumed to have the additive structure

$$\begin{aligned} A^{ep}(\mathbf{F}, \mathbf{F}^p, \mathbf{Z}^p, T) + A^{ve}(\mathbf{F}, \mathbf{F}_i^v, \mathbf{Z}_i^v) = \\ W^e(\mathbf{F}\mathbf{F}^{p-1}, T) + W^p(\mathbf{Z}^p, T) + \sum_{i=1}^M W_i^e(\mathbf{F}\mathbf{F}_i^{v-1}, T) + \rho_0 C_v T \left(1 - \log \frac{T}{T_0}\right), \end{aligned} \quad (2.6)$$

where W^e is the elastic strain-energy density associated with the elastoplastic branch; W^p is the plastic stored energy; $W_i^e (i = 1, \dots, M)$ are the elastic strain-energy densities corresponding to the viscous relaxation mechanisms; ρ_0 is the mass density per unit undeformed volume; C_v is the specific heat per unit mass at constant volume and T_0 is the reference temperature.

The internal variables \mathbf{F}^p , \mathbf{Z}^p and \mathbf{F}_i^v , \mathbf{Z}_i^v are closely related to each other by the means of suitable differential equations or *flow rules* to be introduced later.

2.2 Ogden-type hyperelasticity

It is assumed that the elastic strain energies admit a decomposition into deviatoric and volumetric parts. Furthermore, it proves convenient for the constitutive updates to introduce

the logarithmic elastic strain measures

$$\boldsymbol{\epsilon}^e = \frac{1}{2} \log(\mathbf{F}^{eT} \mathbf{F}^e) = \frac{1}{2} \log(\mathbf{F}^{p-T} \mathbf{C} \mathbf{F}^{p-1}), \quad (2.7)$$

$$\boldsymbol{\epsilon}_i^e = \frac{1}{2} \log(\mathbf{F}_i^{eT} \mathbf{F}_i^e) = \frac{1}{2} \log(\mathbf{F}_i^{v-T} \mathbf{C} \mathbf{F}_i^{v-1}), \quad (2.8)$$

$$\mathbf{e}^e = \text{dev}(\boldsymbol{\epsilon}^e), \quad \theta^e = \text{tr}(\boldsymbol{\epsilon}^e), \quad (2.9)$$

$$\mathbf{e}_i^e = \text{dev}(\boldsymbol{\epsilon}_i^e), \quad \theta_i^e = \text{tr}(\boldsymbol{\epsilon}_i^e), \quad (2.10)$$

where \mathbf{C} is the right Cauchy-Green deformation tensor ($\mathbf{C} = \mathbf{F}^T \mathbf{F}$), and $\text{dev}(\cdot)$ and $\text{tr}(\cdot)$ are the deviator and the trace operators, respectively. Thus, the elastic strain energy density decompositions are

$$W^e(\boldsymbol{\epsilon}^e, T) = W^{e,\text{vol}}(\theta^e, T) + W^{e,\text{dev}}(\mathbf{e}^e, T), \quad (2.11)$$

$$W_i^e(\boldsymbol{\epsilon}_i^e, T) = W_i^{e,\text{vol}}(\theta_i^e, T) + W_i^{e,\text{dev}}(\mathbf{e}_i^e, T), \quad (2.12)$$

with

$$W^{e,\text{vol}}(\theta^e, T) = \frac{\kappa}{2} [\theta^e - \alpha(T - T_0)]^2, \quad (2.13)$$

$$W^{e,\text{dev}}(\mathbf{e}^e, T) = \sum_{j=1}^3 \sum_{n=1}^N \frac{\mu_n}{\alpha_n} ([\exp(e_j^e)]^{\alpha_n} - 1), \quad (2.14)$$

$$W_i^{e,\text{vol}}(\theta_i^e, T) = \frac{\kappa_i}{2} (\theta_i^e)^2, \quad (2.15)$$

$$W_i^{e,\text{dev}}(\mathbf{e}_i^e, T) = \sum_{j=1}^3 \sum_{n=1}^{N_i} \frac{\mu_{i,n}}{\alpha_{i,n}} ([\exp(e_{i,j}^e)]^{\alpha_{i,n}} - 1). \quad (2.16)$$

In (2.11)–(2.16), κ and κ_i ($i = 1, \dots, M$) are bulk moduli; μ_n and $\mu_{i,n}$ are shear moduli associated with the Ogden potentials [68] adopted for deviatoric elasticity; α_n and $\alpha_{i,n}$ are dimensionless real parameters; N is the number of Ogden-terms considered for the time-infinity behavior; N_i is the number of Ogden-terms selected for the i th relaxation mechanism; and e_j^e and $e_{i,j}^e$ ($j = 1, 2, 3$) are the eigenvalues of \mathbf{e}^e and \mathbf{e}_i^e , respectively.

Polyconvexity of the Ogden models requires (cf. [6, 18]):

$$\mu_n \alpha_n > 0, \quad |\alpha_n| > 1 \quad \forall n = 1, \dots, N, \quad (2.17)$$

$$\mu_{i,n} \alpha_{i,n} > 0, \quad |\alpha_{i,n}| > 1 \quad \forall n = 1, \dots, N_i; \quad \forall i = 1, \dots, M. \quad (2.18)$$

For convenience, let

$$\mu^0 = \frac{1}{2} \left(\sum_{n=1}^N \mu_n \alpha_n + \sum_{i=1}^M \sum_{n=1}^{N_i} \mu_{i,n} \alpha_{i,n} \right), \quad (2.19)$$

$$\mu^\infty = \frac{1}{2} \sum_{n=1}^N \mu_n \alpha_n, \quad (2.20)$$

denote the consistent shear moduli in the small strain regime, which correspond to initial and long-term behaviors, respectively.

2.3 Deviatoric and volumetric plasticity

The plastic stored energy is also assumed to admit an additive decomposition into volumetric and deviatoric parts as

$$W^p(\mathbf{Z}^p, T) = W^{p,\text{vol}}(\theta^p, T) + W^{p,\text{dev}}(\epsilon^p, T), \quad (2.21)$$

where

$$\mathbf{Z}^p = \{\theta^p, \epsilon^p\}, \quad (2.22)$$

in which $\theta^p \geq 0$ and $\epsilon^p \geq 0$ are effective volumetric and deviatoric plastic strains, respectively. The flow rule that relates \mathbf{Z}^p and \mathbf{F}^p is assumed to be

$$\dot{\mathbf{F}}^p \mathbf{F}^{p-1} = \dot{\theta}^p \mathbf{N}^p + \dot{\epsilon}^p \mathbf{M}^p, \quad (2.23)$$

where \mathbf{M}^p and \mathbf{N}^p are second-order tensors subject to the normality constraints

$$\text{tr}(\mathbf{M}^p) = 0, \quad \mathbf{M}^p \cdot \mathbf{M}^p = \frac{3}{2}, \quad \mathbf{N}^p = \pm \frac{1}{3} \mathbf{I}. \quad (2.24)$$

with the following irreversibility of plastic flow requirements

$$\dot{\epsilon}^p \geq 0, \quad \dot{\theta}^p \geq 0. \quad (2.25)$$

2.3.1 Deviatoric plasticity

The deviatoric plastic behavior is modeled via the hardening power law

$$W^{p,\text{dev}}(\epsilon^p, T) = \frac{n \sigma_0(T) \epsilon_0^p}{n+1} \left(1 + \frac{\epsilon^p}{\epsilon_0^p} \right)^{\frac{n+1}{n}}, \quad (2.26)$$

where n is the hardening exponent, $\sigma_0(T)$ is the yield stress, and ϵ_0^p is the reference deviatoric plastic strain. Furthermore, the yield stress is assumed to be a function of temperature

$$\sigma_0(T) = \sigma_0(T_0) \left(1 - \frac{T - T_0}{T_m - T_0} \right)^l, \quad (2.27)$$

where T_0 is the reference temperature, T_m is the melting temperature and l is the thermal softening exponent.

2.3.2 Volumetric plasticity

The volumetric plastic behavior is assumed to be related to the expansion or collapse of spherical voids in a plastically incompressible matrix [70, 94, 95]. The initial void volume fraction of the body in the undeformed configuration is given by

$$f_0 = N_v \frac{4\pi a_0^3}{3}, \quad (2.28)$$

where N_v is the void density (number of voids per unit undeformed volume); and a_0 is the initial void radius.

Neglecting the elastic volume change of the voids, the plastic volumetric deformation can be expressed as a function of the void radius

$$J^p = 1 - f_0 + N_v \frac{4\pi a^3}{3}, \quad f = \frac{f_0 + J^p - 1}{J^p}, \quad (2.29)$$

where J^p is the determinant of \mathbf{F}^p , and a is the void radius in the deformed configuration. For purely volumetric deformations the flow rule (2.23) becomes

$$\frac{d}{dt} \log J^p = \text{tr}(\mathbf{N}^p) \dot{\theta}^p = \pm \dot{\theta}^p, \quad (2.30)$$

and hence implies

$$\dot{\theta}^p = \left| \frac{d}{dt} \log J^p \right|, \quad (2.31)$$

which in turn means that the internal variable θ^p represents a measure of the accumulated volumetric plastic deformation. By introducing the expression of the stored energy of a single spherical void in a power-law hardening material [70], and integrating the energies stored by each void (*dilute limit*), the following is obtained:

$$W^{p,\text{vol}}(\theta^p, T) = \frac{n \sigma_0(T) \epsilon_0^p}{n+1} N_v \frac{4\pi a^3}{3} g(\theta^p, n), \quad (2.32)$$

where

$$g(\theta^p, n) = \int_1^{1/f} \left(1 + \frac{2}{3\epsilon_0^p} \log \frac{x}{x-1 + \frac{f_0}{f_0 + \exp \theta^p - 1}} \right)^{\frac{n+1}{n}} dx. \quad (2.33)$$

2.4 Thermodynamic forces

Let \mathbf{T}^p and $\mathbf{Y}^p = \{Y^p, Z^p\}$ denote the thermodynamic forces conjugate to \mathbf{F}^p and $\mathbf{Z}^p = \{\theta^p, \epsilon^p\}$, respectively, which are obtained by applying the chain rule in (2.4), as follows

$$\mathbf{T}^p = -\frac{\partial A}{\partial \mathbf{F}} \cdot \frac{\partial \mathbf{F}}{\partial \mathbf{F}^p} - \frac{\partial A}{\partial \mathbf{F}^p} = \mathbf{F}^{eT} \mathbf{P} - A_{,\mathbf{F}^p}, \quad (2.34)$$

$$Y^p = p - p_c, \quad Z^p = \sigma - \sigma_c, \quad (2.35)$$

where

$$p = -\frac{dA}{d\theta^p} = \mathbf{T}^p \cdot \mathbf{N}^p \mathbf{F}^p, \quad p_c = \frac{\partial A}{\partial \theta^p}, \quad (2.36)$$

$$\sigma = -\frac{dA}{d\epsilon^p} = \mathbf{T}^p \cdot \mathbf{M}^p \mathbf{F}^p, \quad \sigma_c = \frac{\partial A}{\partial \epsilon^p}, \quad (2.37)$$

and in which p and σ are the effective pressure and the effective deviatoric stress, respectively; and p_c and σ_c are the flow pressure and the deviatoric flow stress, respectively. Substituting (2.6), (2.11), and (2.21) in (2.36) and (2.37) the following is obtained:

$$p = -\frac{dA}{d\theta^p} = -\frac{\partial W^{e,\text{vol}}}{\partial \theta^e}, \quad p_c = \frac{\partial W^{p,\text{vol}}}{\partial \theta^p}, \quad (2.38)$$

$$\sigma = -\frac{dA}{d\epsilon^p} = -\frac{\partial W^{e,\text{dev}}}{\partial e^e}, \quad \sigma_c = \frac{\partial W^{p,\text{dev}}}{\partial \epsilon^p}, \quad (2.39)$$

where $e^e = \sqrt{\frac{2}{3} \mathbf{e}^e \cdot \mathbf{e}^e}$.

It is assumed that there exists a *viscous flow rule* that takes the form

$$\dot{\mathbf{F}}_i^v \mathbf{F}_i^{v-1} = \sum_{j=1}^3 \dot{\epsilon}_{i,j}^v \mathbf{M}_{i,j}^v \otimes \mathbf{M}_{i,j}^v \quad (i = 1, \dots, M), \quad (2.40)$$

where $\dot{\epsilon}_{i,j}^v$ and $\mathbf{M}_{i,j}^v$ are the eigenvalues and the eigenvectors of $\mathbf{d}_i^v = \dot{\mathbf{F}}_i^v \mathbf{F}_i^{v-1}$, respectively (null viscous spin is assumed). The viscous internal variables are

$$\mathbf{Z}_i^v = \{\epsilon_{i,1}^v, \epsilon_{i,2}^v, \epsilon_{i,3}^v\}, \quad (2.41)$$

where

$$\epsilon_{i,j}^v = \epsilon_{i,j}^v(0) + \int_0^t \dot{\epsilon}_{i,j}^v(\xi) d\xi. \quad (2.42)$$

The viscous driving forces $\mathbf{Y}_i^v = \{\sigma_{i,1}^v, \sigma_{i,2}^v, \sigma_{i,3}^v\}$ follow from (2.5) and the chain rule as

$$\sigma_{i,j}^v = -\frac{dA}{d\epsilon_{i,j}^v} = \mathbf{T}_i^v \cdot \mathbf{M}_{i,j}^v \mathbf{F}_i^v. \quad (2.43)$$

Substituting (2.6), (2.12) in (2.43), the viscous principal stresses are obtained as

$$\sigma_{i,j}^v = -\frac{dA}{d\epsilon_{i,j}^v} = -\frac{\partial W_i^e}{\partial e_{i,j}^e}. \quad (2.44)$$

Isochoric viscous deformations may be obtained by enforcing the constraint $\dot{\theta}_i^v = \dot{\epsilon}_{i,1}^v + \dot{\epsilon}_{i,2}^v + \dot{\epsilon}_{i,3}^v = 0$ (cf. [28]), while the purely elastic bulk behavior may be obtained by setting the volumetric viscosities to zero.

2.5 Evolution laws—Rate effects

Evolution laws for the internal variables are obtained variationally by assuming the existence of differentiable kinetic potentials $\psi(\mathbf{Y}^p, \mathbf{F}^p, T)$ and $\phi_i(\mathbf{Y}_i^v, \mathbf{F}_i^v, T)$ such that

$$\dot{\mathbf{Z}}^p = \frac{\partial \psi}{\partial \mathbf{Y}^p}, \quad \dot{\mathbf{Z}}_i^v = \frac{\partial \phi_i}{\partial \mathbf{Y}_i^v} \quad (i = 1, \dots, M). \quad (2.45)$$

The dual kinetic potentials $\psi^*(\mathbf{F}^p, \dot{\mathbf{Z}}^p, T)$, $\psi_i^*(\mathbf{F}_i^v, \dot{\mathbf{Z}}_i^v, T)$ are introduced via the Legendre transformations

$$\psi^*(\mathbf{F}^p, \dot{\mathbf{Z}}^p, T) = \sup_{\mathbf{Y}^p} \left\{ \mathbf{Y}^p \cdot \dot{\mathbf{Z}}^p - \psi(\mathbf{Y}^p, \mathbf{F}^p, T) \right\}, \quad (2.46)$$

$$\phi_i^*(\mathbf{F}_i^v, \dot{\mathbf{Z}}_i^v, T) = \sup_{\mathbf{Y}_i^v} \left\{ \mathbf{Y}_i^v \cdot \dot{\mathbf{Z}}_i^v - \phi(\mathbf{Y}_i^v, \mathbf{F}_i^v, T) \right\} \quad (i = 1, \dots, M), \quad (2.47)$$

that in turn satisfy

$$\mathbf{Y}^p = \frac{\partial \psi^*}{\partial \dot{\mathbf{Z}}^p}, \quad \mathbf{Y}_i^v = \frac{\partial \phi_i^*}{\partial \dot{\mathbf{Z}}_i^v}. \quad (2.48)$$

The dual kinetic potentials may also be decomposed into deviatoric and volumetric components

$$\psi^*(\mathbf{F}^p, \dot{\mathbf{Z}}^p, T) = \psi^{*,\text{vol}}(J^p, \dot{\theta}^p, T) + \psi^{*,\text{dev}}(\dot{\epsilon}^p, T), \quad (2.49)$$

$$\phi_i^*(\mathbf{F}_i^v, \dot{\mathbf{Z}}_i^v, T) = \phi_i^{*,\text{vol}}(\dot{\theta}_i^v, T) + \phi_i^{*,\text{dev}}(\dot{\epsilon}_i^v, T), \quad (2.50)$$

where

$$\psi^{*,\text{vol}}(J^p, \dot{\theta}^p, T) = \frac{m^2 \sigma_0(T) \dot{\epsilon}_0^p}{m+1} N_v \frac{4\pi a^3}{3} \left(1 - f^{\frac{1}{m}}\right) \left| \frac{2\dot{a}}{\dot{\epsilon}_0^p a} \right|^{\frac{m+1}{m}}, \quad (2.51)$$

$$\psi^{*,\text{dev}}(\dot{\epsilon}^p, T) = \frac{m^2 \sigma_0(T) \dot{\epsilon}_0^p}{m+1} \left(\frac{\dot{\epsilon}^p}{\dot{\epsilon}_0^p} \right)^{\frac{m+1}{m}}, \quad (2.52)$$

$$\phi_i^{*,\text{vol}}(\dot{\theta}_i^v, T) = \frac{\eta_i^{\text{vol}}}{2} \dot{\theta}_i^v{}^2, \quad (2.53)$$

$$\phi_i^{*,\text{dev}}(\dot{\epsilon}_i^v, T) = \sum_{j=1}^3 \sum_{n=1}^{N_i} \frac{\eta_{i,n}^{\text{dev}}}{\alpha_{i,n}} \left(\left[\exp\left(\frac{\dot{\epsilon}_{i,j}^v}{\dot{\epsilon}_{0i,j}^v}\right) \right]^{\alpha_{i,n}} - 1 \right). \quad (2.54)$$

In (2.51) and (2.52) m is the rate sensitivity exponent; $\dot{\epsilon}_0^p$ is the reference plastic strain rate; and the void radius a is regarded as a function of J^p through (2.29). The rates \dot{J}^p and $\dot{\theta}^p$ are related through (2.31). In (2.53) and (2.54) η_i^{vol} and $\eta_{i,n}^{\text{dev}}$ are the volumetric and deviatoric viscous coefficients, respectively ($i = 1, \dots, M; n = 1, \dots, N_i$); and $\dot{\epsilon}_{0i,j}^v$ are the reference eigenvalues of the viscous strain rate. Non-Newtonian viscosity may be modeled by assuming that these coefficients are deformation dependent.

2.6 Microinertia

The microinertia attendant to the plastic expansion of voids is regarded as dissipated energy in a system of shell-like particles with variable mass [70, 94]. Reformulation of this

problem into an equivalent system of particles with constant mass leads to a microkinetic energy of the form [94]

$$L(b, \dot{b}) = \frac{3}{2} \rho_{v_0} \dot{b}^2; \quad \rho_{v_0} = \rho_0 N_v \frac{4\pi a_0^3}{3}, \quad b = \frac{2}{5} \frac{a^{5/2}}{a_0^{3/2}}. \quad (2.55)$$

The introduction of microinertia effects a change in the thermodynamic stress \mathbf{T}^p

$$\mathbf{T}^p = \mathbf{F}^{eT} \mathbf{P} - A_{, \mathbf{F}^p} + \left(\frac{\partial L}{\partial \mathbf{F}^p} - \frac{d}{dt} \frac{\partial L}{\partial \dot{\mathbf{F}}^p} \right), \quad (2.56)$$

that henceforth is used in place of (2.35).

2.7 Variational formulation of the rate problem

Consider a body $B \subset \mathbb{R}^3$ undergoing a motion described by the mapping $\varphi : B \times [t_1, t_2] \rightarrow \mathbb{R}^3$. Assume that the boundary ∂B , with unit normal $\bar{\mathbf{N}}$, is the union of a displacement boundary $\partial_1 B$, where boundary displacements $\bar{\varphi} : \partial_1 B \times [t_1, t_2] \rightarrow \mathbb{R}^3$ are prescribed, and a traction boundary $\partial_2 B$, where tractions $\bar{\mathbf{T}} : \partial_2 B \times [t_1, t_2] \rightarrow \mathbb{R}^3$ are applied ($\partial_1 B \cap \partial_2 B = \emptyset$). Let also $\mathbf{B} : B \times [t_1, t_2] \rightarrow \mathbb{R}^3$ be the body force. Furthermore, for every $t \in [t_1, t_2]$ the following power functional is introduced

$$\begin{aligned} \Phi[\dot{\varphi}, \dot{\mathbf{Z}}^p, \mathbf{M}^p, \mathbf{N}^p, \dot{\mathbf{Z}}_i^v, \mathbf{M}_{i,j}^v] = \\ \int_B \left[\dot{A} + \psi^* + \sum_{i=1}^M \phi_i^* - \left(\frac{\partial L}{\partial \mathbf{F}^p} - \frac{d}{dt} \frac{\partial L}{\partial \dot{\mathbf{F}}^p} \right) \cdot \dot{\mathbf{F}}^p \right] dV - \int_B \rho_0 (\mathbf{B} - \ddot{\varphi}) \cdot \dot{\varphi} dV - \int_{\partial_2 B} \bar{\mathbf{T}} \cdot \dot{\varphi} dS, \end{aligned} \quad (2.57)$$

where \mathbf{F}^p , \mathbf{Z}^p , \mathbf{M}^p , \mathbf{N}^p , \mathbf{Z}_i^v , and $\mathbf{M}_{i,j}^v$ are now regarded as fields over B ; $\dot{\mathbf{F}}^p$ is determined by $\dot{\mathbf{Z}}^p$, \mathbf{M}^p , and \mathbf{N}^p through the flow rule (2.23), and $\dot{\mathbf{F}}_i^v$ is determined by $\dot{\mathbf{Z}}_i^v$ and $\mathbf{M}_{i,j}^v$ through the viscous flow rule (2.40). Using identities (2.3), (2.35), and (2.43) and the flow

rules (2.23) and (2.40), (2.57) may be rewritten as

$$\begin{aligned} \Phi[\dot{\boldsymbol{\varphi}}, \dot{\mathbf{Z}}^p, \mathbf{M}^p, \mathbf{N}^p, \dot{\mathbf{Z}}_i^v, \mathbf{M}_{i,j}^v] = \\ \int_B \left(\mathbf{P} \cdot \text{Grad} \dot{\boldsymbol{\varphi}} - \mathbf{Y}^p \cdot \dot{\mathbf{Z}}^p - \sum_{i=1}^M \mathbf{Y}_i^v \cdot \dot{\mathbf{Z}}_i^v + \psi^* + \sum_{i=1}^M \phi_i^* \right) dV - \\ \int_B \rho_0 (\mathbf{B} - \dot{\boldsymbol{\varphi}}) \cdot \dot{\boldsymbol{\varphi}} dV - \int_{\partial_2 B} \bar{\mathbf{T}} \cdot \dot{\boldsymbol{\varphi}} dS, \end{aligned} \quad (2.58)$$

where $\mathbf{F} = \text{Grad} \boldsymbol{\varphi}$ has been introduced. The rates $\dot{\boldsymbol{\varphi}}, \dot{\mathbf{Z}}^p, \dot{\mathbf{Z}}_i^v (i = 1, \dots, M)$ and the directions of plastic and viscous flows $\mathbf{M}^p, \mathbf{N}^p, \mathbf{M}_{i,j}^v (j = 1, 2, 3)$ at the generic time $t \in [t_1, t_2]$ are found by solving the minimization problem

$$\Phi^{\text{eff}}[\dot{\boldsymbol{\varphi}}] = \inf_{\dot{\mathbf{Z}}^p, \mathbf{M}^p, \mathbf{N}^p, \dot{\mathbf{Z}}_i^v, \mathbf{M}_{i,j}^v} \Phi \left[\dot{\boldsymbol{\varphi}}, \dot{\mathbf{Z}}^p, \mathbf{M}^p, \mathbf{N}^p, \dot{\mathbf{Z}}_i^v, \mathbf{M}_{i,j}^v \right], \quad (2.59)$$

subject to constraints (2.24) and (2.25). The material velocity field follows from the minimization of the reduced power functional (2.59)

$$\inf_{\dot{\boldsymbol{\varphi}}} \Phi^{\text{eff}}[\dot{\boldsymbol{\varphi}}], \quad \dot{\boldsymbol{\varphi}} = \dot{\boldsymbol{\varphi}} \text{ on } \partial_2 B. \quad (2.60)$$

The functional $\Phi[\dot{\boldsymbol{\varphi}}, \dot{\mathbf{Z}}^p, \mathbf{M}^p, \mathbf{N}^p, \dot{\mathbf{Z}}_i^v, \mathbf{M}_{i,j}^v]$ does not depend on spatial derivatives of its fields, therefore the minimization (2.59) may be obtained locally as

$$\Phi^{\text{eff}}[\dot{\boldsymbol{\varphi}}] = \inf_{\dot{\boldsymbol{\varphi}}} \left(\int_B \phi(\text{Grad} \dot{\boldsymbol{\varphi}}) dV - \int_B \rho_0 (\mathbf{B} - \dot{\boldsymbol{\varphi}}) \cdot \dot{\boldsymbol{\varphi}} dV - \int_{\partial_2 B} \bar{\mathbf{T}} \cdot \dot{\boldsymbol{\varphi}} dS \right), \quad (2.61)$$

where

$$\begin{aligned} \phi(\dot{\mathbf{F}}) &= \inf_{\dot{\mathbf{Z}}^p, \mathbf{M}^p, \mathbf{N}^p, \dot{\mathbf{Z}}_i^v, \mathbf{M}_{i,j}^v} f \left(\dot{\mathbf{F}}, \dot{\mathbf{Z}}^p, \mathbf{M}^p, \mathbf{N}^p, \dot{\mathbf{Z}}_i^v, \mathbf{M}_{i,j}^v \right), \\ f \left(\dot{\mathbf{F}}, \dot{\mathbf{Z}}^p, \mathbf{M}^p, \mathbf{N}^p, \dot{\mathbf{Z}}_i^v, \mathbf{M}_{i,j}^v \right) &= \mathbf{P} \cdot \dot{\mathbf{F}} - \mathbf{Y}^p \cdot \dot{\mathbf{Z}}^p - \sum_{i=1}^M \mathbf{Y}_i^v \cdot \dot{\mathbf{Z}}_i^v + \psi^* + \sum_{i=1}^M \phi_i^*. \end{aligned} \quad (2.62)$$

The Euler-Lagrange equations of the power functional Φ with respect to $\dot{\mathbf{Z}}^p$ and $\dot{\mathbf{Z}}_i^v$ are the kinetic relations (2.48), and its Euler-Lagrange equations with respect to \mathbf{M}^p , \mathbf{N}^p , and $\mathbf{M}_{i,j}^v$ result in the optimal directions of plastic and viscous flows, as indicated in subsection 2.8.

It can be shown via the kinetic relations (2.48) and the flow rules (2.23), (2.40) (cf. [98, 94, 76, 28]) that the Euler-Lagrange equations corresponding to the minimization problem (2.60) are the equations of motion

$$\text{Div} \mathbf{P} + \rho_0 \mathbf{B} = \rho_0 \ddot{\boldsymbol{\varphi}} \text{ in } B, \quad \mathbf{P} \cdot \bar{\mathbf{N}} = \bar{\mathbf{T}} \text{ on } \partial_2 B. \quad (2.63)$$

2.8 Incremental constitutive updates

The time integration of the constitutive equations within a generic time interval $[t_k, t_{k+1}]$ is effected by recourse to an incremental variational update. Assume that \mathbf{F}_k^p , \mathbf{Z}_k^p , $\mathbf{Z}_{i,k}^v$ ($i = 1, \dots, M$), $\dot{\theta}_k^p$, and $\dot{\theta}_k^v$ are known at time t_k , and that the deformation gradient \mathbf{F}_{k+1} and the temperature T_{k+1} at time t_{k+1} are given. A discrete version of problem (2.59) is obtained by introducing the effective incremental strain-energy density (cf. [94])

$$W_k(\mathbf{F}_{k+1}, T_{k+1}) = \min_{\mathbf{Z}_{k+1}^p, \mathbf{M}^p, \mathbf{N}^p, \mathbf{Z}_{i,k+1}^v, \mathbf{M}_{i,j}^v} f_k(\mathbf{F}_{k+1}, T_{k+1}, \mathbf{Z}_{k+1}^p, \mathbf{M}^p, \mathbf{N}^p, \mathbf{Z}_{i,k+1}^v, \mathbf{M}_{i,j}^v), \quad (2.64)$$

where f_k is the incremental objective function

$$f_k(\mathbf{F}_{k+1}, T_{k+1}, \mathbf{Z}_{k+1}^p, \mathbf{M}^p, \mathbf{N}^p, \mathbf{Z}_{i,k+1}^v, \mathbf{M}_{i,j}^v) = W^e(\boldsymbol{\epsilon}_{k+1}^e, T_{k+1}) + W^p(\mathbf{Z}_{k+1}^p, T_{k+1}) + \sum_{i=1}^M W_i^e(\boldsymbol{\epsilon}_{i,k+1}^e, T_{k+1}) + \rho_0 C_v T_{k+1} \left(1 - \log \frac{T_{k+1}}{T_0} \right) + \Delta t \left(\psi_{k+1}^* + \sum_{i=1}^M \phi_{i,k+1}^* \right) + \beta \Delta t^2 B_{k+1}, \quad (2.65)$$

with $\Delta t = t_{k+1} - t_k$, and

$$\boldsymbol{\epsilon}_{k+1}^e = \frac{1}{2} \log(\mathbf{F}_{k+1}^e T \mathbf{F}_{k+1}^e), \quad \boldsymbol{\epsilon}_{i,k+1}^e = \frac{1}{2} \log(\mathbf{F}_{i,k+1}^e T \mathbf{F}_{i,k+1}^e), \quad (2.66)$$

$$\psi_{k+1}^* = \psi^* \left(\frac{\Delta \mathbf{Z}^p}{\Delta t}, J_{k+1}^p, T_{k+1} \right), \quad \phi_{i,k+1}^* = \phi_i^* \left(\frac{\Delta \mathbf{Z}_i^v}{\Delta t}, T_{k+1} \right), \quad (2.67)$$

$$\Delta \mathbf{Z}^p = \mathbf{Z}_{k+1}^p - \mathbf{Z}^p, \quad \Delta \mathbf{Z}_i^v = \mathbf{Z}_{i,k+1}^v - \mathbf{Z}_{i,k}^v, \quad (2.68)$$

$$B_{k+1} = \frac{3\rho_{v0}}{2} \left(\frac{b_{k+1} - b_{k+1}^{\text{pre}}}{\beta \Delta t^2} \right), \quad b_{k+1}^{\text{pre}} = b_k + \Delta t \dot{b}_k + \left(\frac{1}{2} - \beta \right) \Delta t^2 \ddot{b}_k, \quad (2.69)$$

where $\beta \in (0, \frac{1}{2})$. (2.69) defines a Newmark predictor for b_{k+1} , which is regarded as a function of J_{k+1}^p through (2.55) and (2.29). \mathbf{F}_{k+1}^p and $\mathbf{F}_{i,k+1}^v$ ($i = 1, \dots, M$) are computed through the following discrete versions of the flow rules (2.23) and (2.40)

$$\mathbf{F}_{k+1}^p = \exp(\Delta \epsilon^p \mathbf{M}^p + \Delta \theta^p \mathbf{N}^p) \mathbf{F}_k^p, \quad (2.70)$$

$$\mathbf{F}_{i,k+1}^v = \exp \left(\sum_{j=1}^3 \Delta \epsilon_{i,j}^v \mathbf{M}_{i,j}^v \otimes \mathbf{M}_{i,j}^v \right) \mathbf{F}_{i,k}^v. \quad (2.71)$$

The minimum problem (2.64) returns the updated values of the internal variables \mathbf{Z}_{k+1}^p , \mathbf{M}^p , \mathbf{N}^p , $\mathbf{Z}_{i,k+1}^v$, and $\mathbf{M}_{i,j}^v$ ($i = 1, \dots, M; j = 1, 2, 3$). The first Piola-Kirchhoff stress and consistent tangent can now be computed (cf. [94]) as

$$\mathbf{P}_{k+1} = \frac{\partial W_k}{\partial \mathbf{F}_{k+1}}, \quad D\mathbf{P}_{k+1} = \frac{\partial^2 W_k}{\partial \mathbf{F}_{k+1} \partial \mathbf{F}_{k+1}}. \quad (2.72)$$

The symmetry of the consistent tangent is a direct consequence of the potential structure of the incremental problem.

2.9 Predictor-corrector implementation

By adopting a predictor-corrector strategy based on logarithmic elastic strains to solve the variational problem (2.64), the constitutive update is reduced to small-strains and purely kinematic steps (cf. [24, 76, 94, 28]). The corresponding elastic logarithmic strains at time

t_{k+1} are

$$\boldsymbol{\epsilon}_{k+1}^e = \boldsymbol{\epsilon}_{k+1}^{e,\text{pre}} - \Delta \epsilon^p \mathbf{M}^p - \Delta \theta^p \mathbf{N}^p, \quad (2.73)$$

$$\boldsymbol{\epsilon}_{i,k+1}^e = \boldsymbol{\epsilon}_{i,k+1}^{e,\text{pre}} - \sum_{j=1}^3 \Delta \epsilon_{i,j}^v \mathbf{M}_{i,j}^v \otimes \mathbf{M}_{i,j}^v, \quad (2.74)$$

where $\mathbf{M}_{i,j}^v$ are also the eigenvectors of $\boldsymbol{\epsilon}_{i,k+1}^{e,\text{pre}}$, and

$$\boldsymbol{\epsilon}_{k+1}^{e,\text{pre}} = \frac{1}{2} \log(\mathbf{F}_k^{p-T} \mathbf{C}_{k+1} \mathbf{F}_k^{p-1}), \quad (2.75)$$

$$\boldsymbol{\epsilon}_{i,k+1}^{e,\text{pre}} = \frac{1}{2} \log(\mathbf{F}_{i,k}^{v-T} \mathbf{C}_{k+1} \mathbf{F}_{i,k}^{v-1}), \quad (2.76)$$

with $\mathbf{C}_{k+1} = \mathbf{F}_{k+1}^T \mathbf{F}_{k+1}$. (2.73)–(2.76) follow from the co-linearity between \mathbf{M}^p and $\boldsymbol{\epsilon}_{k+1}^{e,\text{pre}}$ (cf. [94]), the optimization of f_k with respect to the viscous flow directions $\mathbf{M}_{i,j}^v$ (cf. [28]), and the assumption of null incremental plastic and viscous deformations in the predictor phase.

Optimization of f_k with respect to \mathbf{M}^p , \mathbf{N}^p yields, after some algebraic manipulation

$$\mathbf{M}^p = \frac{3\mathbf{s}_{k+1}}{2\sigma_{k+1}}, \quad \mathbf{N}^p = \frac{1}{3} \text{sgn}(p_{k+1}^{\text{pre}}) \mathbf{I} \quad (2.77)$$

where

$$\mathbf{s}_{k+1} = \frac{\partial W^e}{\partial \boldsymbol{\epsilon}_{k+1}^e} = \text{dev} \left(\frac{\partial W^{e,\text{dev}}}{\partial \mathbf{e}_{k+1}^e} \right), \quad (2.78)$$

$$\sigma_{k+1} = \sqrt{\frac{3}{2} \mathbf{s}_{k+1} \cdot \mathbf{s}_{k+1}}, \quad (2.79)$$

$$p_{k+1}^{\text{pre}} = k \left[\text{tr}(\boldsymbol{\epsilon}_{k+1}^{e,\text{pre}}) - \alpha(T_{k+1} - T_0) \right], \quad (2.80)$$

with $\mathbf{e}_{k+1}^e = \text{dev}(\boldsymbol{\epsilon}_{k+1}^e)$. (2.77) determines \mathbf{M}^p implicitly, which can be expressed as

$$m_j^p = \frac{3s_{j,k+1}}{2\sigma_{k+1}}, \quad j = 1, 2, 3 \quad (2.81)$$

where m_j^p and $s_{j,k+1}$ are the eigenvalues of M^p and \mathbf{s}_{k+1} , respectively.

Optimization of f_k with respect to $\theta_{k+1}^p, \epsilon_{k+1}^p$ yields

$$\Delta\theta^p = 0, \quad \Delta\epsilon^p = 0 \quad (2.82)$$

if

$$p_{k+1}^{\text{pre}} \leq p_c(\theta_k^p, \epsilon_k^p, T_{k+1}), \quad \sigma_{k+1}^{\text{pre}} \leq \sigma_c(\theta_k^p, \epsilon_k^p, T_{k+1}), \quad (2.83)$$

or

$$p_{k+1}^{\text{pre}} - k \Delta\theta^p = p_{c,k+1} + \frac{\partial}{\partial \theta_{k+1}^p} [\Delta t \psi_{k+1}^* + \beta \Delta t^2 B_{k+1}], \quad (2.84)$$

$$\sigma_{k+1} = \sigma_{c,k+1} + \frac{\partial}{\partial \epsilon_{k+1}^p} [\Delta t \psi_{k+1}^* + \beta \Delta t^2 B_{k+1}], \quad (2.85)$$

otherwise, with

$$\sigma_{k+1}^{\text{pre}} = \sqrt{\frac{3}{2} \mathbf{s}_{k+1}^{\text{pre}} \cdot \mathbf{s}_{k+1}^{\text{pre}}}, \quad (2.86)$$

and

$$\mathbf{s}_{k+1}^{\text{pre}} = \frac{\partial W^{e,\text{dev}}}{\partial \mathbf{e}_{k+1}^{e,\text{pre}}} = \text{dev} \left(\frac{\partial W^e}{\partial \boldsymbol{\epsilon}_{k+1}^{e,\text{pre}}} \right), \quad (2.87)$$

where $\mathbf{e}_{k+1}^{e,\text{pre}}$ is the deviatoric part of $\boldsymbol{\epsilon}_{k+1}^{e,\text{pre}}$.

(2.81), (2.84), and (2.85) may be solved for the unknowns $\theta_{k+1}^p, \epsilon_{k+1}^p, m_j^p (j = 1, 2, 3)$ by recourse to a Newton-Raphson iteration, under the constraints

$$\Delta\theta^p \geq 0, \quad \Delta\epsilon^p \geq 0. \quad (2.88)$$

Optimization of f_k with respect to $\epsilon_{i,j,k+1}^v (i = 1, \dots, M; j = 1, 2, 3)$ leads to the system of equations

$$\sigma_{i,j,k+1}^v = \frac{\partial}{\partial \epsilon_{i,j,k+1}^v} (\Delta t \phi_i^*) \quad (2.89)$$

that can again be solved via a Newton-Raphson iteration. Furthermore, (2.89) may be recast

as

$$\sigma_{i,j,k+1}^v = \frac{\partial W_i^e}{\partial \epsilon_{i,j,k+1}^e}, \quad (2.90)$$

which defines $\sigma_{i,j,k+1}^v$ as a function of $\epsilon_{i,j,k+1}^v$, together with (2.74).

2.10 Stress update

Once \mathbf{Z}_{k+1}^p , \mathbf{M}^p , \mathbf{N}^p , $\mathbf{Z}_{i,k+1}^v$, $\mathbf{M}_{i,j}^v$ are determined, the updated equilibrium and viscous stresses follow from

$$\boldsymbol{\sigma}_{k+1} = p_{k+1} \mathbf{I} + \mathbf{s}_{k+1}, \quad (2.91)$$

$$\boldsymbol{\sigma}_{i,k+1}^v = p_{i,k+1}^v \mathbf{I} + \sum_{j=1}^3 s_{i,j,k+1}^v \mathbf{M}_{i,j}^v \otimes \mathbf{M}_{i,j}^v, \quad (2.92)$$

with \mathbf{s}_{k+1} given by (2.78), and

$$p_{k+1} = \frac{\partial W^{e,\text{vol}}}{\partial \theta_{k+1}^e}, \quad (2.93)$$

$$p_{i,k+1}^v = (\sigma_{i,1,k+1}^v + \sigma_{i,2,k+1}^v + \sigma_{i,3,k+1}^v) / 3, \quad (2.94)$$

$$s_{i,j,k+1}^v = \sigma_{i,j,k+1}^v - p_{i,k+1}^v. \quad (2.95)$$

Due to the variational structure of the update, the stresses and strains satisfy the potential relations

$$\boldsymbol{\sigma}_{k+1} = \frac{\partial W_k}{\partial \boldsymbol{\epsilon}_{k+1}^e}, \quad \boldsymbol{\sigma}_{i,k+1}^v = \frac{\partial W_k}{\partial \boldsymbol{\epsilon}_{k+1}^{e,i}}. \quad (2.96)$$

The first Piola-Kirchhoff stress follows from

$$\mathbf{P}_{k+1} = \mathbf{P}_{k+1}^\infty + \mathbf{P}_{i,k+1}^{ve} \quad (2.97)$$

with

$$\mathbf{P}_{k+1}^\infty = \frac{\partial W_k}{\partial \boldsymbol{\epsilon}_{k+1}^p} \cdot \frac{\partial \boldsymbol{\epsilon}_{k+1}^e}{\partial \mathbf{C}_{k+1}} \cdot \frac{\partial \mathbf{C}_{k+1}}{\partial \mathbf{F}_{k+1}}, \quad (2.98)$$

$$\mathbf{P}_{i,k+1}^{ve} = \frac{\partial W_k}{\partial \boldsymbol{\epsilon}_{i,k+1}^e} \cdot \frac{\partial \boldsymbol{\epsilon}_{i,k+1}^e}{\partial \mathbf{C}_{k+1}} \cdot \frac{\partial \mathbf{C}_{k+1}}{\partial \mathbf{F}_{k+1}}. \quad (2.99)$$

\mathbf{P}_{k+1}^∞ and $\mathbf{P}_{i,k+1}^{ve}$ can also be expressed in indicial notation as (index $k + 1$ not shown for convenience)

$$(\mathbf{P}^\infty)_{jH} = (\boldsymbol{\sigma})_{AB} D \log(\mathbf{C}^{e,pre})_{ABCD} (\mathbf{F}_k^{p-1})_{HC} (\mathbf{F}_k^{p-1})_{LD} F_{jL}, \quad (2.100)$$

$$(\mathbf{P}_i^{ve})_{jH} = (\boldsymbol{\sigma}^v)_{AB} D \log(\mathbf{C}_i^{e,pre})_{ABCD} (\mathbf{F}_{i,k}^{v-1})_{HC} (\mathbf{F}_{i,k}^{v-1})_{LD} F_{jL}, \quad (2.101)$$

with $\mathbf{C}^{e,pre} = \mathbf{F}_k^{p-T} \mathbf{C}_{k+1} \mathbf{F}_k^{p-1}$, and $\mathbf{C}_i^{e,pre} = \mathbf{F}_{i,k}^{v-T} \mathbf{C}_{k+1} \mathbf{F}_{i,k}^{v-1}$. The consistent may be obtained by following [94] and [75].

Chapter 3

Validation

3.1 Parameter identification

This section presents a parameter identification method and several parameter estimates obtained via Genetic Algorithms (GAs). The identification procedure assumes that a collection of N^e experimental results is available for model parameter identification, through a data set of the form

$$\left\{ [x_i^e, \bar{y}_i^e]_{i=1, \dots, N_p^e} \right\}_{e=1, \dots, N^e}, \quad (3.1)$$

where x_i^e are experimental observations of a suitable *strain measure* x , and \bar{y}_i^e are the corresponding recordings of a *stress measure* y , and N_p^e is the number of data points for experiment e . The best-fit values of selected parameters

$$\mathbf{p} = \left\{ \{p_m\}_{m=1, \dots, P} \right\}, \quad (3.2)$$

are sought, under simple bounds of the form

$$\mathbf{p} \in D = [p_1^{lb}, p_1^{ub}] \times \dots \times [p_P^{lb}, p_P^{ub}], \quad (3.3)$$

If \mathbf{p} is assigned, numerical simulations of the experiments can be employed to get a set of predictions

$$\left\{ \{x_i^e, y_i^e(\mathbf{p})\}_{i=1, \dots, N_p^e} \right\}_{e=1, \dots, N^e}, \quad (3.4)$$

and their fitting performance can be evaluated through the *fitness function*

$$f(\mathbf{p}) = \max_i |y_i^e(\mathbf{p}) - \bar{y}_i^e|, \quad (3.5)$$

which is an L_∞ norm of the residuals $y^e - \bar{y}^e$. This leads to the multivariate minimization problem

$$\min_{\mathbf{p} \in D} f(\mathbf{p}), \quad (3.6)$$

which is expected to be non-convex and affected by multiple local optima (cf. Ogden et al. [67]).

GAs are well suited for the minimization of non-convex objective functions due to their ability to explore the entire search space looking for a global minima [87].

A steady-state GA is adapted, where a population of individuals is created sampling the search space. A temporary population is created at every generation and added to the previous one. The worst individuals are removed in order to maintain the size of the population constant. The roulette-wheel selection method was utilized with scaled fitness scores. Any individual has a probability p of being chosen where p is equal to the fitness of the individual divided by the sum of the fitnesses of all the individuals in the population. An initial population of 500–1000 individuals was used along with a mutation percentage of 0.01 and a crossover percentage of 0.6. Although the algorithm was set to terminate after 200–500 generations, it started to converge to a minima, which could be local or global, after approximately 80 generations. It is worth noting that the selection strength for a steady-state GA is twice that of a generational GA, where for each m members of the population there are only $2m$ selections.

3.2 High strain rate compression tests on polyurea

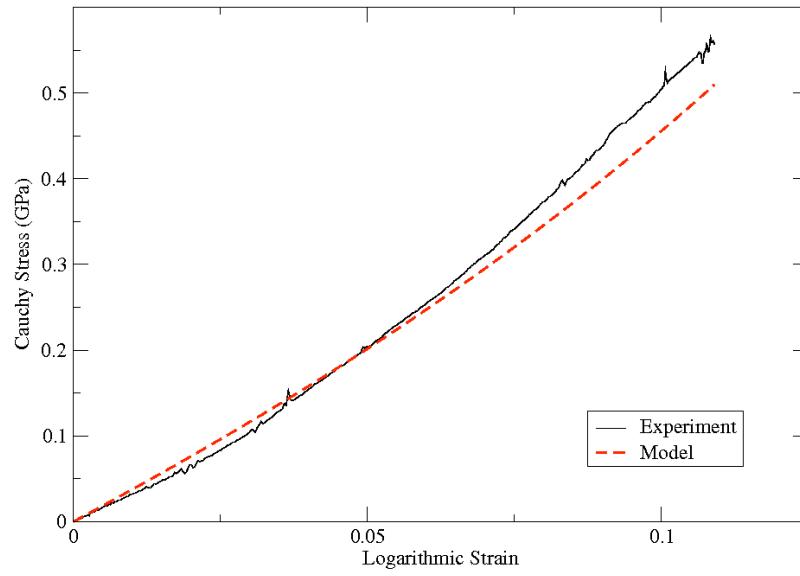
The experimental data considered for polyurea under compression was obtained from the *Center of Excellence for Advanced Materials* at the University of California, San Diego. The experiments were a series of split-Hopkinson bar tests performed by Alireza et al., some of which are referenced from [5]. 15 sets of stress-strain response experiments of polyurea were considered, 3 of which were under unconfined compression loading conditions and the rest under confined compression. These data sets were fitted simultaneously via GAs with

$$\mathbf{p} = \{\mu_1, \alpha_1, \mu_2, \alpha_2, \sigma_0, \epsilon_0^p, n, \dot{\epsilon}_0^p, m\} (P = 9). \quad (3.7)$$

One set of parameters was obtained for all 15 experiments, proving the outstanding effectiveness of the GAs approach. The applied strain rates were in the range of 1,200–37,000 s^{-1} for the confined compression tests and 3,400–6,200 s^{-1} for the unconfined compression. Results for some values of the applied strain rates are presented in Figs. 3.1 and 3.2, with the corresponding parameters in Tab. 3.1.

Confined Compression (1,200/sec Effective Strain Rate)

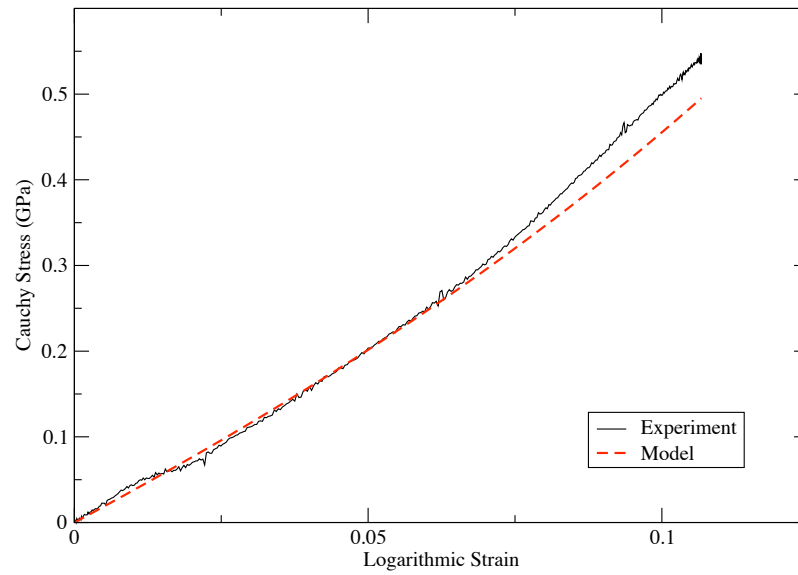
273K Temperature



(a)

Confined Compression (1,300/sec Effective Strain Rate)

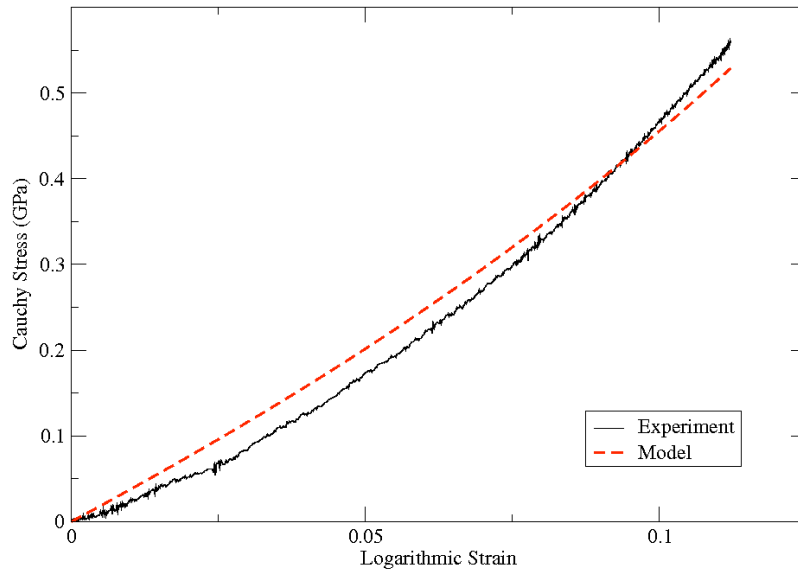
294K Temperature



(b)

Confined Compression (1,400/sec Effective Strain Rate)

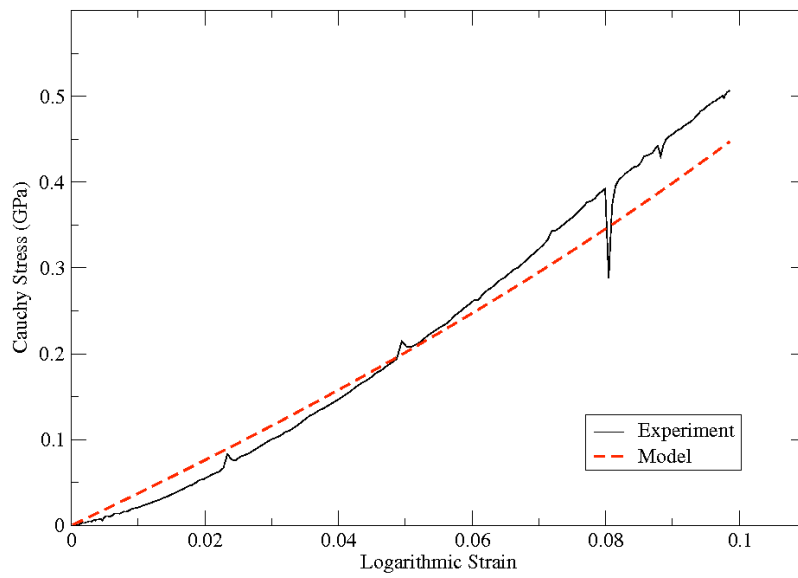
294K Temperature



(c)

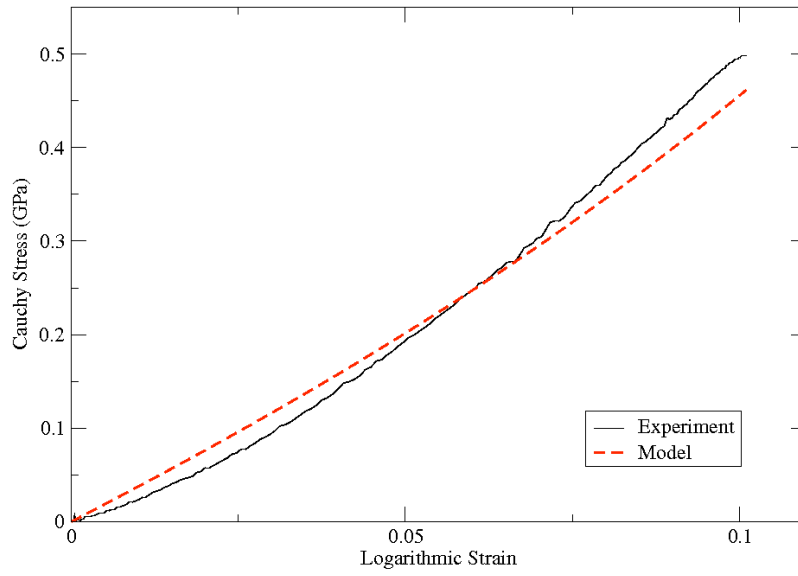
Confined Compression (2,600/sec Effective Strain Rate)

273K Temperature



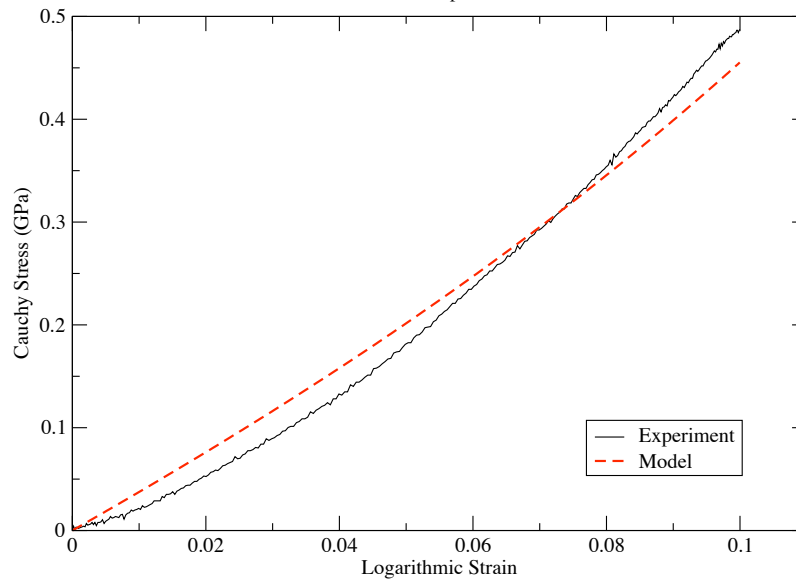
(d)

Confined Compression (2,800/sec Effective Strain Rate)
294K Temperature

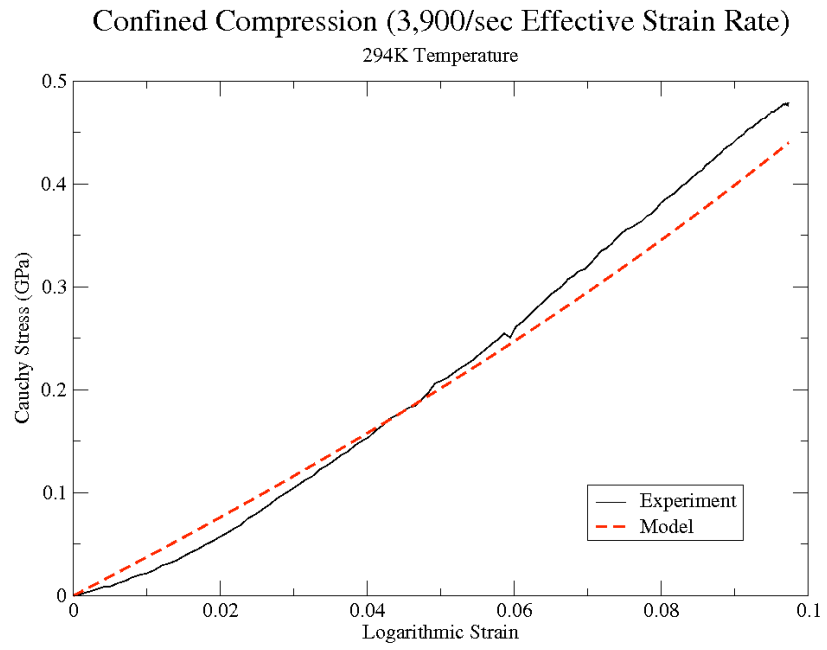


(e)

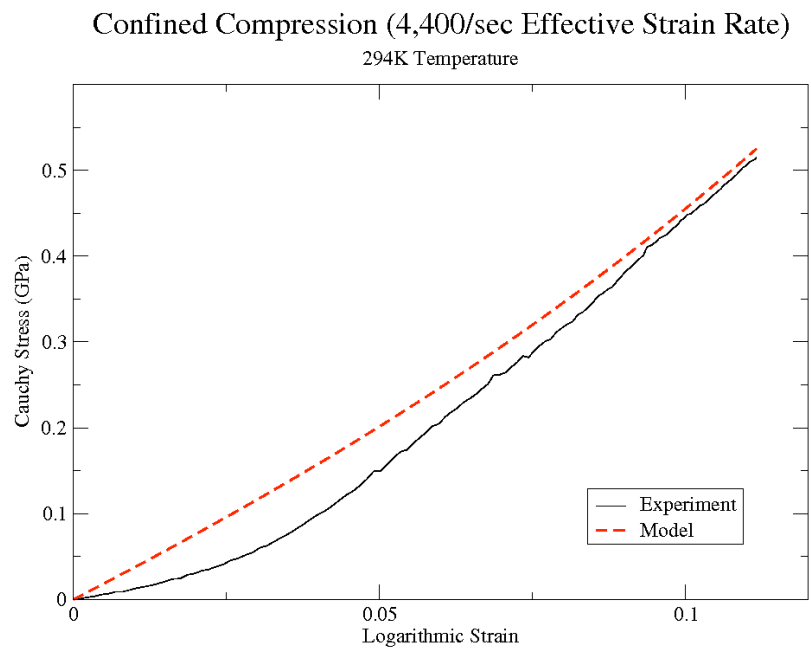
Confined Compression (3,000/sec Effective Strain Rate)
294K Temperature



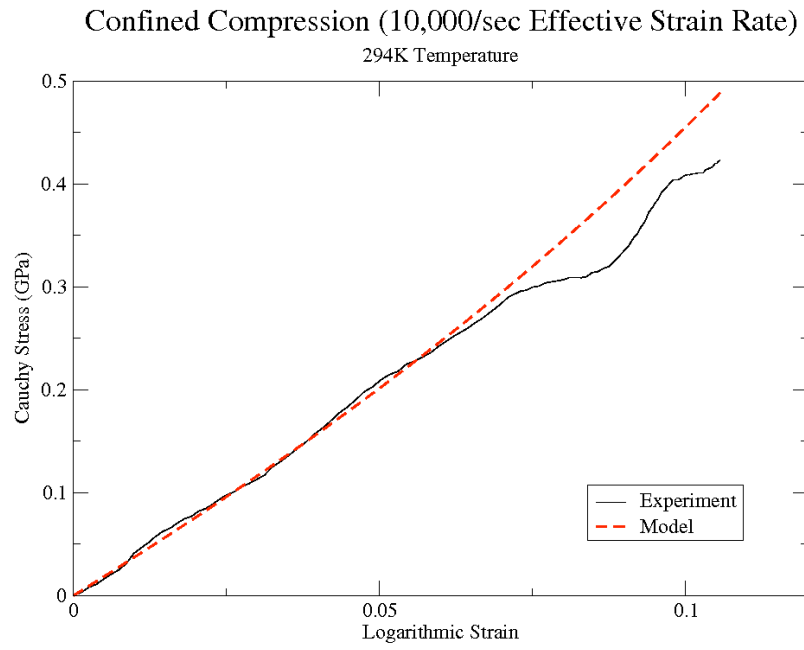
(f)



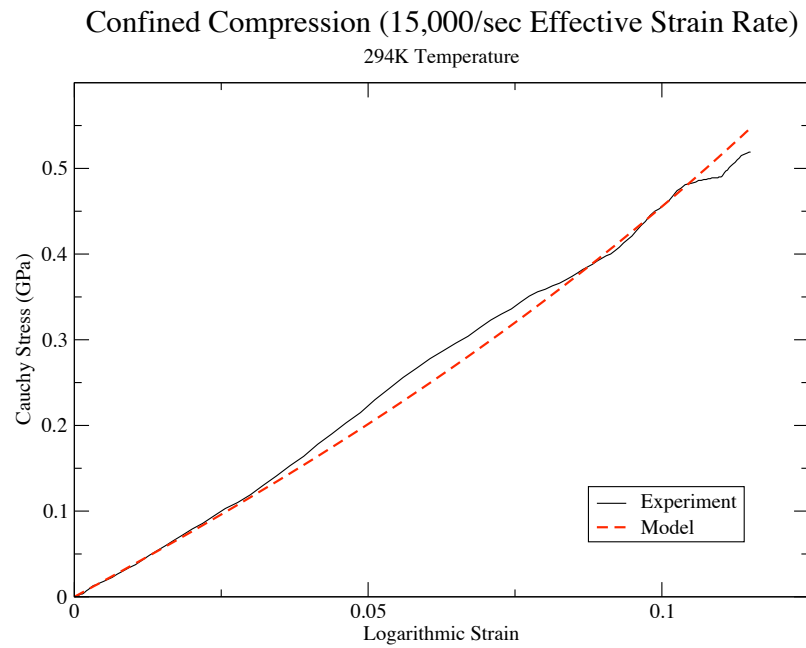
(g)



(h)



(i)



(j)

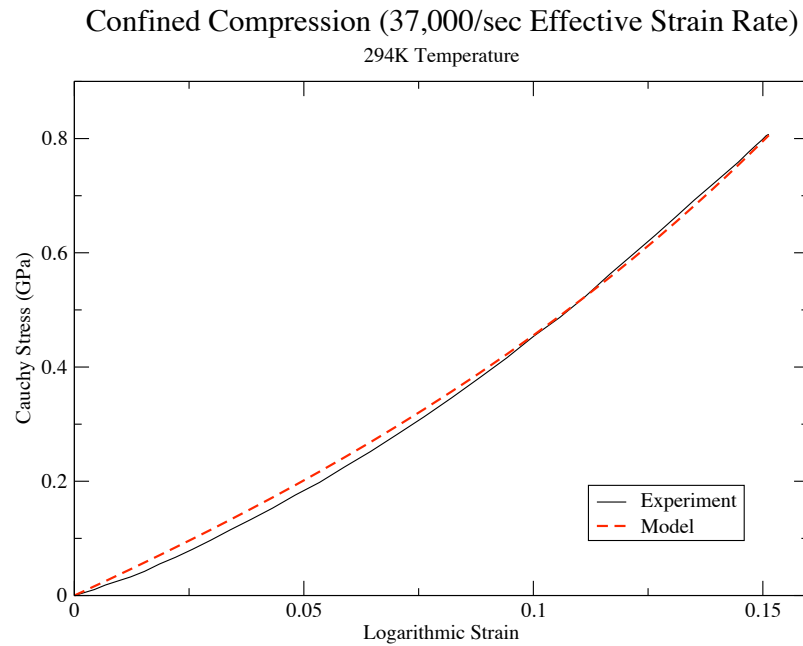
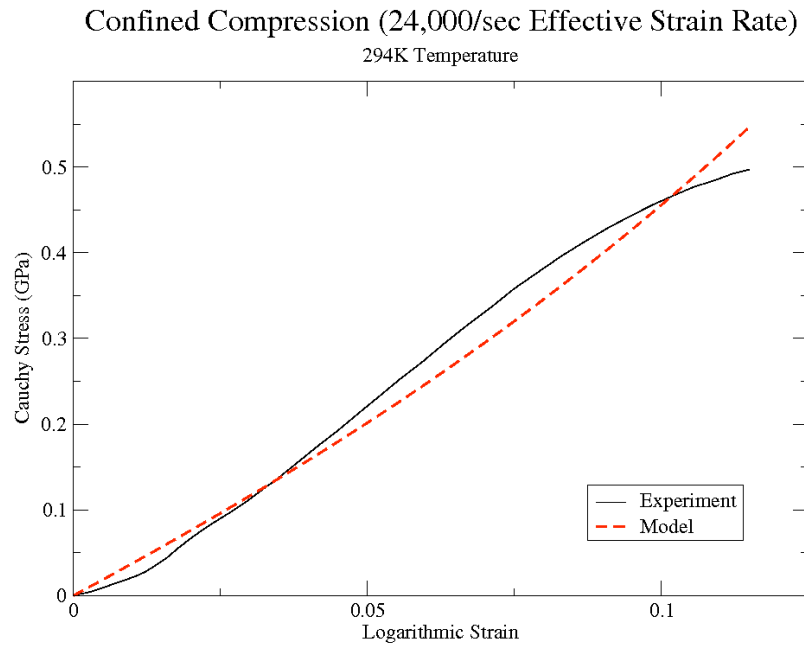
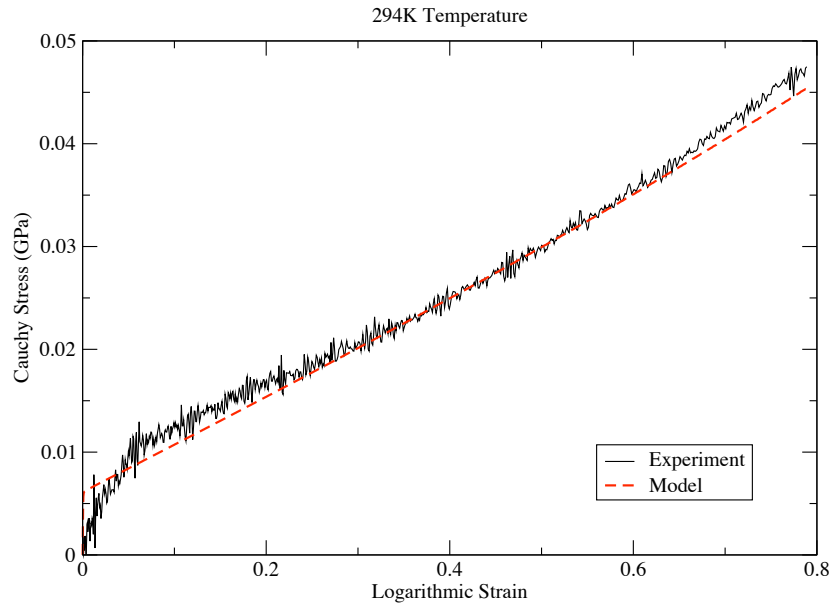


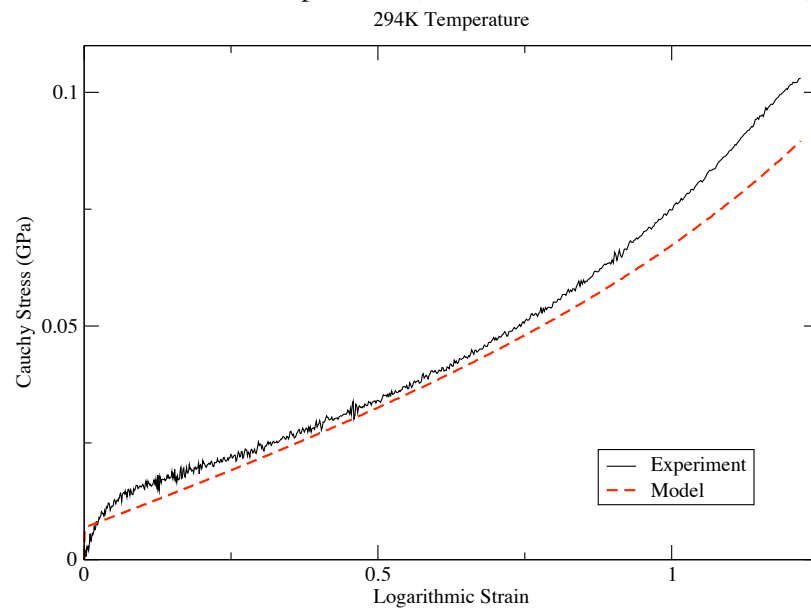
Figure 3.1: Alireza et al. experimental confined compression curves [5] vs. GAs fits. Fitting curves correspond to one set of material parameters (cf. Tab. 3.1).

Unconfined Compression (3,400/sec Effective Strain Rate)



(a)

Unconfined Compression (4,500/sec Effective Strain Rate)



(b)

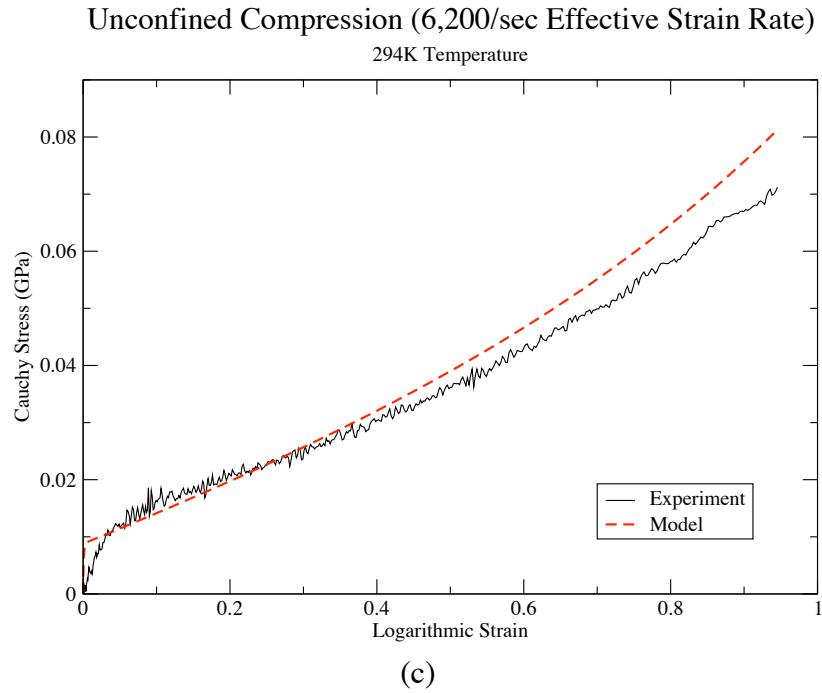


Figure 3.2: Alireza et al. experimental unconfined compression curves [5] vs. GAs fits. Fitting curves correspond to one set of material parameters (cf. Tab. 3.1).

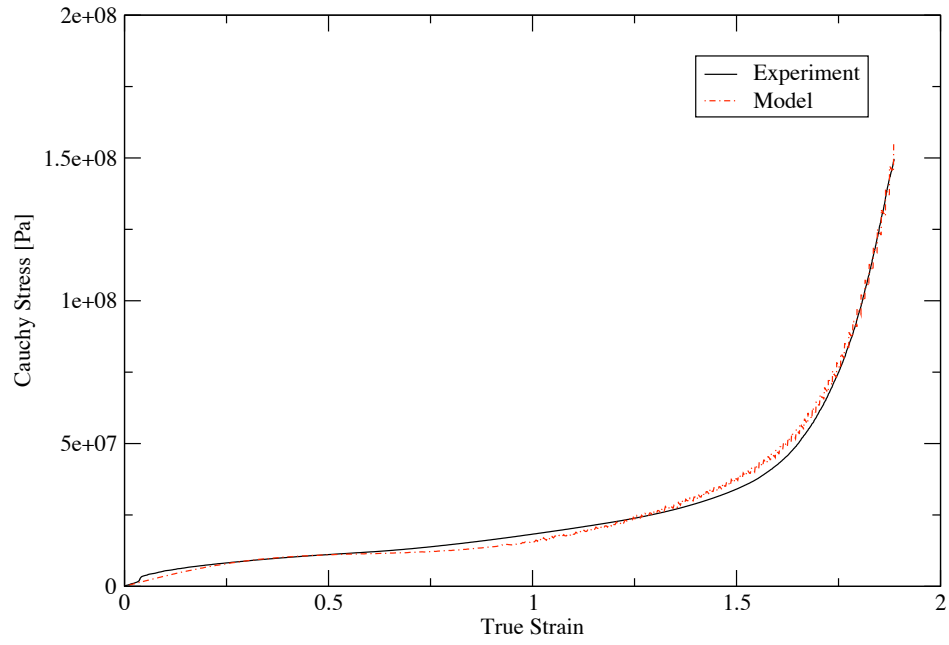
μ_1 [Pa]	94.9×10^6
α_1	17.0
μ [Pa]	-403×10^6
α_2	-9.77
μ^∞ [Pa]	807×10^6
σ_0 [Pa]	5.26×10^6
ϵ_0^p	0.12
n	1.0
$\dot{\epsilon}_0^p$ (s^{-1})	7200
m	0.411

Table 3.1: GAs material parameter estimates for UCSD compression tests on polyurea [5]

3.3 Tension tests on polyurea

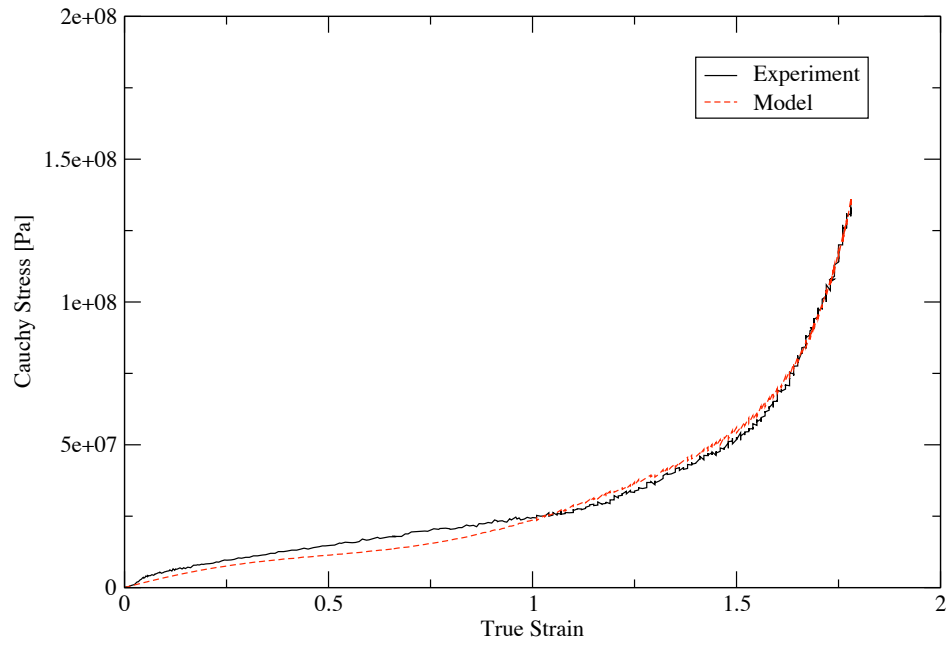
The experimental data considered for polyurea under tension was provided by [84]. The reported results were obtained on a newly developed drop-weight tensile test instrument that ensures strain rate uniformity and strain homogeneity. Shuttle speeds as high as 26 m s⁻¹ were achievable, corresponding to strain rates $\sim 10^3$ s⁻¹ [84]. Tests were conducted at strain rates varying from 0.15 s⁻¹ (quasi-static) to 408 s⁻¹–573 s⁻¹ (high strain rates). The initial region is linear, with a slope approaching 100 MPa at the highest rates. There is also an increase in stiffness as the strain rate increases (see Fig. 3.3.) Considering all of these factors, GAs were utilized to determine sets of parameters for the experiments. It is important to note that the Ogden parameters thus obtained are stiffer as the strain rate increases (see Tab. 3.2.) Also, in agreement with [84], viscoelastic behavior is evident, with the result that the mechanical properties of polyurea in tension are highly rate-dependent (Tab. 3.2.) The model is evidently able to capture these complex behaviors via 3 Ogden terms in deviatoric elasticity, 2 relaxation mechanisms (the first with 3 Ogden terms and the second with only one), and deviatoric plasticity.

0.15/s



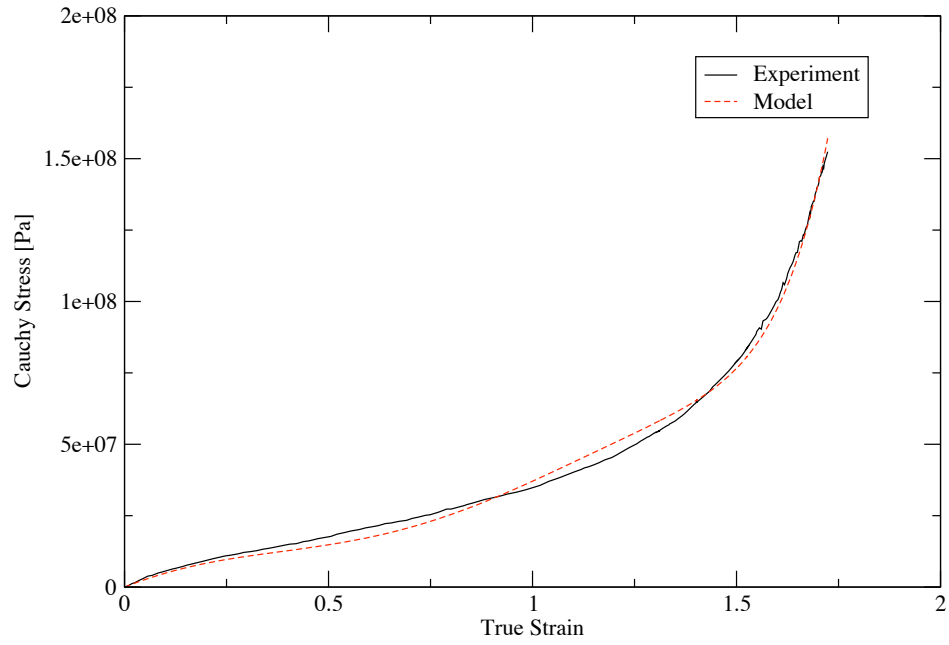
(a)

14/s



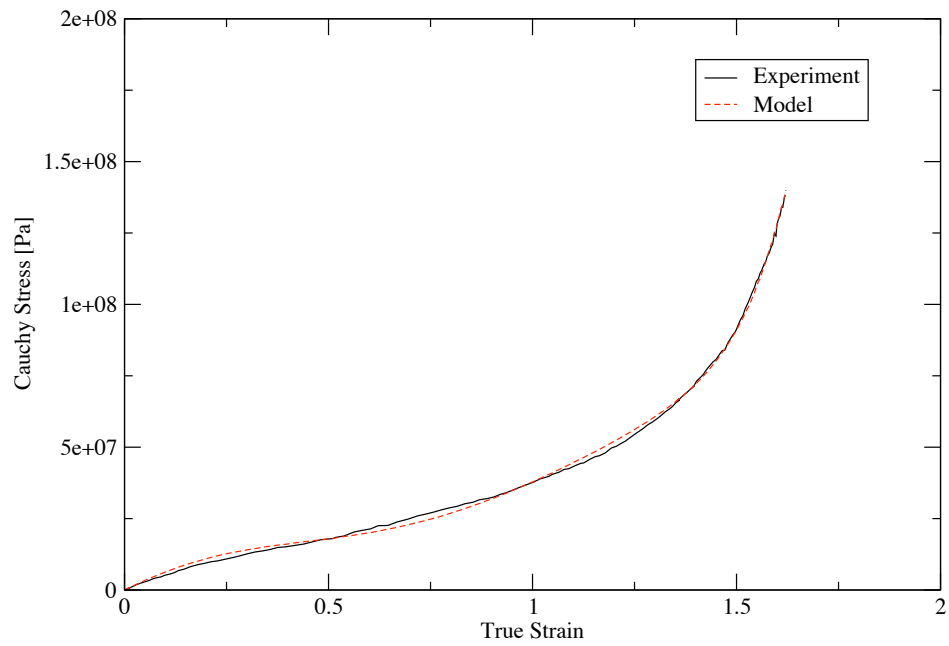
(b)

327/s



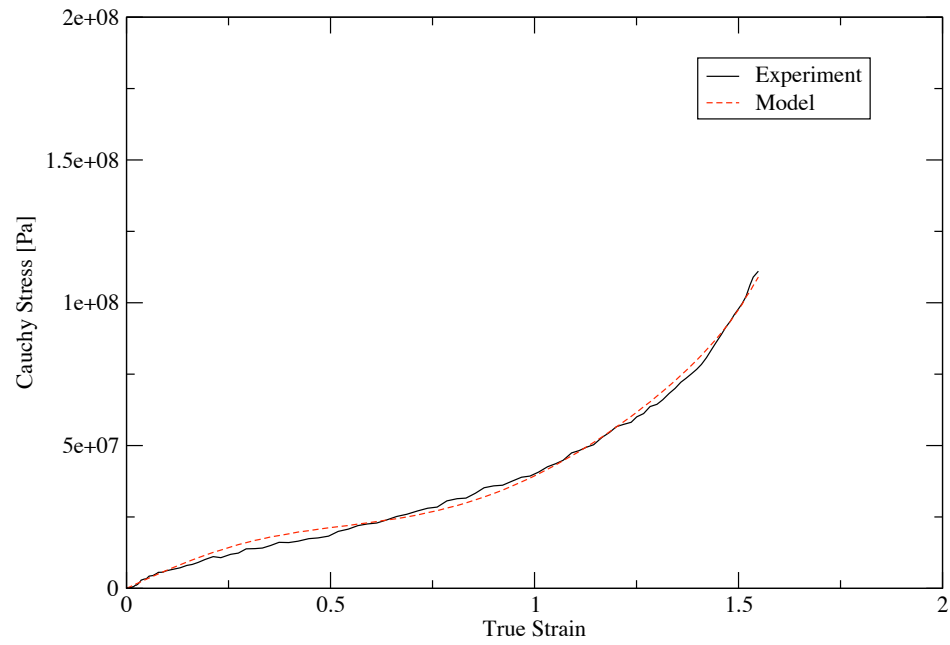
(c)

408/s



(d)

573/s



(e)

Figure 3.3: Tension tests on polyurea. Cauchy stress vs. true strain (all corrected for inertial forces), with the corresponding strain rates as indicated. The model Cauchy stresses are also shown for the same strain rates.

Strain rate [s^{-1}]	0.15	14	327	408	573
μ_1 [Pa]	34.45	55.0	96.92	154.26	148.64
α_1	7.44	7.44	7.5	7.29	7.84
μ_2 [Pa]	33.67	51.8	100.78	146.93	154.15
α_2	7.86	7.47	7.46	8.01	6.09
μ_3 [Pa]	32.72	53.62	98.6	153.57	147.87
α_3	5.33	7.64	7.58	6.65	5.03
τ_1 [s]	2.02	0.0195	0.0006	0.0005	0.0005
$\mu_{1,1}$ [Pa]	1.73×10^6	1.83×10^6	2.79×10^6	2.68×10^6	2.55×10^6
$\alpha_{1,1}$	4.72	4.0	4.0	6.0	5.58
$\mu_{1,2}$ [Pa]	1.6×10^6	1.84×10^6	2.44×10^6	2.54×10^6	2.59×10^6
$\alpha_{1,2}$	4.5	4.28	4.11	4.58	5.39
$\mu_{1,3}$ [Pa]	1.97×10^6	1.92×10^6	2.79×10^6	2.52×10^6	2.46×10^6
$\alpha_{1,3}$	4.78	4.21	4.29	6.0	5.47
τ_2 [s]	41.66	0.355	0.0116	0.00992	0.00992
$\mu_{2,1}$ [Pa]	192218	483001	937288	942297	718477
$\alpha_{2,1}$	4.62	4.47	4.58	4.46	4.44
σ_0 [Pa]	5.59×10^6	6.57×10^6	5.64×10^6	6.47×10^6	5.59×10^6
ϵ_0^p	1.1	1.1	1.1	1.01	1.1
n	0.005	0.005	0.005	0.004	0.001

Table 3.2: Model parameter estimates for tension tests on polyurea at various strain rates

3.4 Tensile tests on high-density polyethylene

Density measurements on stretched semi-crystalline polymers such as high-density polyethylene (HDPE) under uniaxial tension have shown significant dilatation due to void formation and crazing [4]. The behavior of HDPE during tensile continuous loading at constant strain

rate, unloading, and recovery is examined. The specimen is deformed at a strain rate of 10^{-3}s^{-1} until the strain under load reaches 1.0, subsequently unloaded at the same rate, and finally left to recover at zero stress for 3 hours [4]. The evolution of volume strain, $\epsilon_v = \epsilon_{11} + \epsilon_{22} + \epsilon_{33}$, vs. true axial strain ϵ_{33} , is shown in Fig. 3.6. It is important to note that the recorded experimental volume strain is both elastic and plastic, nevertheless, the elastic component contributes minimally and there is an early onset of plastic dilatation [4]. With the activation of deviatoric and volumetric plasticity along with one relaxation mechanism and rate effects, the fitting parameters are let to be

$$\mathbf{p} = \{ \mu_1, \alpha_1, \tau_1, K^\infty, \mu_{1,1}, \alpha_{1,1}, K^0, \sigma_0, \epsilon_0^p, n, N_v, \dot{\epsilon}_0^p, m \}, \quad (3.8)$$

with $P = 13$. The resulting values of the parameters, obtained from GA, are shown in Tab. 3.3.

μ_1 [Pa]	70.2×10^6
α_1	1.10
μ^∞ [Pa]	38.7×10^6
K^∞ [Pa]	9.89×10^9
τ_1 [s]	8.10
$\mu_{1,1}$ [Pa]	129×10^6
$\alpha_{1,1}$	12.15
K^1 [Pa]	9.95×10^9
μ^1 [Pa]	822×10^6
σ_0 [Pa]	5.43×10^6
ϵ_0^p	0.89
n	0.50
a_0 [m]	10.0×10^{-6}
N_v [m^{-3}]	3.87×10^{12}
$\dot{\epsilon}_0^p$ [s^{-1}]	51.98
m	14.75

Table 3.3: GAs material parameter estimates for a tensile uniaxial test in [4] on high-density polyethylene (strain rate: $\dot{\epsilon} = 0.001\text{s}^{-1}$)

The volumetric strain recovered from the model is $\log(J^p)$, which is due to void expansion and shrinkage during the process of cavitation. A total residual plastic strain of 0.76 and volumetric plastic strain of 0.046 were obtained from the simulation compared to the experimental values of 0.71 and 0.044, respectively. Figs. 3.5 and 3.6 show the model's ability to capture void growth and shrinkage in HDPE.

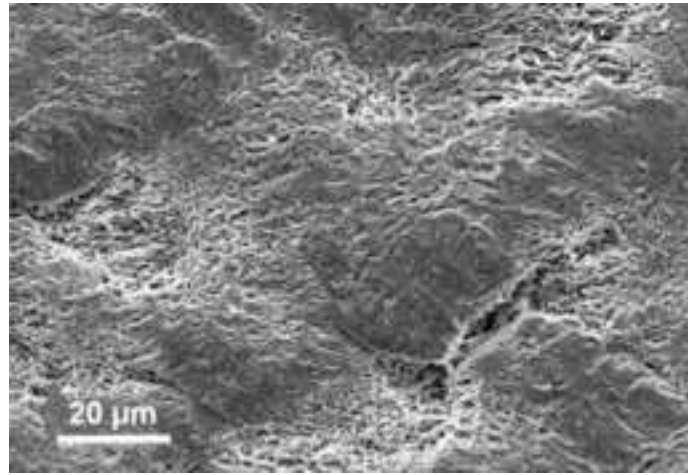


Figure 3.4: SEM observation of cavitation mechanisms in HDPE during plastic deformation (tensile axis is vertical). Interspherulitic decohesion for $\epsilon_{33r} = 0.71$ (axial residual strain) [4]

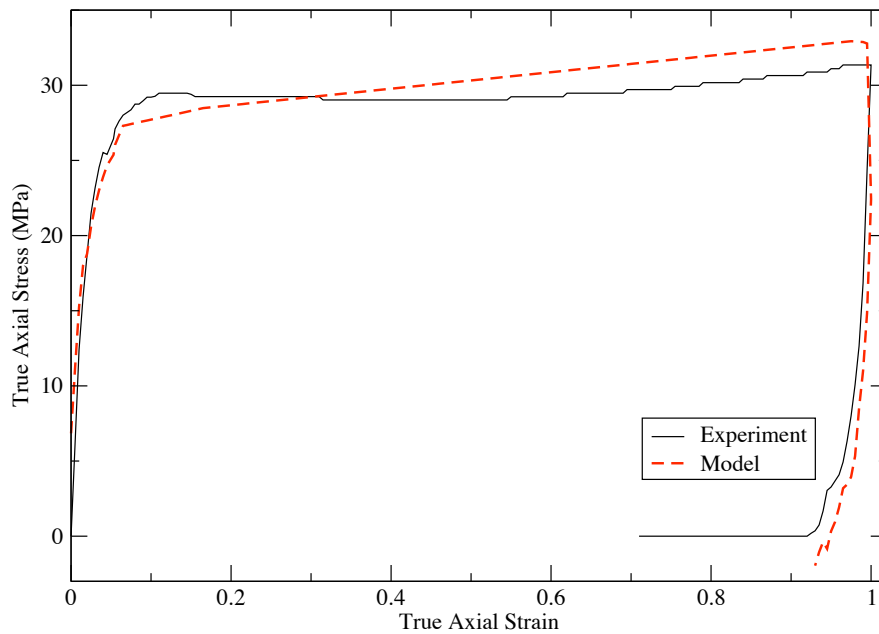


Figure 3.5: Predicted and experimental axial stress-axial strain curves for a tensile uniaxial test by [4] on high-density polyethylene (strain rate: $\dot{\epsilon} = 0.001\text{s}^{-1}$)

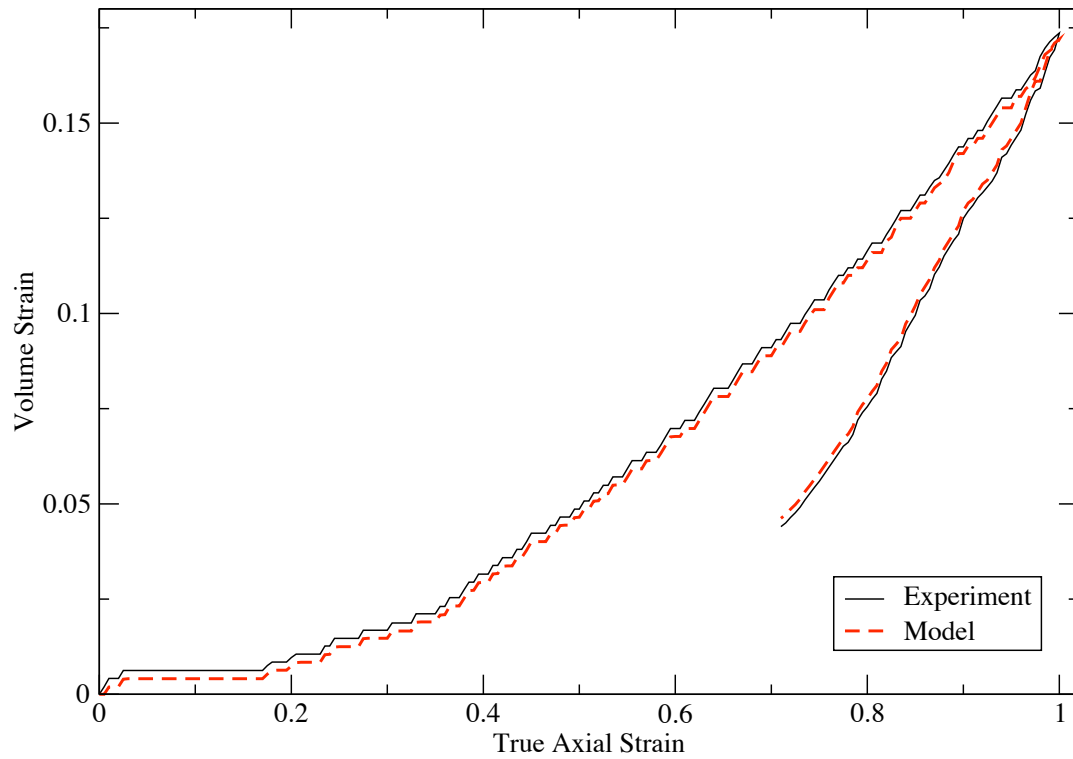


Figure 3.6: Total experimental volumetric strain in HDPE [4] used as input and model volumetric plastic strain-axial strain. The difference between the curves is the volumetric elastic strain. This shows the ability of the model to distinguish between elastic and plastic volumetric strain (strain rate: $\dot{\epsilon} = 0.001\text{s}^{-1}$).

3.5 Monotonic and cyclic uniaxial tests on brain tissue

Uniaxial tests performed by Miller et al. [57] on short cylindrical samples of swine brain tissue are considered [57]. These tests were performed in both tension and compression (Fig. 3.7), under different strain rates (*moderately high*, *intermediate*, and *low* strain rates). Brain samples were extracted between the arachnoid membrane and the ventricle surface of the swine brains, with a 30 mm diameter and a 13 mm height, in order to measure *averaged* isotropic properties of the tissue.

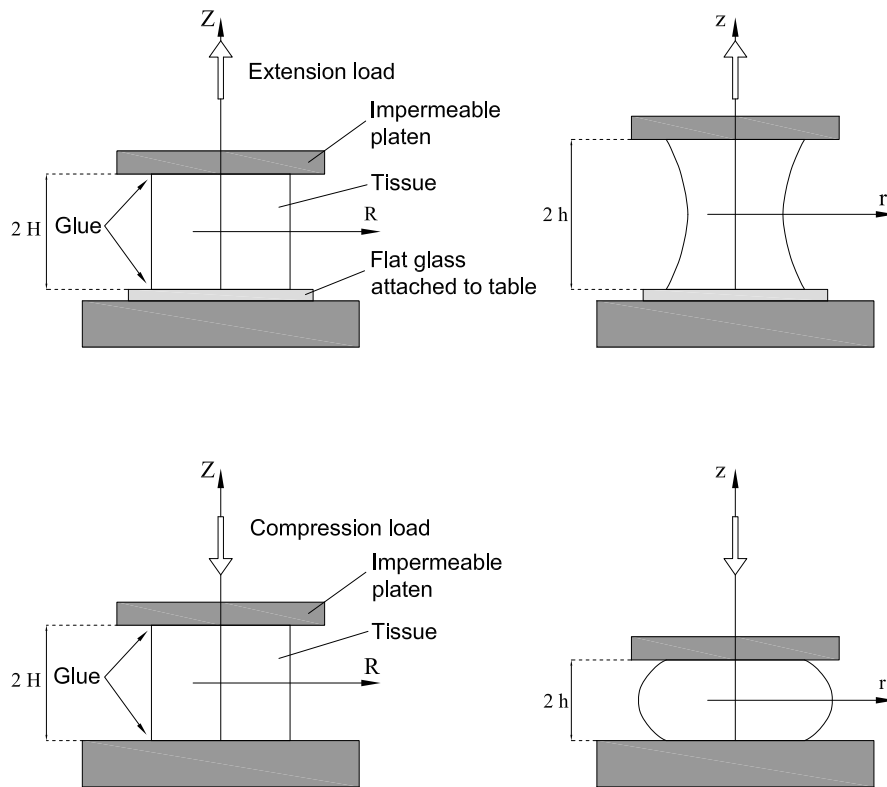


Figure 3.7: Illustration of the uniaxial tests on short cylindrical samples of brain tissue by [57]

The experimental results in [57] can be summarized into five stress-strain curves [58], relating the first Piola-Kirchhoff traction P_z (vertical force divided by the undeformed cross-sectional area) with the mean stretch λ (current sample height $2h$ divided by the

initial height $2H$, cf. Fig. 3.7). Two curves are in tension ($\dot{\lambda} = 0.64, 0.64 \times 10^{-2} \text{s}^{-1}$), and three in compression ($\dot{\lambda} = 0.64, 0.64 \times 10^{-2}, 0.64 \times 10^{-5} \text{s}^{-1}$).

A first set of parameter estimates was obtained through a viscoelastic fitting model (ve), ignoring the plastic part of the equilibrium network. Two relaxation mechanisms were considered, one-term Ogden-models, and independent tensile and compressive responses. The selected fitting parameters are

$$\mathbf{p} = \{\mu_1, \alpha_1, \tau_1, \mu_{1,1}, \alpha_{1,1}, \tau_2, \mu_{2,1}, \alpha_{2,1}\}, \quad (P = 8), \quad (3.9)$$

where

$$\tau_i = \frac{\eta_{i,1}^{\text{dev}}}{\mu_{i,1}} \quad (i = 1, 2) \quad (3.10)$$

denote the *relaxation times* of the viscous networks.

The tensile-compressive GAs estimates are shown in the first two columns of Tab. 3.4. The positive $\{\mu, \alpha\}$ pairs in tension ($N^e = 2$), negative pairs in compression ($N^e = 3$), and significantly higher shear moduli μ^0, μ^∞ in compression confirm the well-known notion in the literature of the heterogeneous tensile-compressive nature of brain tissue (cf. [57, 79, 54, 91]). A comparison between experimental and fitting stress-strain curves is shown in Fig. 3.8.

Further estimates were obtained for the mixed tensile-compressive response (*global response*: $N^e = 5$), alternatively considering a pure viscoelastic (ve), and a viscoelastic/elasto-plastic (ve/ep) model. In the first case the procedure is as before, while in the second the plastic section of the time-infinity network was activated, assuming

$$\mathbf{p} = \{\mu_1, \alpha_1, \tau_1, \mu_{1,1}, \alpha_{1,1}, \tau_2, \mu_{2,1}, \alpha_{2,1}, \sigma_0, \epsilon_0^p\}, \quad (P = 10) \quad (3.11)$$

(plastic rate effects were deactivated).

The global GAs estimates are shown in the third and fourth columns of Tab. 3.4, while the corresponding fitting curves are depicted in Fig. 3.9. It can be observed that the global

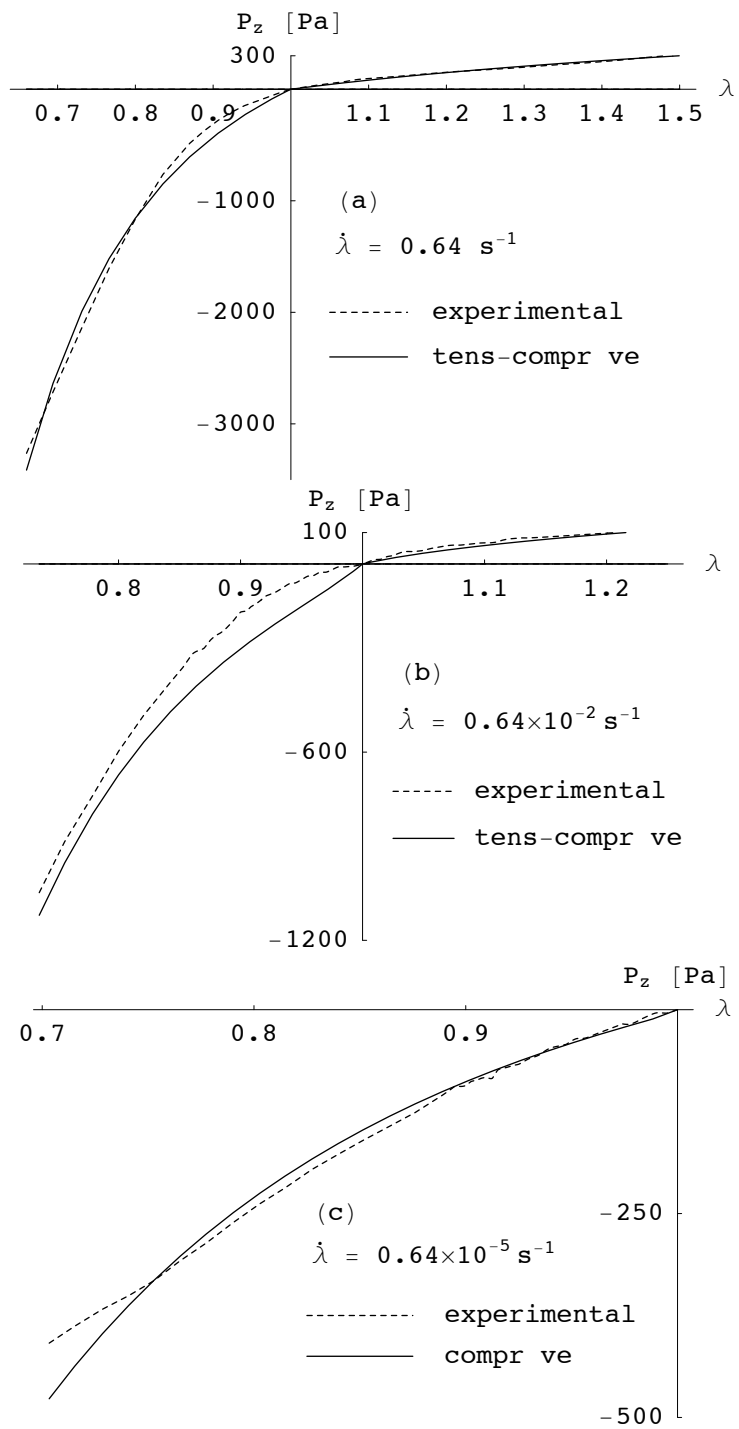


Figure 3.8: Independent tension-compression viscoelastic fits of experiments in [57]

Fit Type	ten. ve	comp. ve	global ve	global ve/ep
μ_1 [Pa]	106.4	-147.6	-45.8	-30.6
α_1	1.89	-2.95	-5.79	-8.00
μ^∞ [Pa]	100.4	218.2	132.6	122.2
τ_1 [s]	4.68	4.31	0.18	0.19
$\mu_{1,1}$ [Pa]	106.4	-481.6	-66.9	-53.2
$\alpha_{1,1}$	1.89	-2.39	-17.99	-19.09
τ_2 [s]	62.43	598.81	499.20	490.30
$\mu_{2,1}$ [Pa]	106.4	-144.0	-74.4	-68.9
$\alpha_{2,1}$	1.89	-4.56	-6.32	-6.42
μ^0 [Pa]	301.34	1122.7	969.9	851.8
σ_0 [Pa]	-	-	-	315.28
ϵ_0^p	-	-	-	0.30

Table 3.4: GAs material parameter estimates for monotonic tests on brain tissue in [57]

response is best fitted with negative $\{\mu, \alpha\}$ pairs, and that the inclusion of plastic behavior significantly increases the fitness performance.

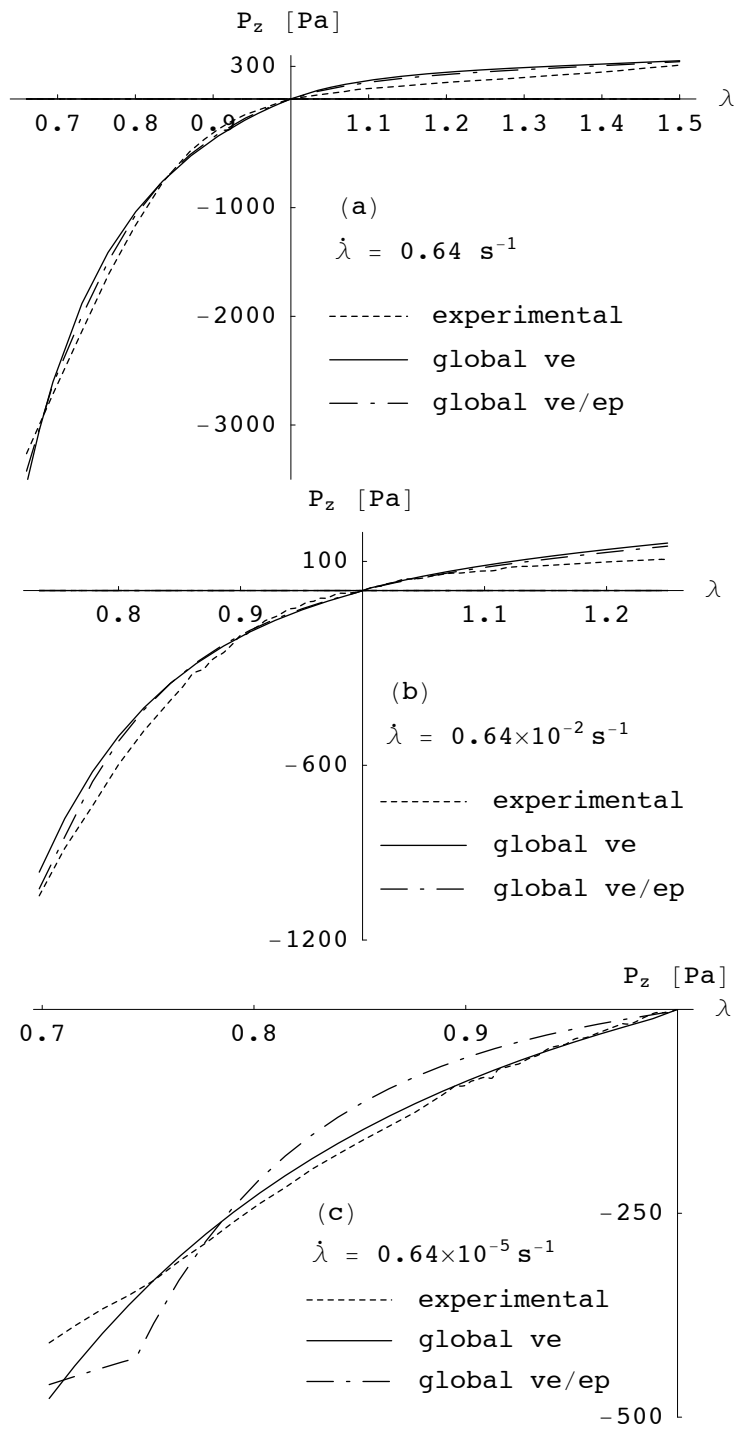


Figure 3.9: Global viscoelastic (ve) and viscoelastic/elastoplastic (ve/ep) fits of experiments in [57]

Miller et al. [57] estimated $\mu^0 = 156$ Pa, $\mu^\infty = 842$ Pa, $\alpha_1 = \alpha_{1,1} = \alpha_{2,1} = -4.7$, through a simplified "finite linear" viscoelastic model, accounting for large deformations and small perturbations away from thermodynamic equilibrium. Those results are in good agreement with the global GAs estimates of Tab. 3.4. The same authors estimated $\tau_1 = 0.50$ s and $\tau_2 = 50.0$ s, that is, a second relaxation time about 10 times smaller than our global estimates ($\tau_2 \approx 500$ s, cf. Tab. 3.4). It is worth noting that the finite viscoelastic model converges more rapidly toward thermodynamic equilibrium than finite linear viscoelastic theories (cf. [81]). This implies that larger relaxation times are needed in order to extend the viscous effects over time.

A final set of estimates was obtained considering the cyclic quasistatic uniaxial tests performed by [30] on human brain tissue excised during autopsy. Two one-cycle compression-tension (first compression and then tension), tension-compression tests (Fig. 1 of [30]), and a multi-cycle test (Fig. B.3 of [30]) performed on prismatic specimens of white matter harvested from different brain regions were examined. In the latter case, the first three cycles of a 20-cycle test were analyzed, activating three viscoelastic networks and plastic rate effects.

The GAs material parameter estimates and a comparison between experimental and fitting curves are illustrated in Tab. 3.5 and Figs. 3.10 and 3.11. It is evident from the figures that the presented model is able to capture hysteresis, strong non-linearity, different behavior in tension and in compression, relaxation, preconditioning, and cyclic softening of brain tissue. The results of Tab. 3.5 show that human brain samples analyzed by [30] manifest higher initial and long term shear moduli in comparison with the pig brain samples tested by [57] (cf. Tab. 3.4)

Fit Type	compr-tens	tens-compr	3 cycles
μ_1 [Pa]	-297.29	-659.71	-69.81
α_1	-2.98	-30.0	-40.0
τ_1 [s]	19.81	2.13	0.57
$\mu_{1,1}$ [Pa]	-223.89	-133.37	-610.73
$\alpha_{1,1}$	-6.31	-2.02	-23.76
τ_2 [s]	211.17	207.57	7.62
$\mu_{2,1}$ [Pa]	2.05	109.30	-4.95
$\alpha_{2,1}$	21.55	15.26	-1.00
τ_3 [s]	-	-	24.58
$\mu_{3,1}$ [Pa]	-	-	74.67
$\alpha_{3,1}$	-	-	1.00
ϵ_0^p	1.0e-4	0.176	7.6e-4
n	10.0	7.51	1.78
$\dot{\epsilon}_0^p$ [s ⁻¹]	-	-	0.01
m	-	-	14.35

Table 3.5: GAs material parameter estimates for [30] tests on specimens of brain white matter

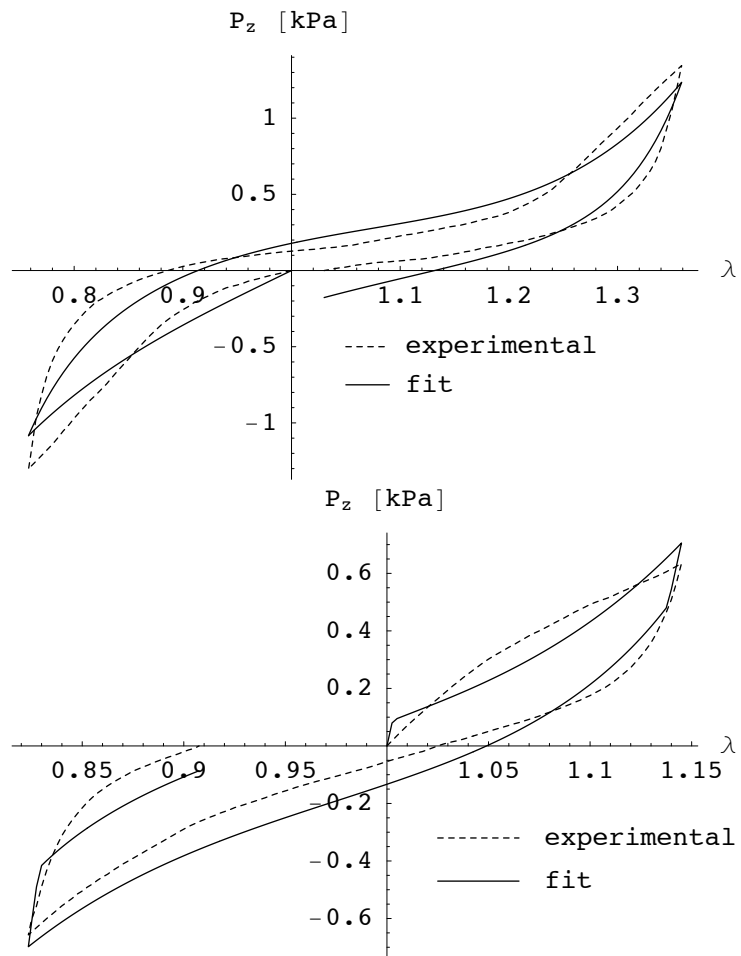


Figure 3.10: Fits of Franceschini et al. one-cycle compression-tension (a) and tension-compression (b) tests on specimens of white matter (cf. [30], Fig. 1)

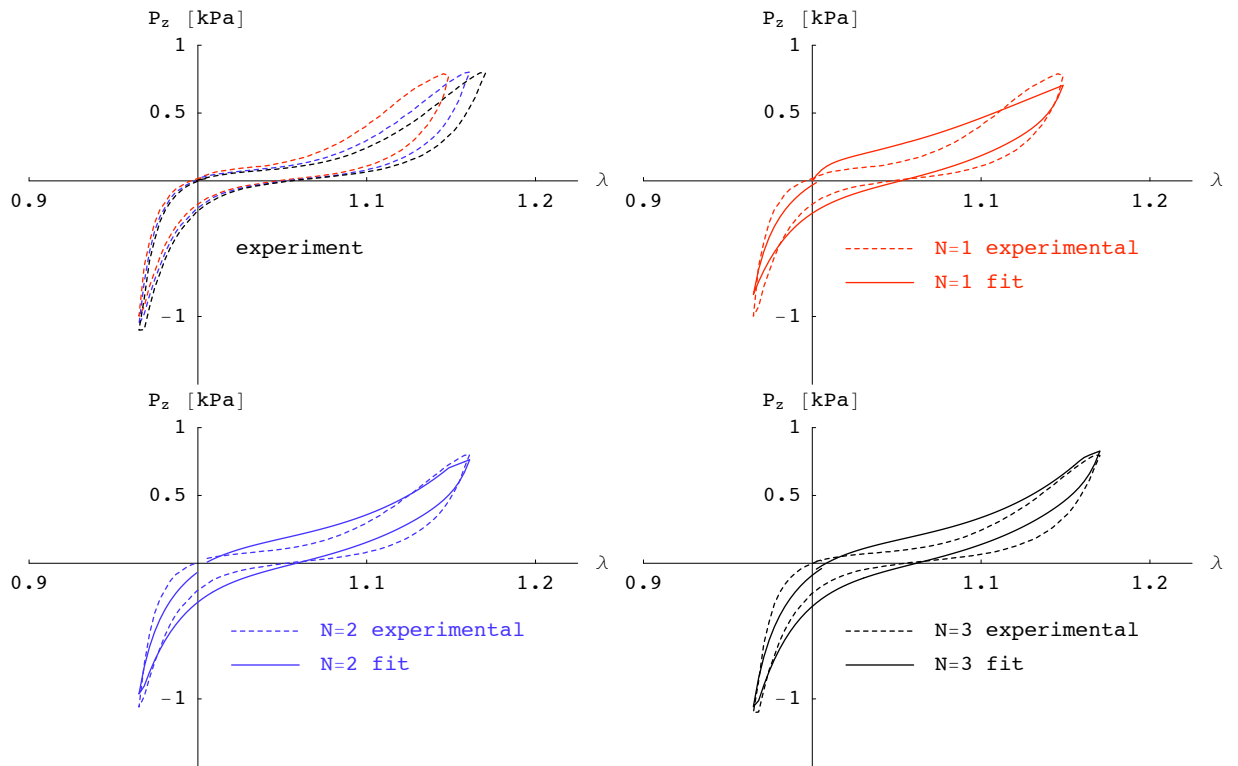


Figure 3.11: Fits of Franceschini et al. cyclic tests on a specimen of white matter (cf. [30], Fig. B.3, first three cycles)

Chapter 4

Application to ballistic and blast impact on composite plates and shells

4.1 Introduction

The need for effective, light, and easily applied protective armors has become an aggressively sought objective of the U.S. armed forces. Elastomeric polymers have recently been identified as promising for purposes of mitigating powerful explosions and retaining structural fragments caused by such loads. The polymers are sprayed on as a lightweight monolithic coating, do not contain volatile organic compounds, and can be made fire resistant. Three-quarter-inch spray-on coatings are presently being applied by the military in Iraq to the doors and side panels and below the floor of Humvees. Tests have determined that, when sprayed on three-sixteenth-inch steel armor, the coatings offer the same protection as three-eighth-inch armor, but at a much reduced weight. Thus, three-quarter-inch coating deflects most small-arms fire and a good percentage of explosive devices. The reinforced armor not only helps absorb the blast effects of roadside bombs, but also prevents the vehicles' metal from fragmenting and harming its occupants.

Different types of reinforcements have been investigated by several researchers. Hybrid light-weight fiber-reinforced polymer-matrix composite laminate armor has been analyzed by Grujicic et al. [38] using a two-dimensional axisymmetric model without fracture. That type of armor is constructed using various combinations and stacking sequences of a high-

strength/high-stiffness carbon fiber-reinforced epoxy (CFRE) and a high-ductility/high-toughness Kevlar fiber-reinforced epoxy (KFRE) composite laminates of different thicknesses [38]. It is found that the armor consisting of one layer of KFRE and one layer of CFRE, with KFRE laminate constituting the outer surface of the armor, possesses the maximum resistance towards the projectile-induced damage and failure [38].

Laminated composites have shown good potential in reducing armor weight compared to steels for the same ballistic protection, as they maintained 26% weight saving compared to steel according to Ubeyli et al. [90]. Also, the ballistic properties of flax, hemp, and jute fabric reinforced polypropylene composites processed by hot compression moulding were investigated by Wambua et al. [92]. The composites' ballistic effect was examined by investigating the ballistic limit of composite-steel hybrid systems prepared by gluing thin mild steel plates on the face and rear of the natural fiber composites [92]. Flax composites exhibited better energy absorption than hemp and jute composites and failed by shear cut-out, delamination, and fiber fracture [92]. It was found that the ballistic properties of the hemp composites increased significantly when a mild steel plate was used as facing and backing [92]. Lin et al. have derived analytical solutions for the deformation, penetration, and perforation of composite plates and sandwich panels subjected to quasi-static punch indentation and projectile impact [49]. A generalized solution methodology for the projectile impact on such structures was developed based on the contact load duration, the through-thickness and the lateral transit times [49]. These results also lacked comprehensive contact and fracture models. The ballistic properties of Kevlar 29/Polivnyl Butyral and Polyethylene fiber composites used in the light armor design were analyzed experimentally and numerically by Colakoglu et al. [23]. Higher elastic modulus and strength of Polyethylene composite resulted in a better ballistic performance [23].

In the following sections, the ballistic impact of a high-speed projectile on a polyurea-retrofitted DH36 steel plate is investigated. In Section 4.2.1, the localization elements approach utilized in this study is outlined. The formulation of the contact potential used to model the impact forces is summarized in Section 4.2.2. Then, in Section 4.2.3, the

experimental setup for the composite plate shot is detailed. Quantitative and qualitative validation is discussed in Section 4.2.4.

4.2 Ballistic impact on composite plates

4.2.1 Localization elements

Due to the high strain rate imposed by the ballistic impact, the use of a class of finite elements developed in [96] is proposed for capturing sub-grid localization processes such as shear bands and void sheets. The elements take the form of a double surface and deform in accordance with an arbitrary constitutive law — in particular, they allow for the development of displacement and velocity jumps across volume element boundaries [97].

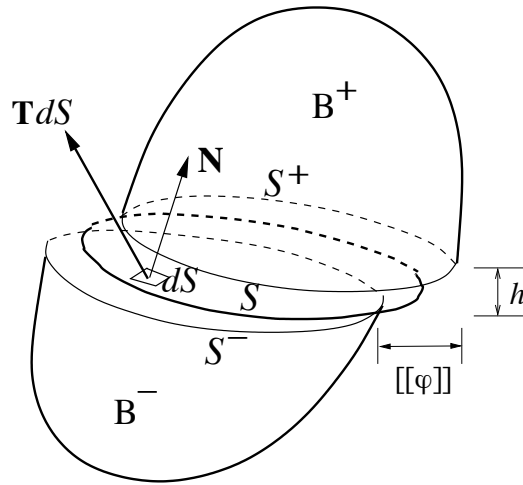


Figure 4.1: Localization surface in a three-dimensional body. S^+ and S^- are the top and bottom (smooth) surface of band attached to the sub-body B^+ and B^- , respectively. T is the traction acting on the mid-surface S .

The thickness of the localized zone is set by an additional field variable which is determined variationally. The localization elements are inserted, and become active, only when localized deformations become energetically favorable. The implementation is three dimensional and allows for finite deformations.

Strain localization is strictly regarded as a *sub-grid* phenomenon and, consequently, the bands of strain localization are modeled as *displacement discontinuities*. These displacement discontinuities are confined to volume-element interfaces and are enabled by the insertion of specialized *strain-localization elements*. These elements consist of two surfaces, attached to the abutting volume elements, which can separate and slip relative to each other. The kinematics of the strain-localization elements are identical to the kinematics of cohesive elements proposed by Ortiz and Pandolfi [73] for the simulation of fracture. In contrast to cohesive elements, the behavior of strain-localization elements is governed directly by the same constitutive relation which governs the deformation of the volume elements. As is evident from dimensional considerations alone, the transformation of displacement jumps into a deformation gradient requires the introduction of a length parameter, namely, the band thickness. The band thickness is optimized on the basis of an incremental variational principle [76, 98]. This optimization takes the form of a configurational-force equilibrium and results in a well-defined band thickness.

4.2.2 Modeling contact forces

A validation of the ballistic impact on a polyurea-reinforced steel plate requires the implementation of a contact potential algorithm capable of recreating the physical contact and frictional forces arising from the projectile impact. The contact capability developed in [69] is proposed to model the forces which arise from the impact between the projectile and the target plate. The following summarizes the contact algorithm:

Let the kinetic energy of the body be given by

$$T(\dot{\varphi}) = \int_{B_0} \frac{1}{2} \rho_0 \dot{\varphi} \cdot \dot{\varphi} dV_0, \quad (4.1)$$

in which φ is the position, dV_0 is a material or referential differential of volume, and ρ_0 is the mass density in the reference configuration.

The potential energy of the body has contributions from the strain energy from the bulk

material, the applied load, the body forces, and an indicator function that plays the role of the contact potential, as follows

$$\begin{aligned}
 V(\varphi) = & \int_{B_0} w(F) dV_0 - \int_{B_0} \rho_0 b \cdot \varphi dV_0 + \\
 & + \int_{\partial_t B_0} [I_C(\varphi) - t \cdot \varphi] dS_0
 \end{aligned} \tag{4.2}$$

in which φ is the position, F is the deformation gradient, $w(F)$ is the stored energy function for the bulk material, dV_0 is a material or referential differential of volume, b is the body force density per unit mass, $\partial_t B_0$ is the part of ∂B_0 in which the boundary traction t is specified, and $I_C(\varphi)$ is an indicator function defined as

$$I_C(\varphi) = \begin{cases} 0, & \text{if } \varphi \in C, \\ \infty, & \text{otherwise,} \end{cases} \tag{4.3}$$

in which C is the set of admissible configurations φ in which interpenetration does not occur [44].

The Lagrangian function for the body is then

$$L(\varphi, \dot{\varphi}) = T(\dot{\varphi}) - V(\varphi), \tag{4.4}$$

which gives rise to the action integral

$$I[\varphi] := \int_0^T L(\varphi, \dot{\varphi}) dt, \tag{4.5}$$

which, according to Hamilton's variational principle, yields the equation of motion for the system when extremized.

The action integral (4.5) reaches an extremum when its variation with respect to its independent variables is zero, as follows

$$\begin{aligned} \delta I &= \int_0^T \left(\int_{B_0} (\rho_0 b \cdot \delta \varphi - P : \delta F - \rho_0 \ddot{\varphi} \cdot \delta \varphi) dV_0 + \int_{\partial_t B_0} (t - F^{\text{con}}) \cdot \delta \varphi dS_0 \right) dt \\ &= \int_0^T \left(\int_{B_0} (\nabla \cdot P^T + \rho_0 b - \rho_0 \ddot{\varphi}) \cdot \delta \varphi dV_0 + \int_{\partial_t B_0} (t - F^{\text{con}} - P \cdot N) \cdot \delta \varphi dS_0 \right) dt = 0 \end{aligned} \quad (4.6)$$

in which $F^{\text{con}} := \partial I_C(\varphi)/\partial \varphi$ are the contact forces. The Euler-Lagrange equation corresponding to (4.5) is then

$$\begin{aligned} \nabla \cdot P^T + \rho_0 b &= \rho_0 \ddot{\varphi} \quad \text{on } B_0, \\ P \cdot N + F^{\text{con}} &= t \quad \text{on } \partial_t B_0, \\ t &= \mathbf{0} \text{ on } S_0. \end{aligned} \quad (4.7)$$

The admissible configurations in which interpenetration does not occur are such that

$$\varphi \in C \iff g_\alpha(\varphi) \geq 0, \quad \alpha = 1, \dots, N_p \quad (4.8)$$

in which $g_\alpha(\varphi)$ are constraints that prevent penetration, and N_p is the number of such constraints. One choice for the constraint functions is the interpenetrating distances between the surface defined by the contact potential and the target. In this way N_p becomes the number of interpenetrating distances. The indicator function can then be approximated as

$$I_C(\varphi) \approx k \sum_{\alpha=1}^{N_p} g_\alpha^3(\varphi), \quad (4.9)$$

in which k is a penalty parameter.

4.2.3 Composite plate shot experimental setup

The experiment to be validated was performed by Bill Mock et al. [60] at the research gas gun facility of Naval Surface Warfare Center (Dahlgren Division) (see Fig. 4.2.). A 4340 steel impactor is launched as shown in Fig. 4.3 at a composite circular plate comprising DH36 steel and polyurea casted on (see Tab. 4.1 for shot details). The impactor strikes the target plate on the steel side at a speed of 280.9 m/s causing it to deform significantly along with the polyurea coating. Displacement profiles at various times are recorded and later compared to the validation run.

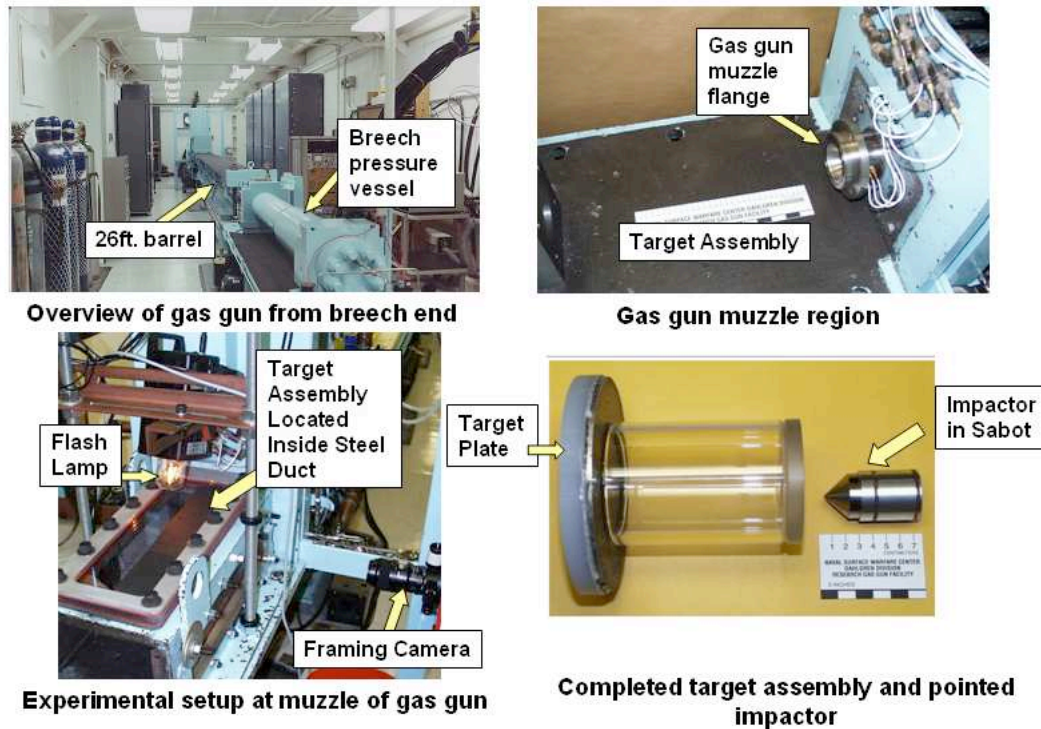


Figure 4.2: Naval Surface Warfare Center (Dahlgren Division) Research Gas Gun Facility (Courtesy of Bill Mock et al. [60])

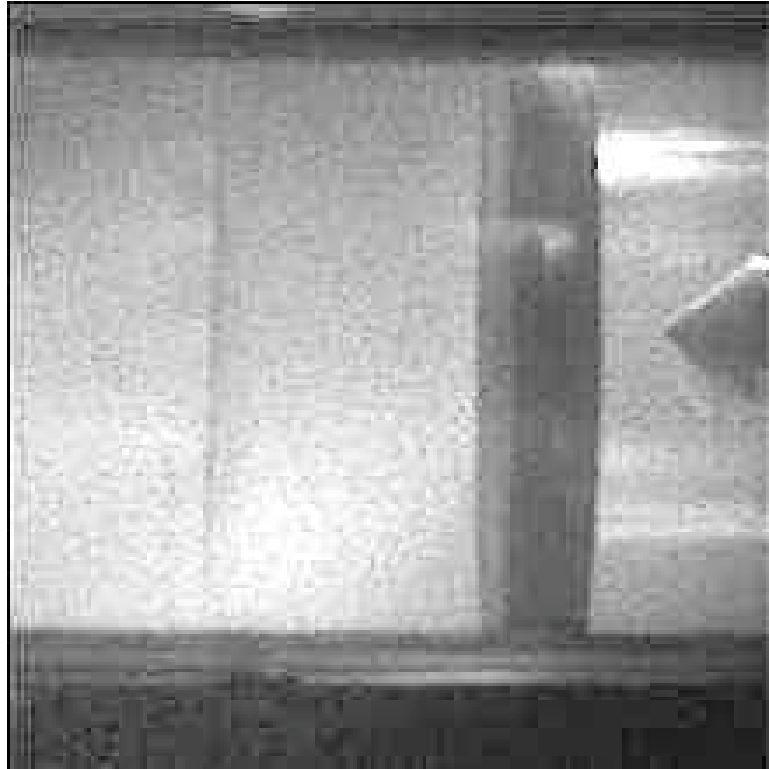


Figure 4.3: Impactor (right) about to strike target composite plate (left)

Impactor mass [gm]	145
Impactor hardness [RC]	36
DH36 steel target plate mass [gm]	692.2
DH36 steel target plate diameter [mm]	154.2
DH36 steel target plate average thickness [mm]	4.75
Polymer mass [gm]	230.1
Polymer diameter [mm]	154.2
Polymer thickness [mm]	11.1
Polymer/steel thickness ratio	2.335
Impact speed [m/s]	280.9

Table 4.1: Shot parameters

4.2.4 Validation

Due to all of the polyurea fits obtained in Chapter 3 being at the material point, the polyurea bulk behavior needs to be identified before the shot experiment is to be validated. For this particular shot experiment, the polyurea approximately elongates to a strain of 0.104 (by observing the displacement results) during the first 270 microseconds, resulting in a strain rate of 380/s. The 408/s strain rate material parameters obtained in Section 3.3 were used in a 3-dimensional finite element simulation of a release wave experiment (see Fig. 4.4) conducted by Clifton et al. at Brown University with an impact velocity of 218.2 m/s.

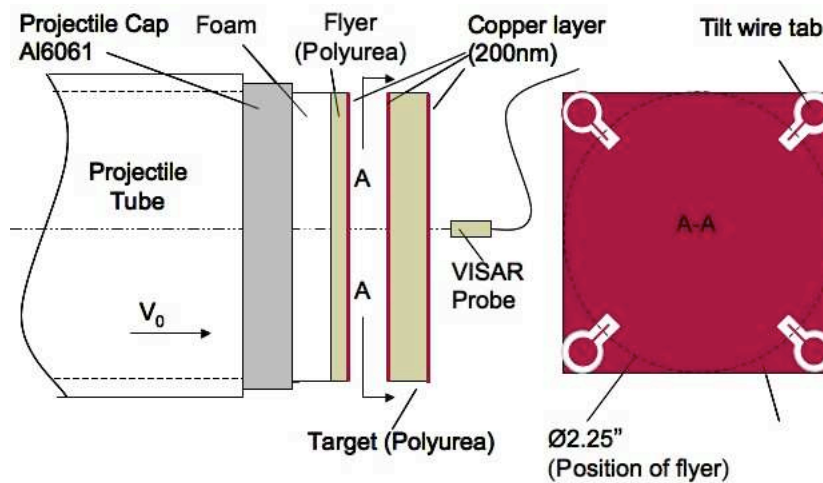


Figure 4.4: Polyurea release wave experiment set up by Clifton et al. [22]

The existence of voids in polyurea was observed in the microstructure of the spall area (Fig. 4.5) which called for the activation of volumetric plasticity in the model. Contact was also utilized in order to capture the effect of the reflected wave in the flyer as it passes through the interface and reaches the original wave in the target plate resulting in spall as shown in Fig. 4.6. The second peak in Fig. 4.7 is caused by the reflected wave from the spall plain reaching the free surface. Spall was captured in the validation via insertion of localization elements.

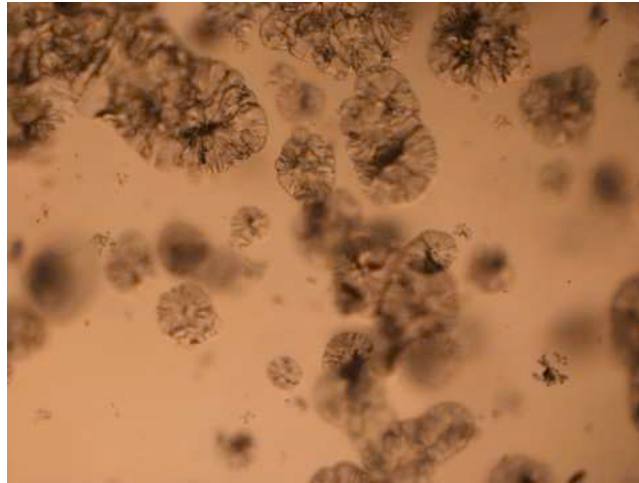


Figure 4.5: Microstructure of the damaged area in polyurea as a result of the release wave experiment [22]

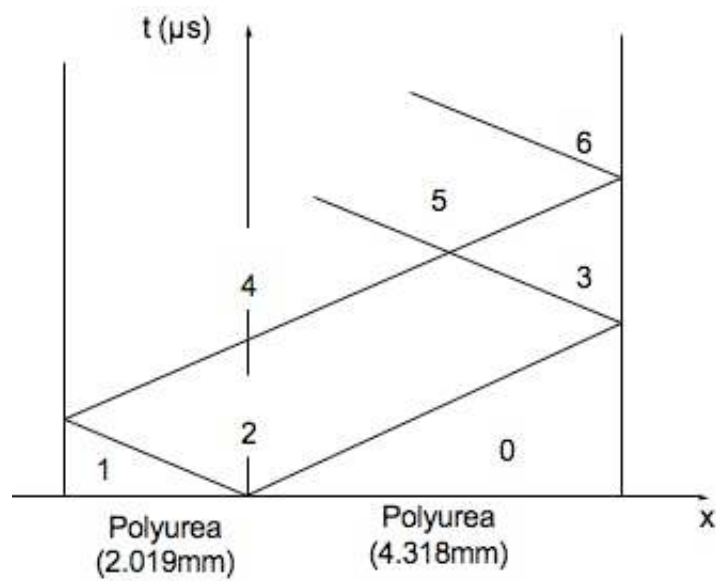


Figure 4.6: T-x diagram of the release wave experiment [22]

The simulated normal velocity of the target free surface is shown to be in good agreement with the experimental results (see Fig. 4.7). The bulk parameters obtained for this validation are shown in Tab. 4.2. It is important to note that cyclic tests, which include

tension and compression, are needed in order to obtain a more comprehensive set of parameters.

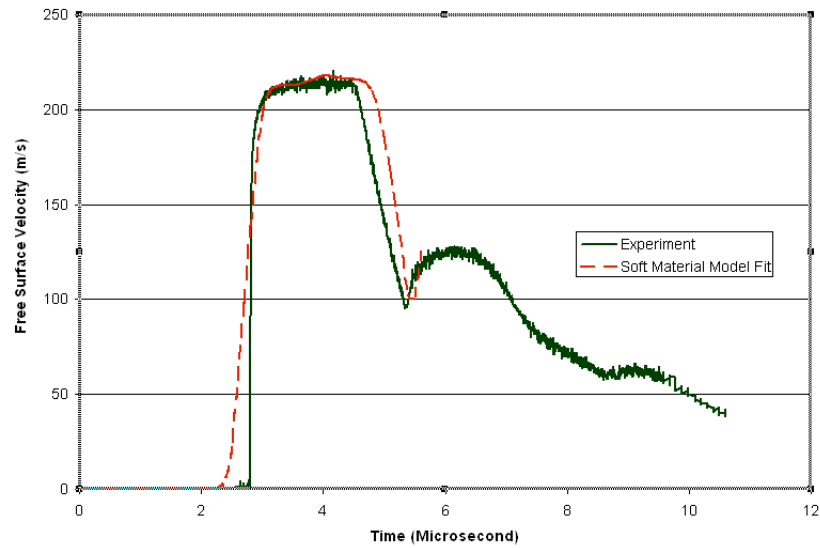


Figure 4.7: Free surface normal velocity vs. time [22]

ρ	1070
ν	0.495
Void radius a_0 [m]	81.6×10^{-7}
Void density N_v [voids/ m^3]	2.89×10^{12}
μ_1 [Pa]	150
α_1	7.5
μ_2 [Pa]	150
α_2	7.5
μ_3 [Pa]	150
α_3	7.5
τ_1 deviatoric [s]	4.90×10^{-4}
τ_1 volumetric [s]	4.90×10^{-4}
$\mu_{1,1}$ [Pa]	2.6×10^6
$\alpha_{1,1}$	5.0
$\mu_{1,2}$ [Pa]	2.6×10^6
$\alpha_{1,2}$	5.0
$\mu_{1,3}$ [Pa]	2.6×10^6
$\alpha_{1,3}$	5.0
τ_2 deviatoric [s]	9.94×10^{-3}
τ_2 volumetric [s]	9.94×10^{-3}
$\mu_{2,1}$ [Pa]	0.95×10^6
$\alpha_{2,1}$	4.5
σ_0 [Pa]	6.0×10^6
ϵ_0^p	1.0
n	0.003

Table 4.2: Material parameter estimates for release wave experiment on polyurea [22]

A mesh comprising 25605 tetrahedral elements was constructed in adherence to the

dimensions outlined in Tab. 4.1. The model outlined in this work was utilized for polyurea with the activation of thermal softening allowing for the formation of shear bands (thermal properties obtained from [45] and Primeaux Associates LLC are shown in Tab. 4.4.) The parameters obtained for polyurea in Section 3.3 and Tab. 4.2 were assigned to the polyurea elements. A porous plasticity model outlined in [94] was utilized for the DH36 steel with the material properties shown in Tab. 4.3. Friction was modeled as in [82] with values of 0.15 and 0.1 for the static and kinetic friction coefficients, respectively. The experimental displacement profiles were recorded at various times for the purpose of validation (see Fig. 4.8). The simulation was performed on 256, 2.4 GHz, Intel Xeon processors with 4 GB of memory shared between every 2 processors. The calculation lasted for approximately 72 hours to reach 297 microseconds. It is observed in the experiment that the composite target plate starts to move as a rigid body along with the impactor at approximately 200 microseconds. The simulation displacement profiles were consequently compared to the experimental results up to 208 microseconds with great agreement, as shown in Fig. 4.9. The final configurations are shown in Fig. 4.10 and contours of the plastic strain, volumetric strain, and temperature are shown in Figs. 4.11 and 4.12.

ρ	7700
E [GPa]	210.0
ν	0.29
σ_0 [Pa]	400.0×10^6
ϵ_0^p	0.004
n	6.0
$\dot{\epsilon}_0^p$ [s^{-1}]	0.001
m	60.0
T_0 [K]	293
T_m [K]	1371
C_v [$J\ Kg^{-1}\ K^{-1}$]	486.0
α [K^{-1}]	12.0×10^{-6}
l	0.75
β	0.9
Void radius a_0 [m]	5.2×10^{-9}
Void density N_v [voids/ m^3]	1.0×10^{22}

Table 4.3: Material parameter estimates for DH36 steel via fits to data in [64]

T_0 [K]	293
T_m [K]	500.0
C_v [$J\ Kg^{-1}\ K^{-1}$]	1.5×10^3
α [K^{-1}]	4.0×10^{-5}
l	1.0
β	0.5

Table 4.4: Thermal parameter estimates for polyurea

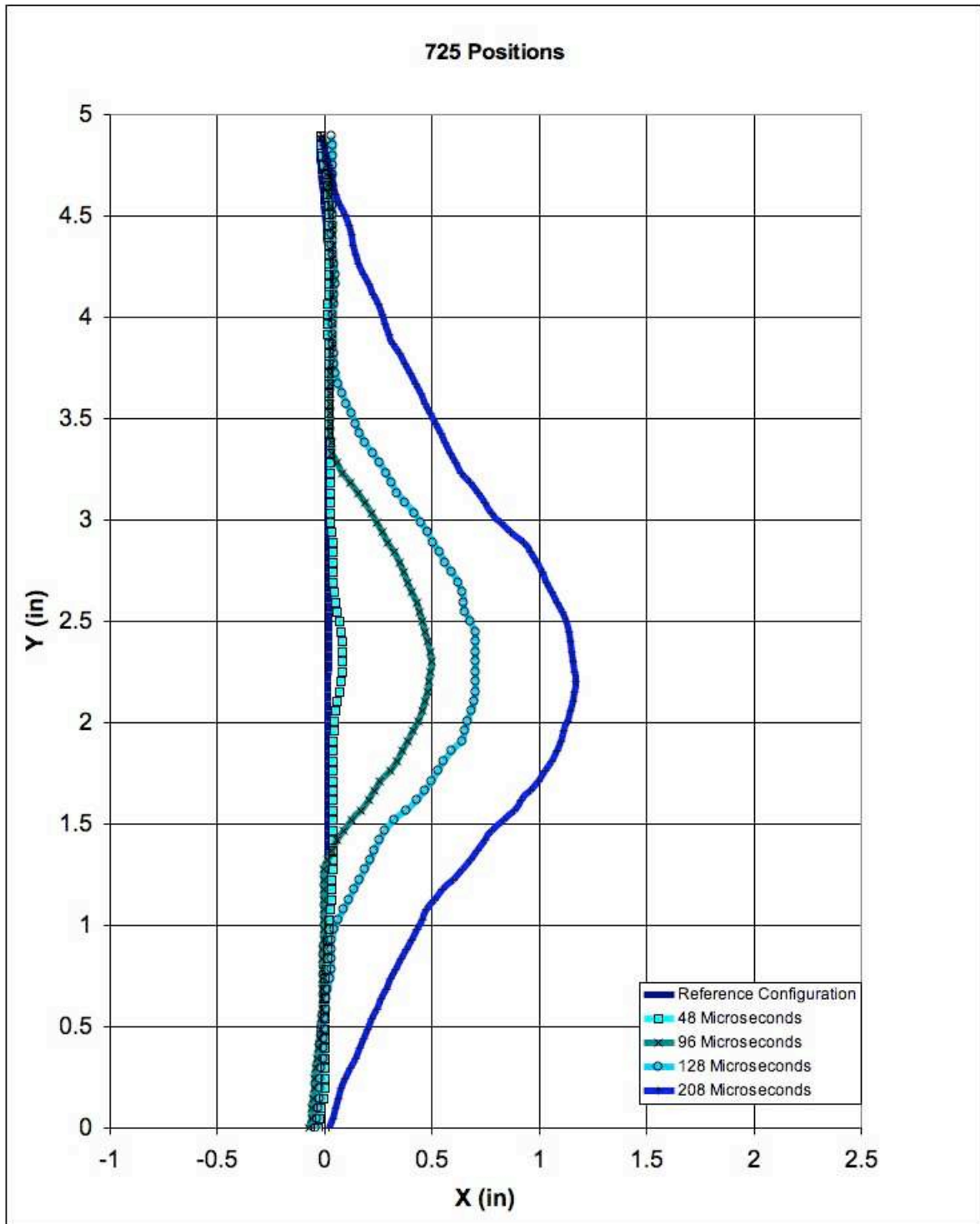


Figure 4.8: Composite plate positions at different times. Each color/symbol represents a time frame.

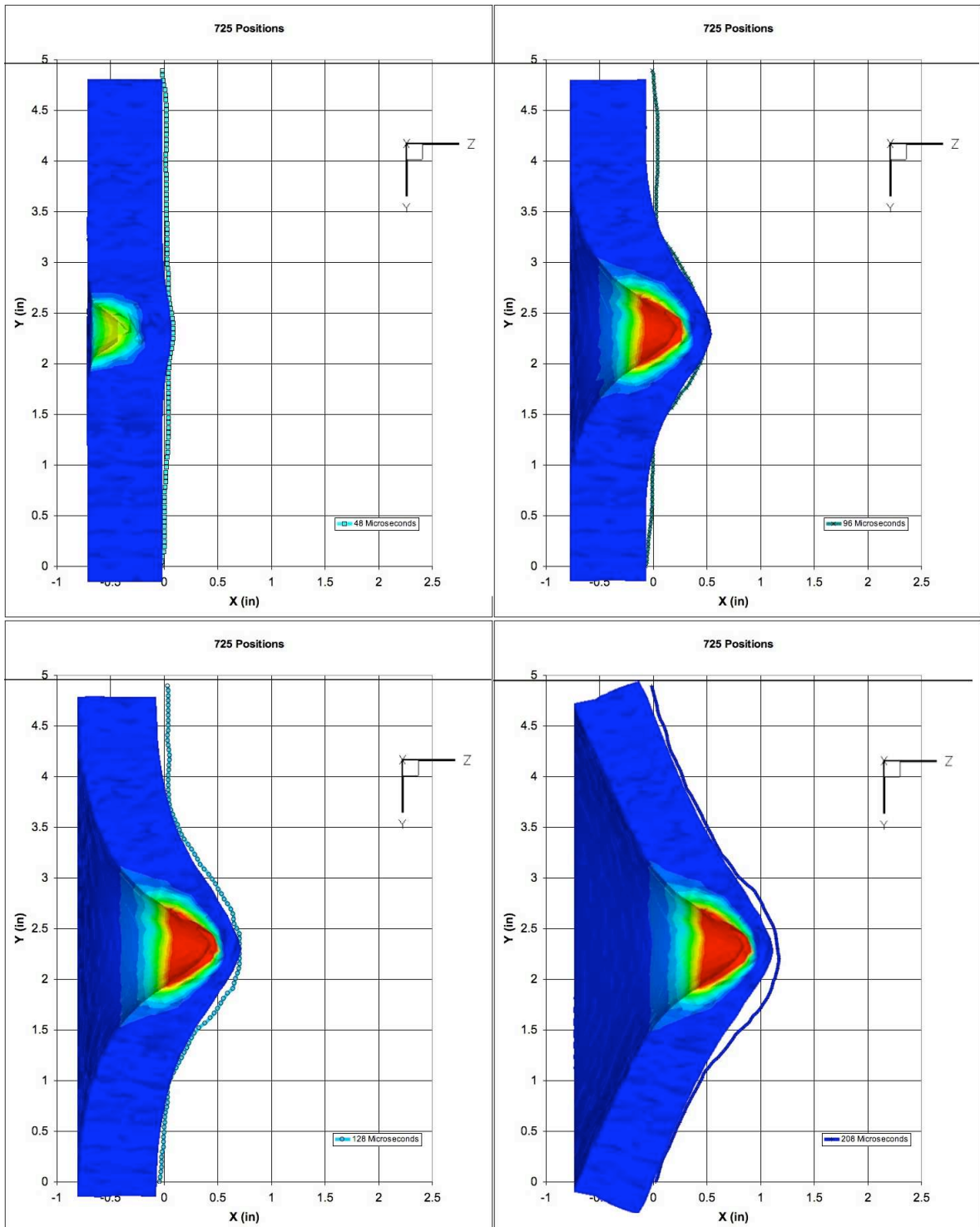
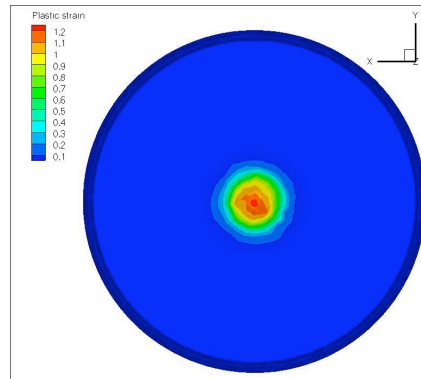


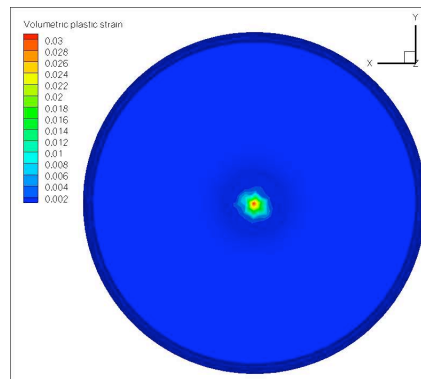
Figure 4.9: Experimental and computational displacements at various times



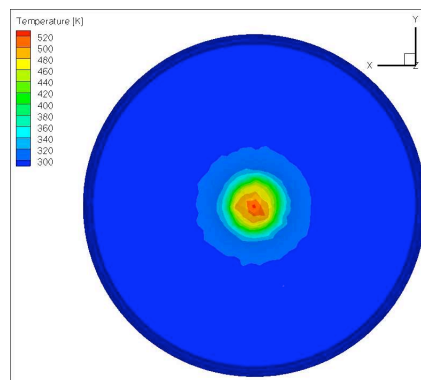
Figure 4.10: Experimental (top) and computational (bottom) final configurations



(a)

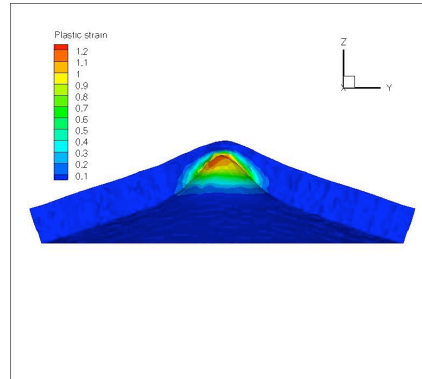


(b)

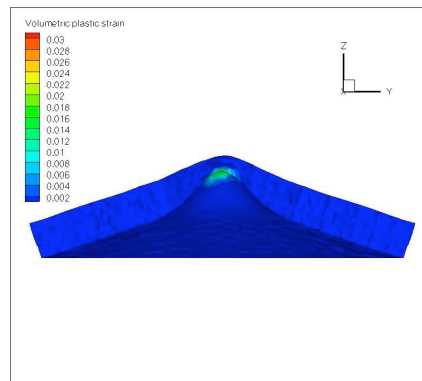


(c)

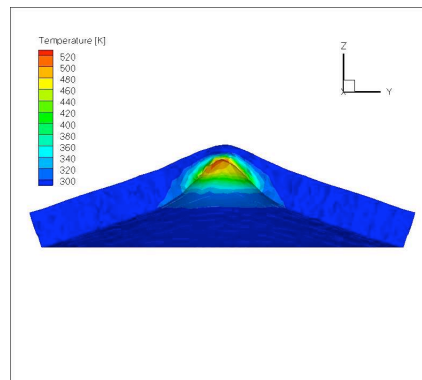
Figure 4.11: Plastic strain (a), volumetric strain (b), and temperature (c) contour plots from the impact side of the composite plate



(a)



(b)



(c)

Figure 4.12: Plastic strain (a), volumetric strain (b), and temperature (c) contour plots across the thickness of the composite plate

4.3 Blast impact on composite shells

4.3.1 Subdivision thin-shell elements

Within the framework of Kirchoff-Love theory, the strain energy density of thin shells is expressed in terms of the first and second fundamental forms of the shell middle surface. Therefore, a conforming finite element discretization requires smooth shape functions belonging to the Sobolev space H^2 . Cirak, Ortiz, and Schröder [19, 21] proposed a novel type of discretization based on the concept of subdivision surfaces which delivers smooth H^2 shape functions on unstructured meshes in a particularly natural and efficient way. The interpolation within one element is accomplished with shape functions which have support on the element as well as the one ring of neighboring elements (see Fig. 4.13)

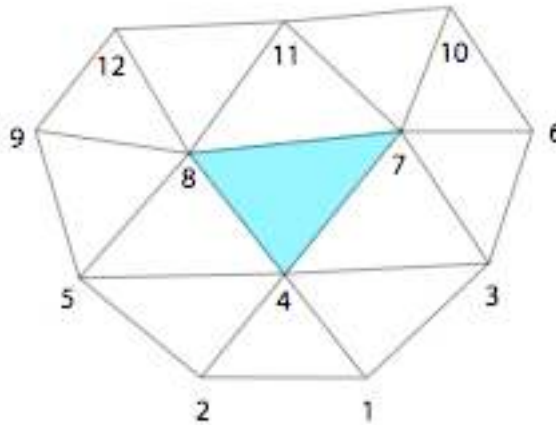


Figure 4.13: Support of shape functions of a subdivision element (central triangle)

The number of the control points N involved in the interpolation of each element depends on the local connectivity of the mesh. For example, for regular patches where each of the three element vertices are incident to six elements the interpolant derived from the Loop's subdivision scheme has $N = 12$ control points [51, 93]. The overlapping local interpolations, each over one patch, combined lead to a global interpolation with square integrable curvatures. In addition to several other advantages, an appealing feature of the

subdivision elements is that the sole unknowns in the finite element solution are the nodal displacements. However, this comes at a certain cost, namely, that the subdivision shape functions are non-local in the sense that the displacement field within one element depends on the displacements of the nodes attached to the element and the immediately adjacent ring of nodes in the mesh.

4.3.2 Shell fracture and fragmentation

In three-dimensional solids, cohesive laws of fracture have been successfully integrated into finite-element analysis by encoding them into cohesive elements in the form of double surfaces (e.g. [15, 71, 72, 74] and references therein). The opening of the cohesive elements is compatible with the deformation of the adjacent volume elements and is subject to a unilateral closure constraint. Cohesive elements may be inserted adaptively upon the attainment of a critical stress condition on the interelement boundary [15, 71, 74]. The insertion of cohesive elements introduces new surfaces into the mesh, which undergoes complex topological transitions as a result. For three-dimensional solids these transitions can be classified exhaustively [71, 74], and appropriate actions may be taken in order to update the representation of the mesh in each case. The natural extension of the cohesive element concept to shells consists of inserting cohesive elements at interelement edges, and constraining the opening of the cohesive elements to conform to the deformation of the middle surface of the shell and its normal. This approach allows for fracture both in an in-plane or tearing mode, a shearing mode, or a bending or hinge mode. However, within a subdivision-element framework the essential difficulty resides in making the scheme adaptive, in the sense of inserting cohesive elements in an otherwise conforming mesh upon the attainment of some appropriate critical condition. Thus, the non-locality of the displacement interpolation renders the tracking of the topological transitions induced by the insertion of cohesive elements unmanageably complex. In order to sidestep this difficulty, all the element edges are fragmented ab initio by duplication of common nodes [20], Fig. 4.14. In implicit calculations, element conformity prior to fracture is enforced by the ad-

dition of a penalty term to the energy. Alternatively, in explicit dynamics calculations conformity is readily enforced by a displacement averaging technique.

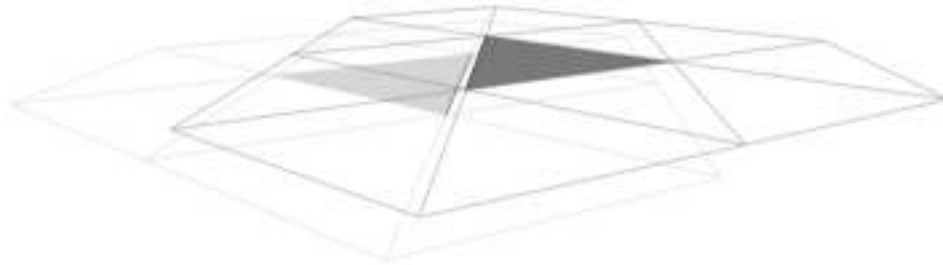


Figure 4.14: One cohesive edge and the two adjacent subdivision shell elements with their one-neighborhoods

4.3.3 DH36 steel/Polyurea composite hull

Laminated composite plates are simulated with n plies of thicknesses h_1, \dots, h_n by the simple device of disposing n integration points across the thickness of the plate and assigning polyurea and DH36 steel properties to the corresponding plies (see Fig. 4.15). This method applies equally well to shell and cohesive elements. In the case of shells the properties of DH36 steel are modeled by means of finite-deformation porous plasticity [94]; whereas the properties of polyurea are modeled by means of the model presented in this thesis. In the shell cohesive elements, the quadrature points corresponding to steel and polyurea layers are simply assigned the fracture properties of each material. Once the fracture criterion is fully satisfied for either material, the integration points belonging to that material become inactive and hence do not contribute to the composite shell deformation.

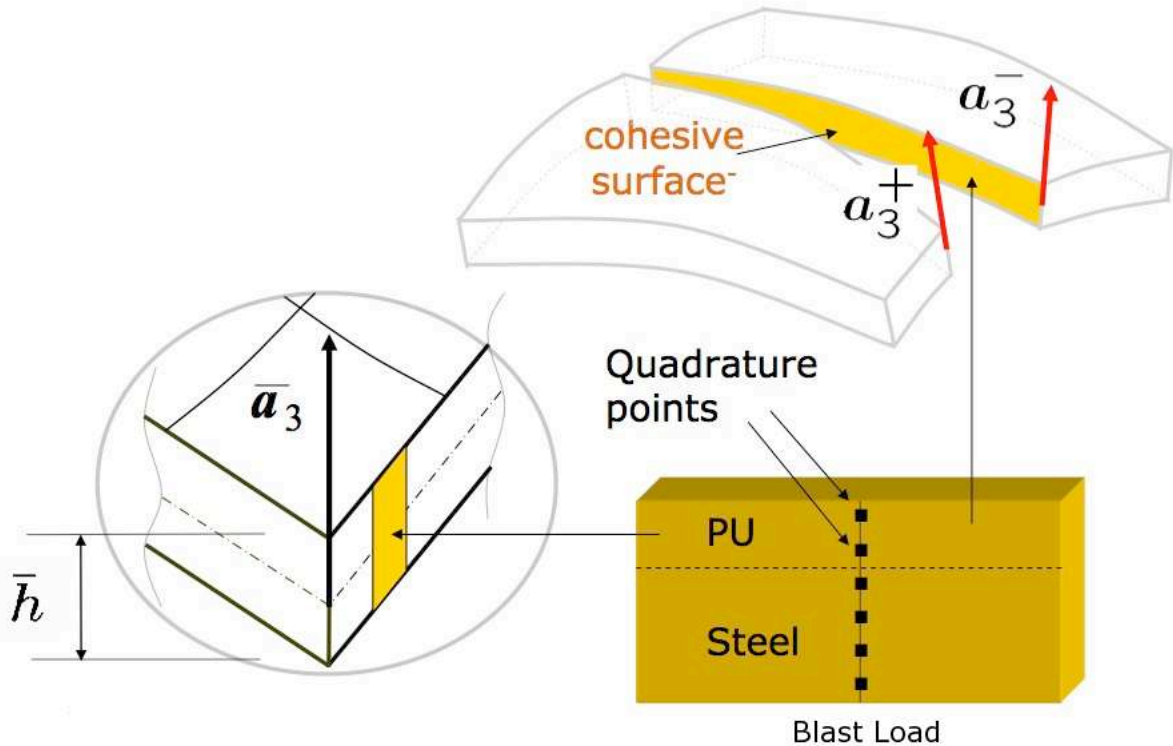


Figure 4.15: Composite shell formulation

An underwater blast pressure profile as in [29] is applied to a polyurea (located opposite of the blast side) retrofitted DH36 steel composite hull section taken from a Meko 140 corvette ship used by the Argentinean navy. The hull is modeled via shell elements with dimensions shown in Fig. 4.17 and formulation shown in Fig. 4.15. The loading conditions impose bending on the structure resulting in polyurea being in tension; the highest strain rate tension parameters obtained in Chapter 3 were assigned to the polyurea across-the-thickness integration points and the DH36 steel material parameters shown in Tab. 4.3 were assigned to the steel in the same fashion. The estimated fracture properties for both materials are shown in Tab. 4.5. An underwater 0.5 Kg TNT blast load is applied to the DH36 steel side of a 2880 shell-element mesh as shown in Fig. 4.16 with free boundary conditions. Two simulations were conducted; the first with a composite hull comprising 0.0048 mm DH36 steel and 0.01056 mm polyurea coating on the opposite side of the

blast load. The second with a 0.00625 mm DH36 steel hull without polyurea. Both hulls have approximately the same total mass of 3811 Kg. The kinetic energy of the two shells was plotted vs. time as shown in Fig. 4.27 with sample qualitative results shown in Fig. 4.26. Assuming that the starting hull thickness is 0.0048 mm of DH36 steel, the addition of 0.01056 mm of polyurea is almost equivalent to adding 0.00145 mm of DH36 steel with only an increase in the hull total kinetic energy of 4.2%. The advantages of adding polyurea vs. DH36 steel can be summarized into two main factors: ease of application and cheaper cost. This establishes a quantitative measure to improve the composite design by minimizing the kinetic energy resulting in larger absorption of the blast energy in finite deformation.

Material	DH36 Steel	Polyurea
Cohesive Stress (MPa)	1200	24
Fracture Energy G_c (N/m)	11905	37037

Table 4.5: DH36 steel and polyurea fracture parameters

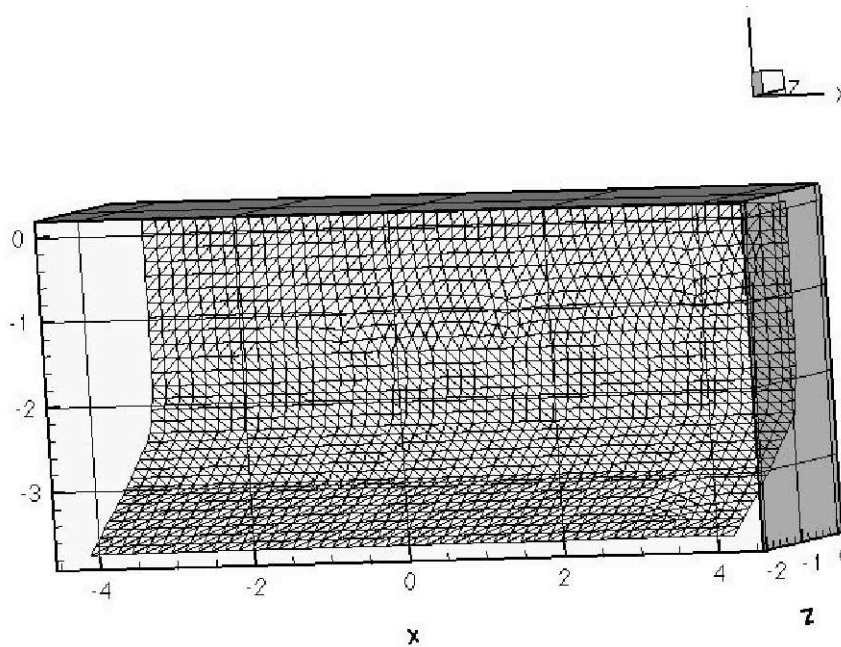


Figure 4.16: Hull mesh (2880 elements)

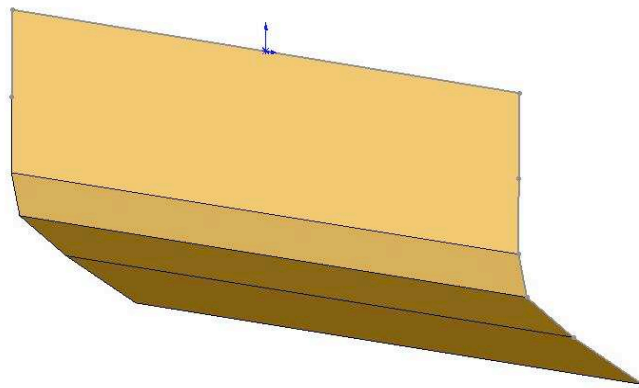
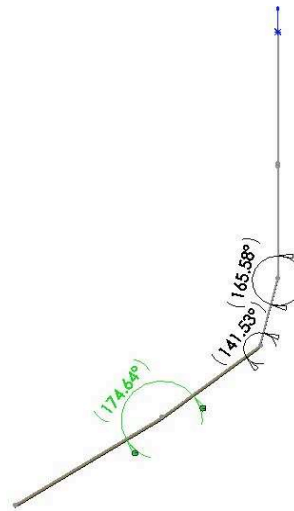
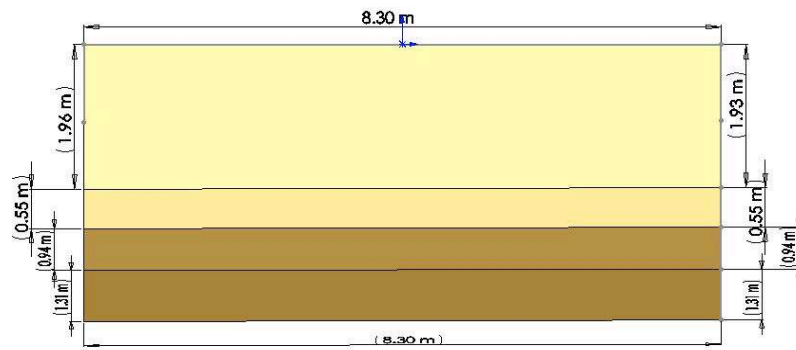
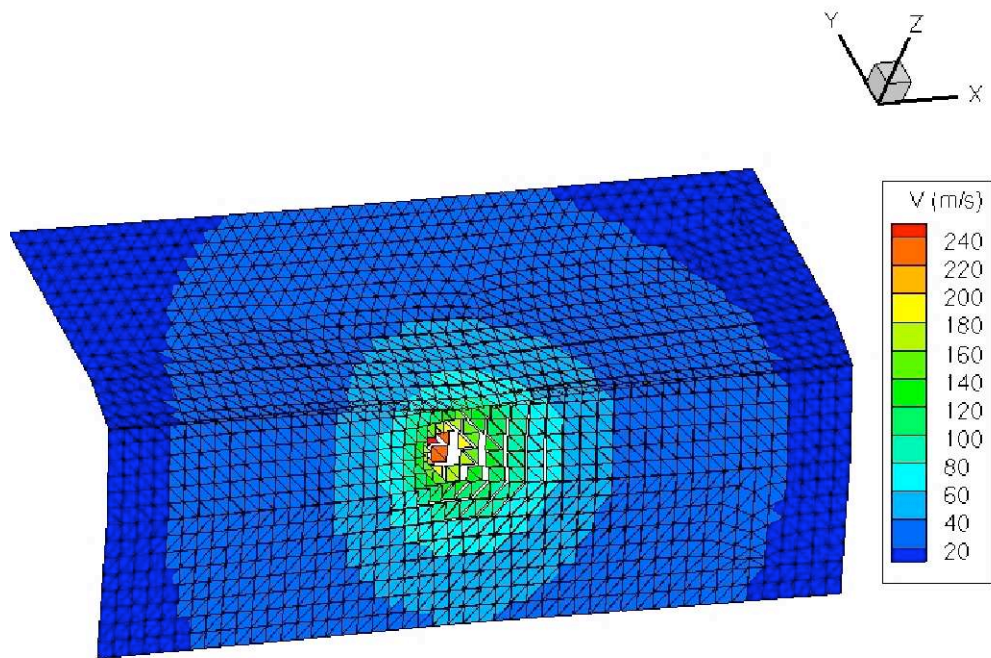
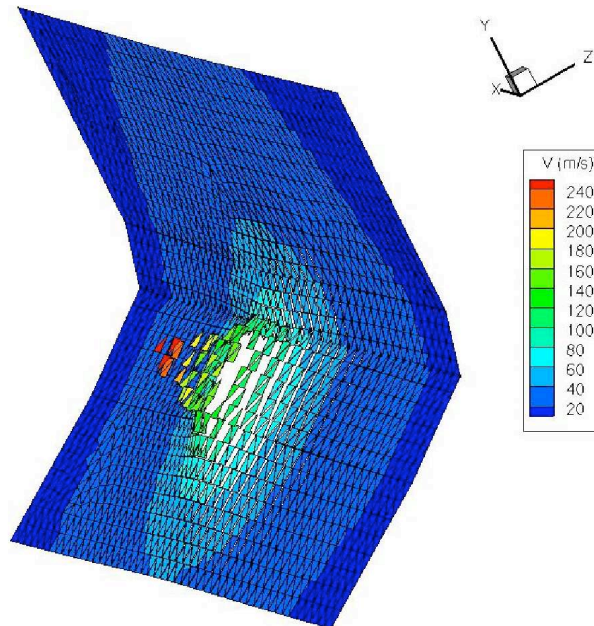


Figure 4.17: Hull front, side, and dimetric views (top to bottom)



(a)



(b)

Figure 4.18: Composite hull views during blast impact. Views are front (a) and side (b).

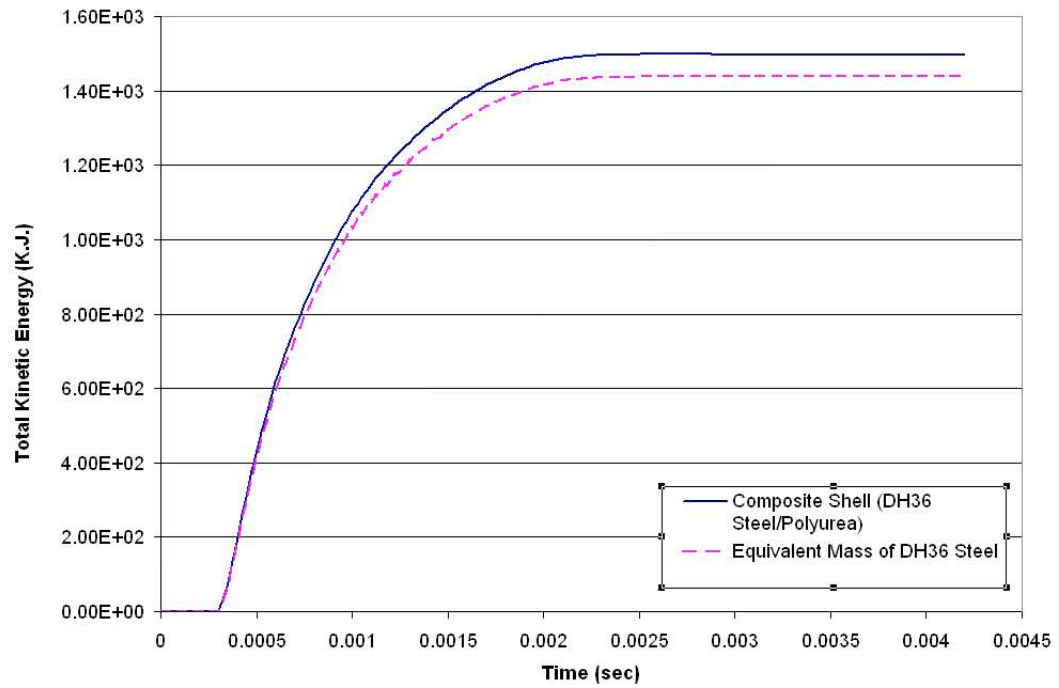


Figure 4.19: Hull kinetic energy vs. time for different configurations

4.3.4 Aluminum/PVC foam H100/Aluminum composite hull

Another composite hull configuration involves the use of Divinycell H100, a PVC foam with a density of 100 Kg/m^3 , in the hull central part of the thickness laminates (see Fig. 4.20). Aluminum and PVC properties are assigned to the corresponding plies as described in Section 4.3.3.

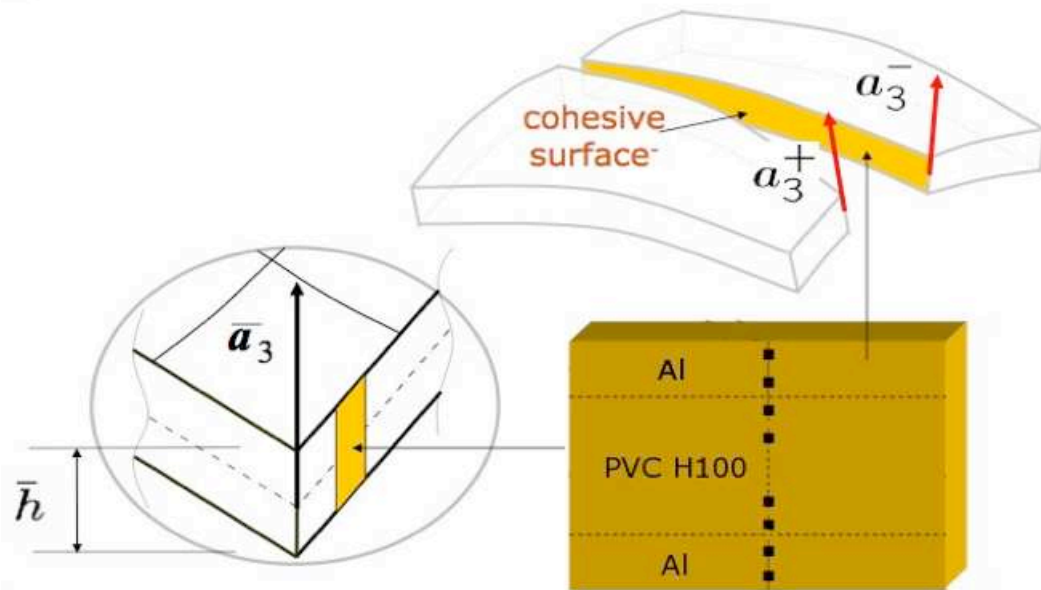


Figure 4.20: Composite shell formulation

4.3.5 PVC foam - Divinycell H100

The compressive behavior of PVC H100 is due to its cellular structure (Fig. 4.21). At very low compressive stress ($\leq \sim 2$ MPa), the cellular structure is able to support the load. As the compressive stress increases behind the first stress peak, the cells collapse, determining the plastic flow (Fig. 4.22). At high compressive strain, the material is compact due to the collapse of all the cells and its stiffness greatly increases as the loading continues. The overall uniaxial foam response in compression is shown in Fig. 4.23.

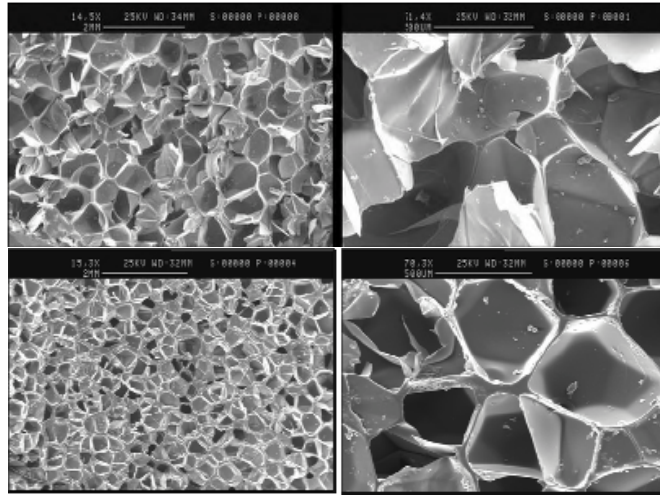


Figure 4.21: Cells structure of Divinycell H45 (top) and H130 (bottom)[7]

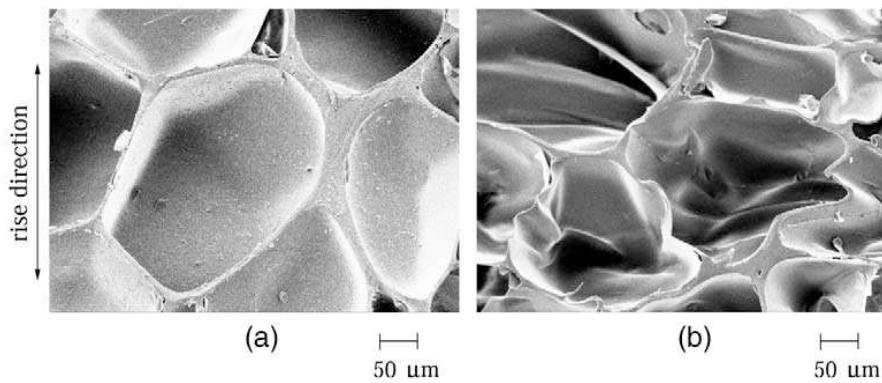


Figure 4.22: Photographs of a specimen of H200 foam sectioned along its mid-plane. Views are undeformed and uniaxially compressed to 10% from left to right.[25]

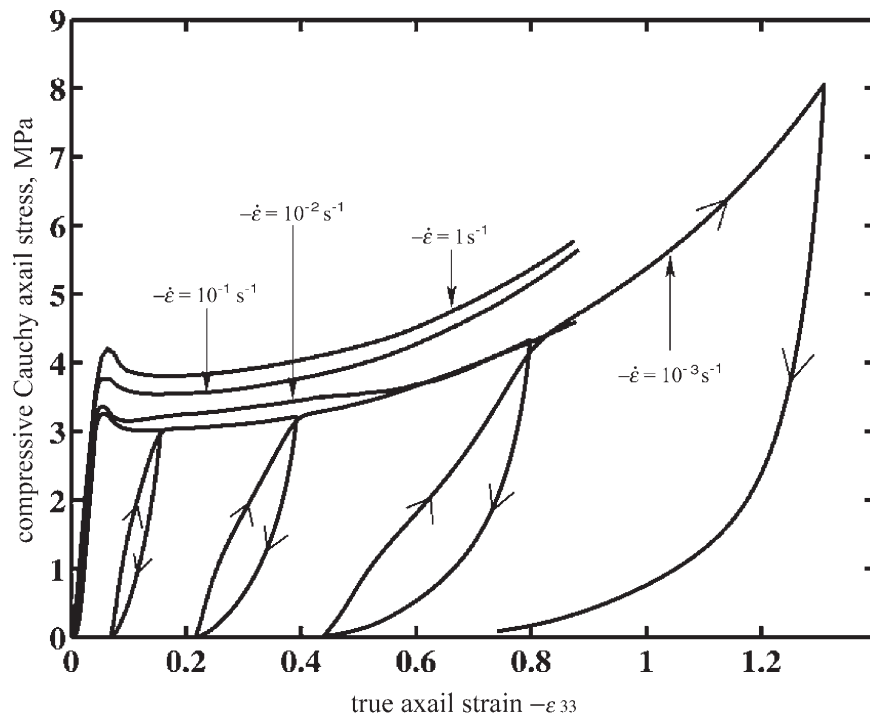
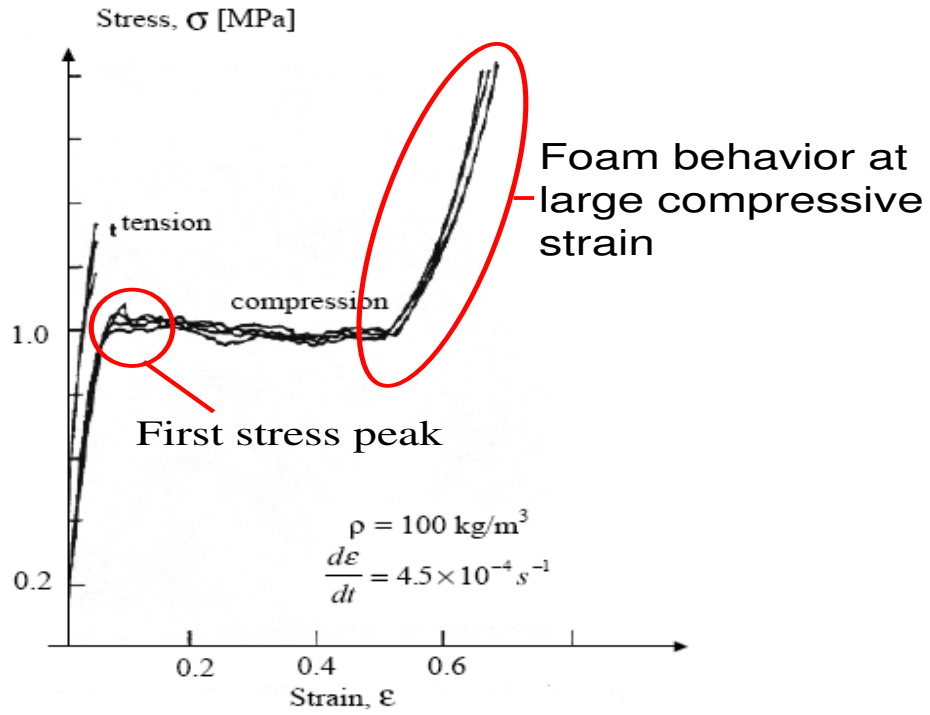


Figure 4.23: Foam uniaxial compressive behavior

Due to the lack of comprehensive stress-strain data for PVC H100, information provided in the literature for PVC foam, along with reported stress-strain trends (see Tab. 4.6), inspired the schematic uniaxial response of Divinycell H100 shown in Fig. 4.24. In uniaxial tension, the stress strain curve is, within a good approximation, linear elastic until rupture. In uniaxial compression, the PVC foam response may instead be subdivided into three different phases:

1. Initial linear elastic response until the first compressive stress peak is reached
2. Plastic deformation
3. Final stiffness gain.

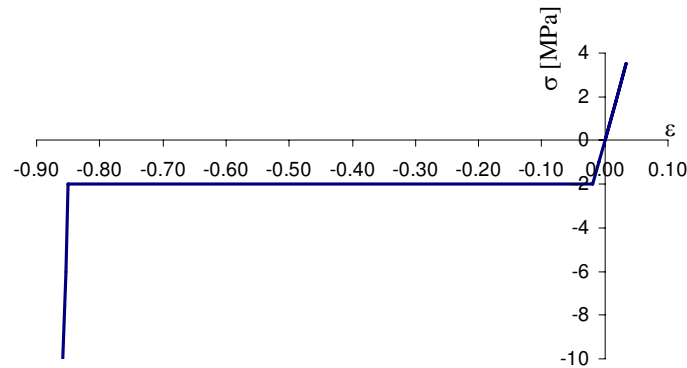


Figure 4.24: Schematic uniaxial stress-strain curve for Divinycell H100

All the values which characterize the response of the Divinycell H100 foam used in the following analysis are reported in Tab, 4.6, with σ_c being the compressive stress at which the slope of the stress-strain curve first changes. The calibrated soft material model parameters (without plasticity) at an assumed strain rate of 1 s^{-1} are shown in Tab. 4.7. Other sources report similar properties [1, 33, 13].

Fit Type	compression	tension
μ_1 [Pa]	-147.4	6.64×10^9
α_1	-5.5	10.0
μ_2 [Pa]	376.2	-
α_2	9.4	-
μ_3 [Pa]	-133.5	-
α_3	-14.1	-
τ_1 [s]	0.02	-
$\mu_{1,1}$ [Pa]	2.3×10^6	-
$\alpha_{1,1}$	10.0	-
$\mu_{1,2}$ [Pa]	-2.3×10^6	-
$\alpha_{1,2}$	-10.0	-
$\mu_{1,3}$ [Pa]	2.3×10^6	-
$\alpha_{1,3}$	10.0	-

Table 4.7: Soft material model parameter estimates for PVC H100 foam

ε_c	-0.85
E [MPa]	105.0
μ [MPa]	40.0
ν	0.32
E_f [MPa]	1000.0
σ_{ut} [MPa]	3.5
σ_c [MPa]	-2.0
σ_{uc} [MPa]	-50.0
K_{IC} [MPa \sqrt{m}]	0.1
G_{IC} [MPa m]	9.52×10^{-5}
δ_c [m]	5.44×10^{-5}

Table 4.6: Divinycell H100 material properties

ρ [Kg/m ³]	2734
E [GPa]	87.6
ν	0.31
σ_0 [Pa]	275.0×10^6
ϵ_0^p	0.1
n	25.0
$\dot{\epsilon}_0^p$ [s ⁻¹]	0.001
m	500.0
T_0 [K]	293
T_m [K]	933
C_v [J Kg ⁻¹ K ⁻¹]	896.3
α [K ⁻¹]	33.0×10^{-6}
l	0.75
β	0.9
Void radius a_0 [m]	5.2×10^{-9}
Void density N_v [voids/m ³]	1.0×10^{22}

Table 4.8: Material parameters for aluminum

Material	Aluminum	PVC H100
Cohesive Stress (MPa)	180	24
Fracture Energy G_c (N/m)	2.75	95.2

Table 4.9: Aluminum and PVC H100 fracture parameters

The final Young's modulus is assumed equal to about one third of the Young's modulus of the bulk PVC material from which the foam is made, to account for possible voids still present in the compacted material. The ultimate compressive strength, -50 MPa, is equal to one of the lowest values available for the compressive strength of bulk PVC [2].

In order to better characterize the PVC foam response in blast analysis, the material

behavior at high strain and high strain rates should be further investigated, since most of the experiments reported in the literature do not show the final stiffness gain. In the presented computations, the first stress peak is used as the compressive failure of the foam [59]. The strain rate does not significantly alter the first peak of the compressive stress for foam of low density, such as the Divinycell H100 (Fig. 4.25) [86, 17], however, its role in the material response at high strain is not determined and therefore not taken into account in the presented analyses.

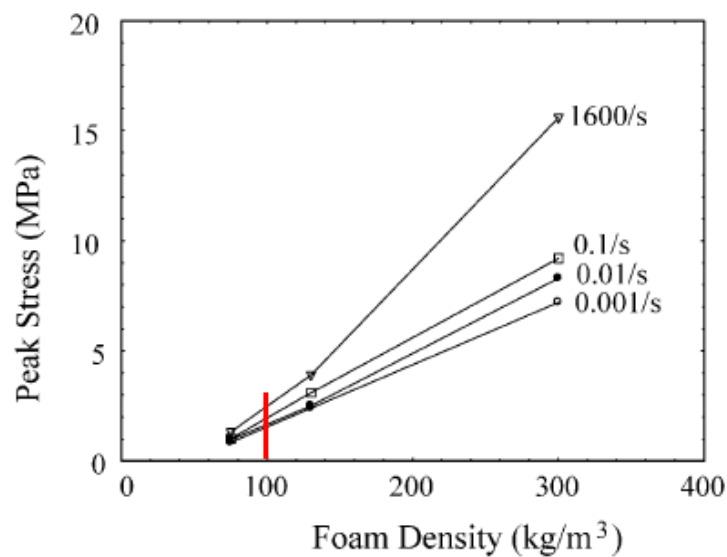
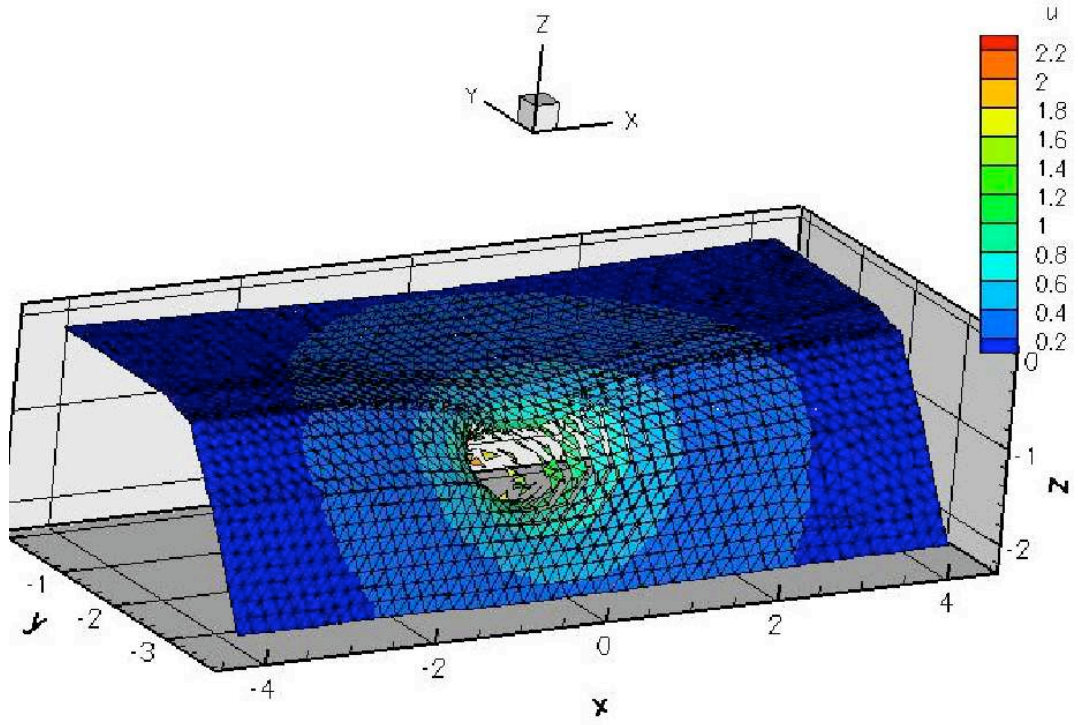
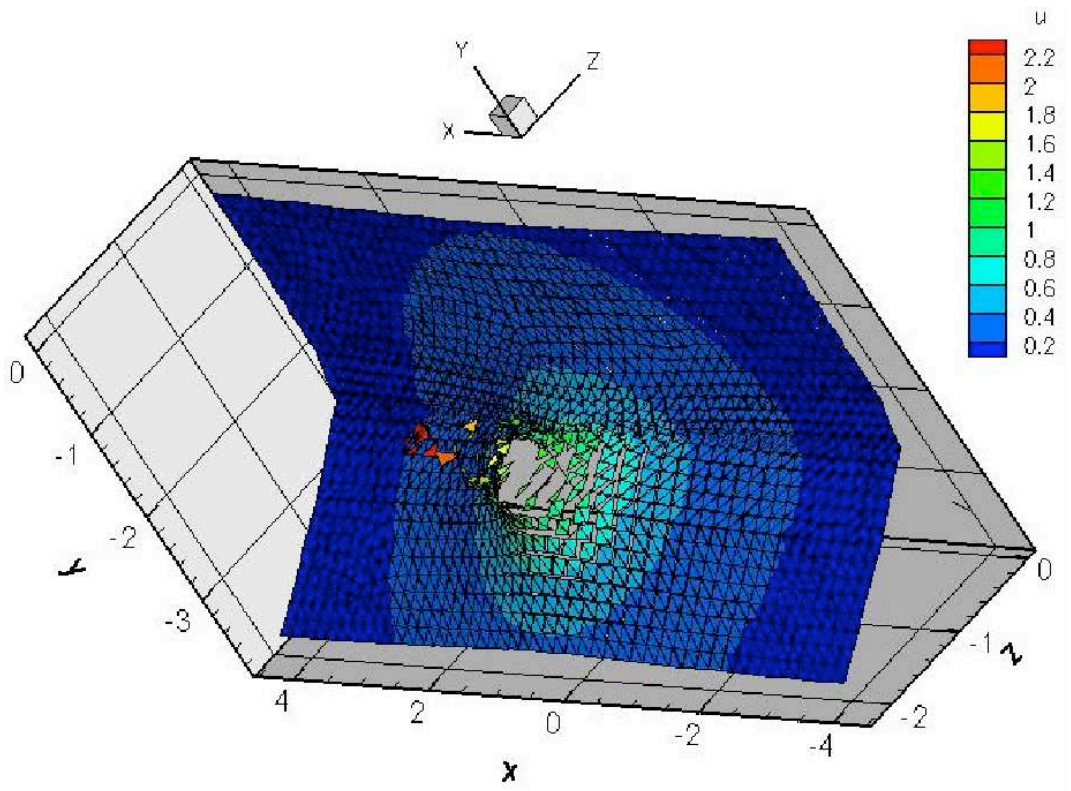


Figure 4.25: Variation of peak stress with foam density from quasi-static to high strain rate [86]

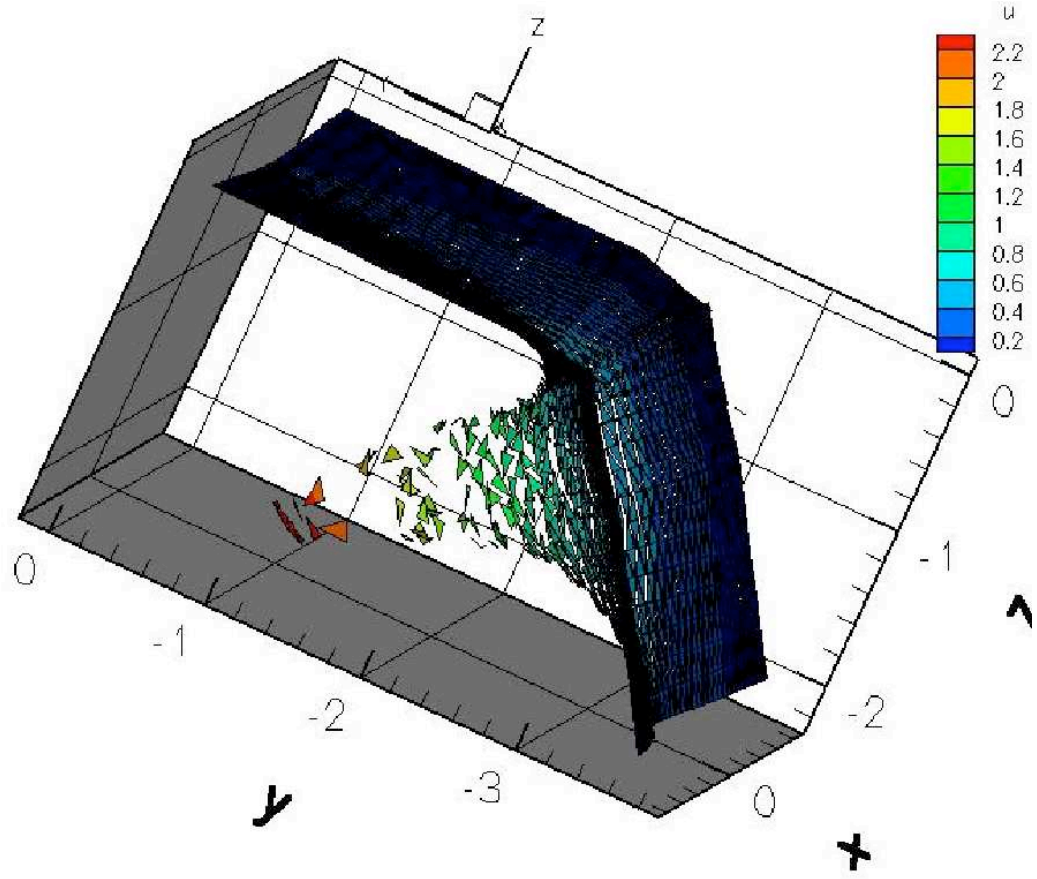
A blast load as in Section 4.3.3 was applied to an aluminum–PVC–aluminum composite hull with thicknesses 2.5, 50.0, 2.5 mm, respectively (see Fig. 4.20). The loading conditions impose bending on the structure, hence the tension/compression material properties of the PVC foam were assigned to the thickness integration points accordingly. The blast was the result of an underwater 0.5 Kg TNT explosion applied to one side of the shell in two separate simulations. The first with a shell mesh comprised of 2880 elements and the second of 11520 elements. The kinetic energy of the two shells was plotted vs. time as shown in Fig. 4.27, with a sample qualitative result shown in Fig. 4.26.



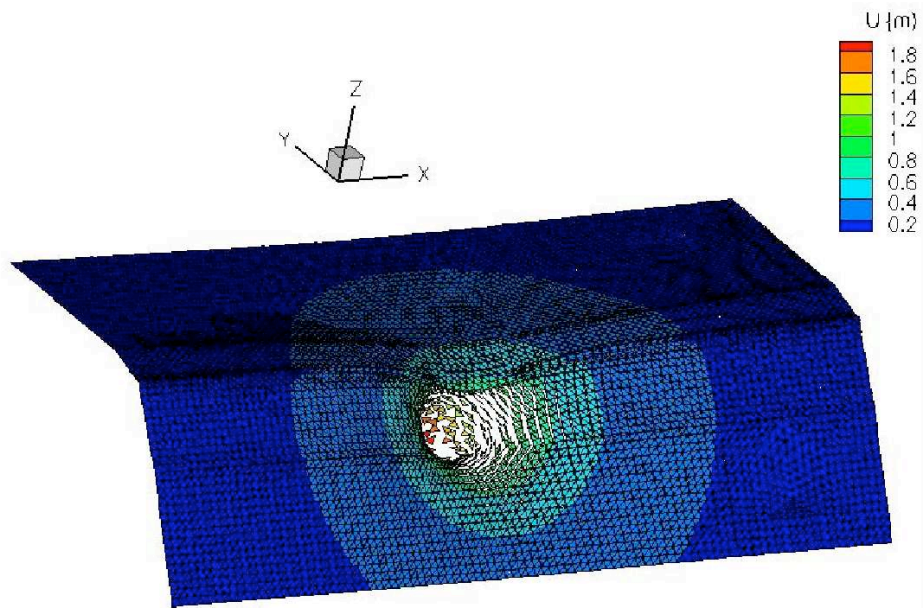
(a)



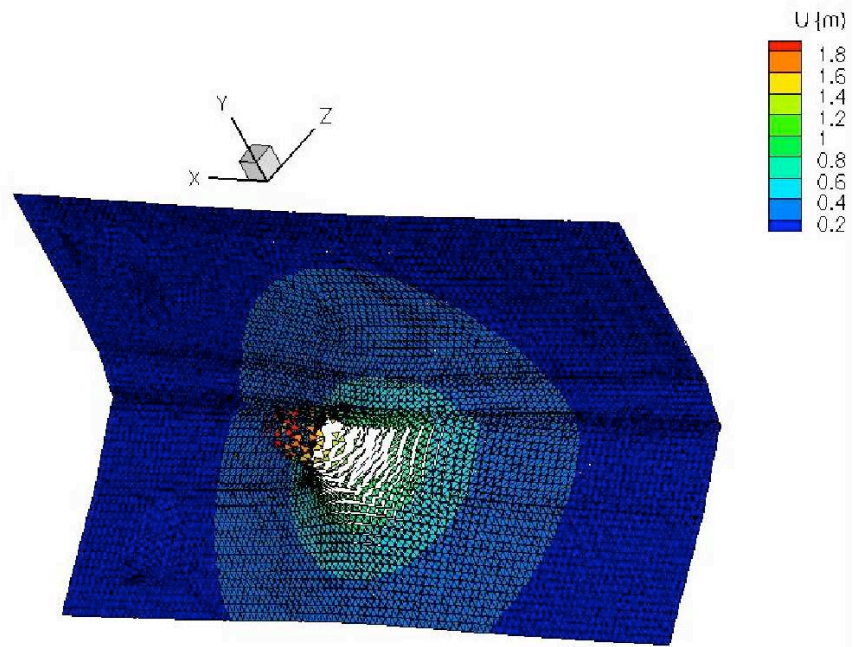
(b)



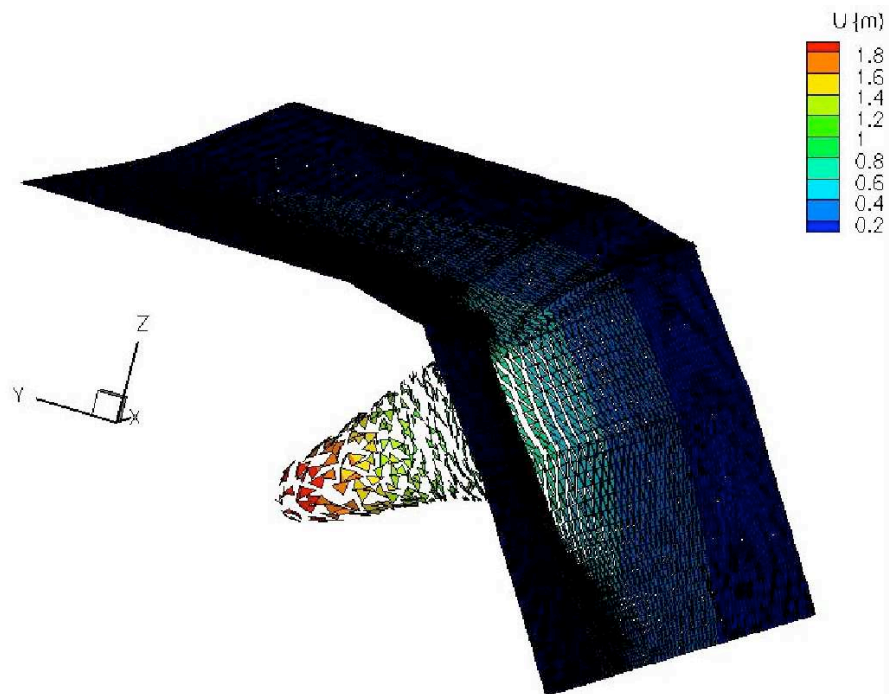
(c)



(d)



(e)



(f)

Figure 4.26: Coarse (a,b,c) and fine (d,e,f) hulls during blast impact. Views are front (a,d), back (b,e), and side (c,f).

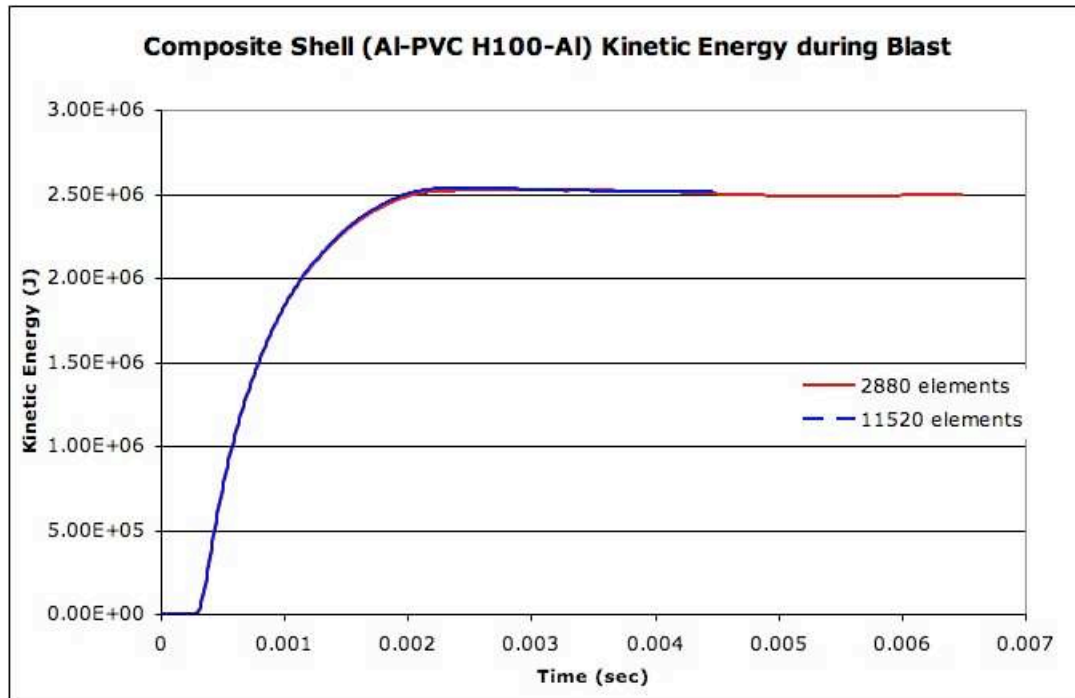


Figure 4.27: Shell kinetic energy vs. time for different configurations

All together, these methods and techniques result in a powerful framework for the modeling of a shell structure subjected to blast loading. The process of damage, fracture, and fragmentation are modeled explicitly and the energy absorbed by the structure during the blast can be precisely quantified for future design purposes.

Chapter 5

Application to brain trauma

5.1 Introduction

Brain damage resulting from traumatic brain injuries (TBI) under impact/acceleration loading is often classified as *focal* or *diffuse* in the medical literature. The first consists of contusions, lacerations, haematomas (extradural or intradural), tentorial/tonsillar herniation, etc., and may occur under (*coup*) or opposite to (*contre-coup*) the site of impact. Diffuse damage instead encompasses *diffuse axonal injury* (DAI), cerebral swelling, and cerebral ischemia, and is often associated with focal damage. Alternatively, brain damage can be classified as *primary*, occurring at the impact site, or *secondary*, occurring at remote sites.

Damage is frequently caused by the relative motion of the brain with respect to the skull (brain retarded or set into motion subsequently by the skull); striking and bouncing of the parenchyma against inner skull protrusions; rupture of bridging veins, axonal fibers and vascular tissue; and cavitation phenomena induced by negative pressures.

Fig. 5.1 (adapted from Kleiven [46]) shows the dynamics of a frontal impact injury. The translational cranial motion causes relative brain movements and short-term intracranial pressure gradients. High positive pressures are observed at the coup site, together with marked negative pressures at the contrecoup site (cf. Lindgreen and Rinder [50], Nahum et al. [63], Johnson and Young [43]). Coup contusions are produced by the slapping effect of the skull hitting the brain, while contrecoup lesions follow from the bouncing of the

brain against the inner posterior surface of the skull and the development of *cavitation bubbles* within the brain due to negative pressures. The growth and collapse of such bubbles may induce local tissue damage. This phenomenon, known as *contre cavitation*, is well recognized in the literature (cf. Lubock and Goldsmith [53], Hardy et al. [39], Nusholtz et al. [65], Brennen [14], Johnson and Young [43]).

Cavitation effects can also be observed in the coup region (*coup cavitation*), since negative pressures immediately follow the shock wave front, in both the coup and the contrecoup areas (Gross [37], Lindgreen and Rinder [50], Fujiwara [31], Rodrigues et al. [83]). Coup lesions are usually prevalent in the case of an impact from a small object, while contrecoup lesions are typically more severe under impacts from large objects. The development of coup and/or contrecoup lesions is also dependent on which part of the skull is impacted. There is evidence that frontal impacts always result in frontal lobe injuries and that occipital, and temporal impacts cause prevalent contrecoup lesions (cf. Leestma [48]). However, in many cases, both coup and contrecoup lesions are observed.

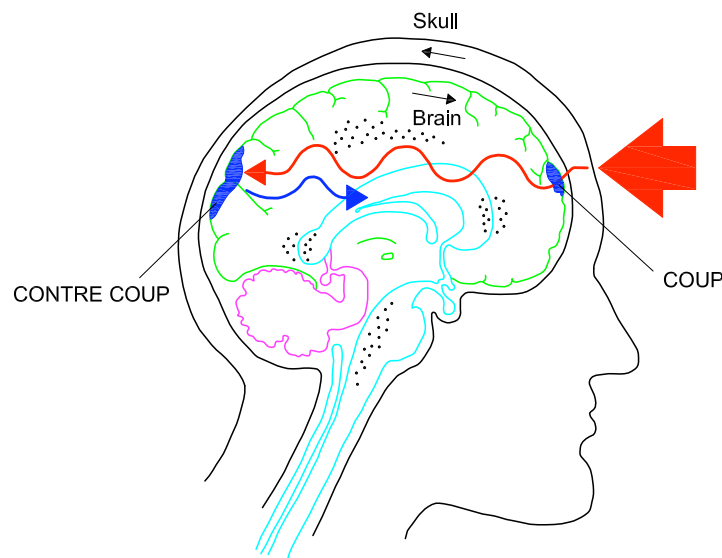


Figure 5.1: Coup-contrecoup injury (adapted from Kleiven [46])

TBI are also produced by rotational movements of the parenchyma within the skull (angular acceleration injuries) and bending-stretching of the craniospinal junction (Adams and Graham [3]). Such traumas are often associated with DAI since rotational or bending motions may lead to severe shearing of axons in different brain regions. Axons can literally be torn in half by shearing forces. DAI was defined by Strich in [88] and is now widely recognized in the literature (cf. Perles and Rewcastle [78], Adams and Graham [3]); it was observed, with varying degrees of severity, in about 30% of the cases in the Glasgow brain trauma database (Adams and Graham [3]). DAI also results in various and widespread regions of the brain no longer being able to function or intercommunicate. Gliar cellular reactions create axonal retraction balls and/or microglial scars or degeneration of the fiber tracts.

Moreover, blast-associated TBI represents another relevant form of brain damage, which is receiving a growing attention from the scientific community due to its special features and relevance for civil and military purposes.

Biomechanical modeling of traumatic brain injuries requires the formulation of complex constitutive equations, accounting for large strains, time and rate effects, and consistent damage modeling. The current biomechanical literature is mainly concerned with hyperelastic or finite linear viscoelastic models, accounting for small perturbations away from thermodynamic equilibrium (Prangue and Margulies [79], Miller et al. [56], [57], [58], Meaney [54], Brands et al. [11], [12], Velardi et al. [91]). Plasticity, hysteresis, permanent deformation, and biphasic (solid/fluid) behavior of soft biological tissues have also been analyzed by Bergström and Boyce [9], Gasser and Holzapfel [32], and Franceschini et al. [30]. It is often assumed that brain *white matter* exhibits mechanical *anisotropy*, due to the presence of oriented neural tracts (*axons*) in a matrix made of cell bodies and vascular network (cf. [79], Meaney [54], Velardi et al. [91]). The latter, on the contrary, doesn't possess any particular directionality and can be modeled as isotropic (*gray matter*). Nevertheless, some authors assume that brain tissue (both in the gray and in the white matter) may be modeled as *initially isotropic*, provided that a large enough sample of material

is taken into consideration (cf. Miller et al. [57], [58]).

This chapter deals with the biomechanical modeling of the brain tissue response to traveling impact waves, and the computational simulation of traumatic brain injuries. The material model presented in this thesis is employed. By contrast to other elastic and viscoelastic approaches available in the literature, the present model is able to reproduce permanent brain tissue damage, in the form of plastic sliding between brain layers and irreversible growth of voids or bubbles in the material, simulating the effects of DAI and cavitation injury. The model also includes time-dependent viscous deformations and large perturbations of the material from thermodynamic equilibrium, via an exact finite viscoelasticity theory with validation against available experimental results on brain tissue samples in Chapter 3.

Finite element simulations of two different traumatic brain injuries are presented, examining frontal and oblique impact events. The ability of the present theory in reproducing real tissue damage mechanisms is illustrated, and predictions of intracranial pressure, shear strain, cavitation, and shear injuries dynamics are presented. Attention is focused on the correlation between simulation results and prediction of physiological brain dysfunction. Potential applications of the present research to relevant medical and engineering problems are examined in the closing chapter.

5.2 Finite element model of the human head

The injury simulations presented in this work make use of a finite element model of the human head recently realized at the Bioengineering Laboratory of the University of Salerno [16]. A finite element mesh was reconstructed from the axial Magnetic Resonance Images available in "The Whole Brain Atlas" of the Harvard Medical School (<http://www.med.harvard.edu/AANLIB/>), via 3D image processing and editing, using the commercial software Mimics (Materialise Group, Leuven, Belgium). The mesh includes the following components (refer to Fig. 5.2): (1) skull without facial bones; (2) cerebrospinal fluid (CSF) in the form of a 3-mm-thick layer; (3) gray matter; (4) white matter; (5) cerebellum; (6) corpus

callosum; (7) telencephalic nuclei; (8) brain stem; (9) ventricles.

The entire model comprises 39047 tetrahedral composite elements [89], and is characterized by a detail level similar to that of the Wayne State Brain Injury Model (Zhou et al. [102]). The brain measures 1508 cm³ in volume (CSF excluded) and has a mass of 1.40 kg. The modeled portion of the skull is 678 cm³ in volume and has a mass of 0.82 kg. The total model mass is 2.38 kg. The reader is referred to Cardamone and Socci [16] for further details about mesh geometry, density, and topology.

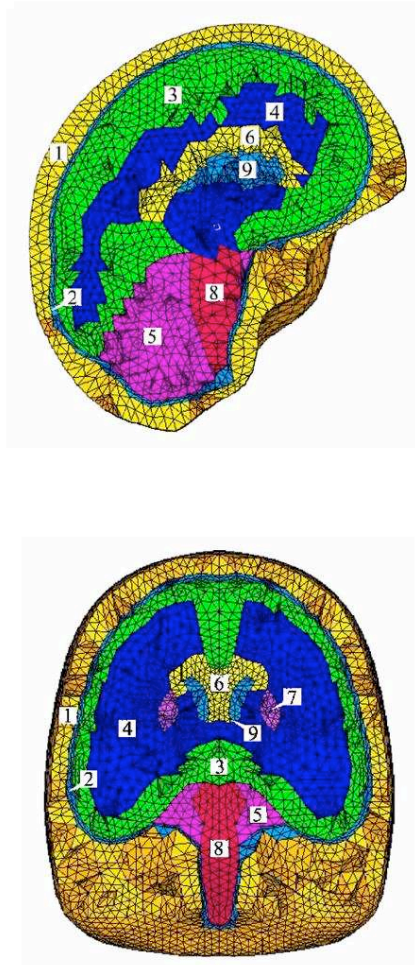


Figure 5.2: Mid-sagittal and mid-coronal sections of the adopted head finite element model: (1) skull without facial bones; (2) CSF; (3) gray matter; (4) white matter; (5) cerebellum; (6) corpus callosum; (7) telencephalic nuclei; (8) brain stem; (9) ventricles.

The constitutive model presented in this work is used to model the brain tissue components, considering two viscoelastic mechanisms and one-term Ogden functions. Viscoelastic material properties frequently used in the literature for head injury simulations (cf. Zhou et al. [102]; Zhang et al. [100], [101]; Kleiven [46]; Kleiven and von Holst [47]; Horgan and Gilchrist [42]) were suitably adapted to the present model. A factor of $1/2.5$ is used to rescale the short-term shear moduli given in [101] for white matter, gray matter, and brain

stem, to ensure consistency with the short-term brain tissue model proposed by Mendis et al. [55]. In particular, shear stiffness ratios of $1/2$, $1/4$, $1/4$ are assigned to the elastoplastic and the viscoelastic networks, respectively. Following the results given in [27], negative $\{\mu, \alpha\}$ couples are considered. A yield stress of 20 kPa is adopted, amplifying by a factor of 2 the shear stress threshold defined by Zhang et al. [101] as a tolerable level for 80% probability of mild traumatic brain injury. The volumetric viscosities η_i^{vol} were set to zero, assuming purely elastic volumetric behavior in the viscoelastic networks. The shear (or deviatoric) viscosities $\eta_{i,n}^{dev}$ were expressed in terms of the (near thermodynamic equilibrium) *relaxation times* $\tau_i = \eta_i^{dev} / \mu_i$, where η_i^{dev} and μ_i are consistent linear viscosities and shear moduli. In detail, $\tau_1 = 0.008s$ is prescribed in the first, and $\tau_2 = 0.15s$ in the second mechanism [55]. The first mechanism accounts for short-term viscoelastic response and essentially rules time effects in impact problems (cf. next section). The complete set of material properties employed for soft tissue components is given in Tab. 5.1. For the skull and the CSF, the hyperelastic models described in Tab. 5.2 (cf. [100]) are adopted.

Component	GM	WM	BSCC
Mass density [kg/m ³]	1040	1040	1040
<i>Elastoplastic response</i>			
Ogden's coefficient μ_1 [kPa]	-2.72	-3.28	-4.64
Ogden's coefficient α_1	-5.00	-5.00	-5.00
Long term shear mod. μ^∞ [kPa]	6.80	8.20	11.60
Bulk modulus κ [kPa]	2190	2190	2190
Yield stress σ_0 [kPa]	20.0	20.0	20.0
Reference plastic strain ϵ_0^p	0.05	0.05	0.05
Hardening exponent n	10	10	10
Reference plastic strain rate $\dot{\epsilon}_0^p$ [s ⁻¹]	0.001	0.001	0.001
Plastic strain rate exponent m	10	10	10
Void density N_v [m ⁻³]	10 ⁸	10 ⁸	10 ⁸
Initial void radius a_0 [μ m]	100	100	100
<i>First viscoelastic mechanism</i>			
Relaxation time τ_1 [s]	0.008	0.008	0.008
Ogden's coefficient $\mu_{1,1}$ [kPa]	-1.36	-1.64	-2.32
Ogden's coefficient $\alpha_{1,1}$	-5.00	-5.00	-5.00
Bulk modulus κ_1 [kPa]	2190	2190	2190
<i>Second viscoelastic mechanism</i>			
Relaxation time τ_2 [s]	0.15	0.15	0.15
Ogden's coefficient $\mu_{2,1}$ [kPa]	-1.36	-1.64	-2.32
Ogden's coefficient $\alpha_{2,1}$	-5.00	-5.00	-5.00
Bulk modulus κ_2 [kPa]	2190	2190	2190
Initial shear modulus μ^0 [kPa]	13.60	16.40	23.20

Table 5.1: Soft tissue material properties. GM = Gray Matter; WM = White Matter; BSCC = Brain Stem and Corpus Callosum

	Skull	CSF
Mass density [kg/m^3]	1210	1004
Shear modulus μ [kPa]	3280	0.50
Bulk modulus κ [kPa]	4760	2190

Table 5.2: Skull and CSF properties

5.3 Impact simulations

The present section illustrates two different head injury simulations concerning frontal and oblique impacts with an external object. In the first case, some comparisons are established with available experimental results. Attention is focused on intracranial pressures, shear stresses, and related brain tissue damage.

5.3.1 Frontal impact

A simulation of experiment no. 37 by Nahum et al. [63] on the intracranial pressure dynamics in a human cadaver impacted by a rigid mass is performed. The impact was reproduced by applying a pressure load history over a frontal region of the skull, with semi-sinusoidal time distribution for a duration of 6 ms and amplitude corresponding to a resultant peak force of 7.90 kN [63] (Figs. 5.3, 5.4). Similar simulations have been performed by other authors for the validation of different finite element models (cf. Ruan et al. [85], Zhou et al. [102], Kleiven and von Holst [47], Horgan and Gilchrist [42]).

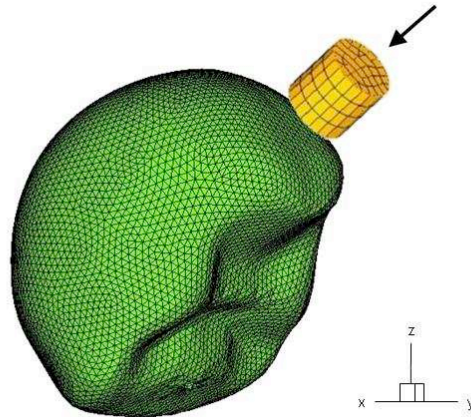


Figure 5.3: Frontal impact injury

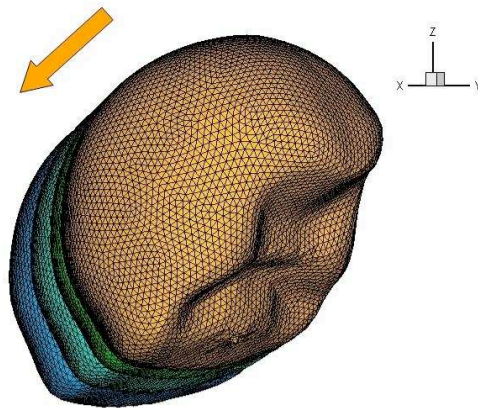


Figure 5.4: Animation of the translational head motion following frontal impact ($t = 2, 4, 6, 8$ ms)

Fig. 5.5 shows the predicted pressure time-histories in correspondence with three different brain regions (frontal, posterior-fossa and parietal lobes), against the corresponding experimental results given in [63]. A very good correlation between theory and experiments can be observed, concerning both peak values and time-distribution of the intracranial pressure, which validates the present constitutive and finite element models.

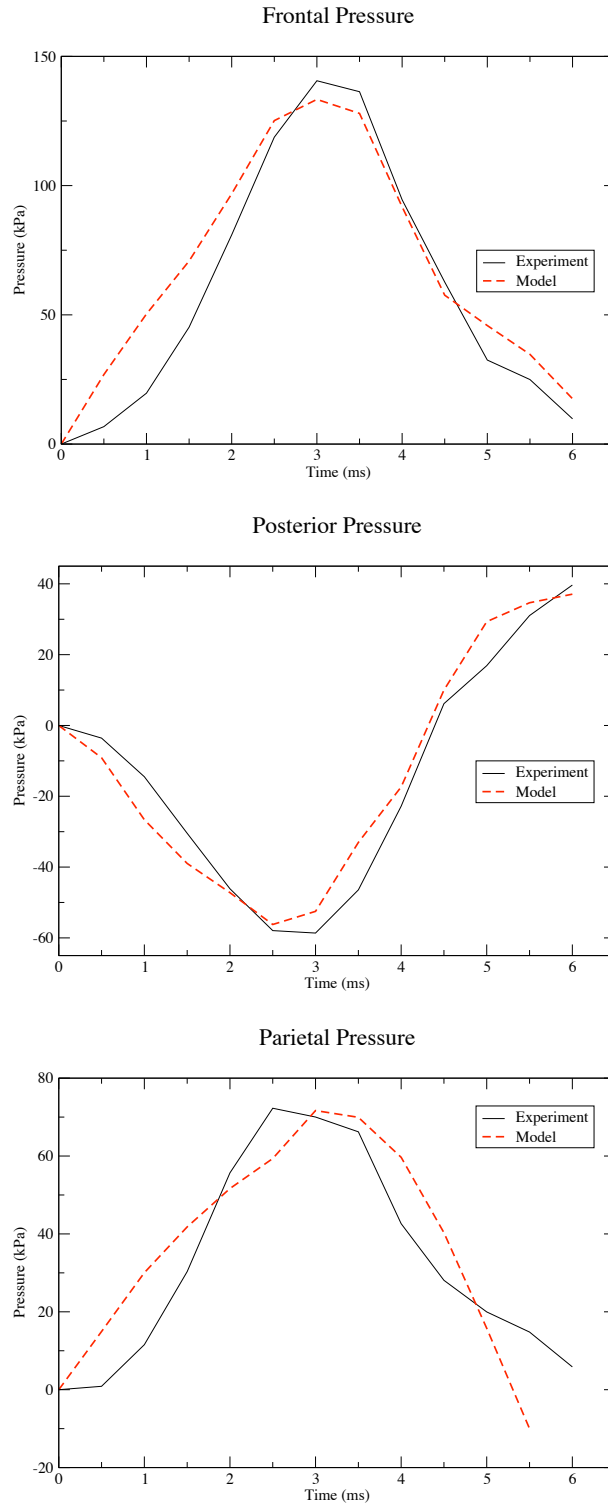
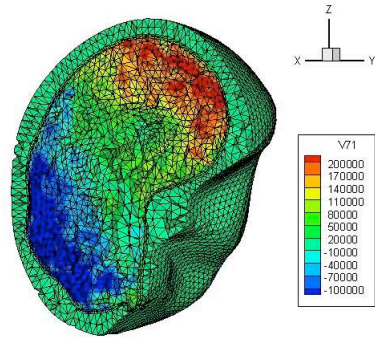


Figure 5.5: Predicted vs. experimental intracranial pressure time-histories (Nahum et al. [63], experiment no. 37)

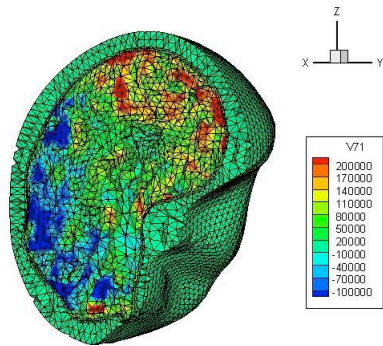
During the simulation, as well as in the referenced experiment [63], positive (compressive) peak pressures were observed in the frontal brain region, beneath the impact site, together with negative (tensile) pressure in the posterior-fossa area, opposite to the impact site (Fig. 5.5). Those peaks approximately occurred in correspondence with the peak of the external pulse ($t = 3$ ms). After that time, the frontal pressure started to decrease toward zero, while the posterior pressure began to increase toward positive values. A pressure profile similar in shape to that of the frontal region, but reduced in amplitude, was observed in correspondence with the parietal lobe (Fig. 5.5).

Contour plots of the intracranial pressure over a mid-sagittal section of the head model are shown in Fig. 5.6, at the peak ($t = 3$ ms), during the decreasing phase ($t = 4.5$ ms), and soon after the end of the pulse ($t = 6.5$ ms). One observes that the traveling stress wave reflects against the skull at the contre-coup site and then moves back toward the interior of the parenchyma. It is followed by a *tensile "tail"* (negative pressure wave), which produces irreversible cavitation damage in different brain regions, especially within the contre-coup area (Fig. 5.7). Cavitation initiates when the traveling tensile stress reaches a threshold value p_c (*critical cavitation pressure*) [94], [27], and determines instable growth of voids (or bubbles) in the tissue. It is locally amplified by the superposition of primary and reflected tensile waves.

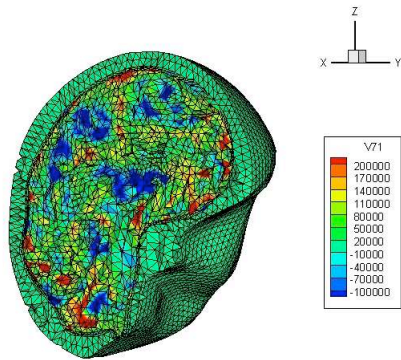
101



t=3.0 ms

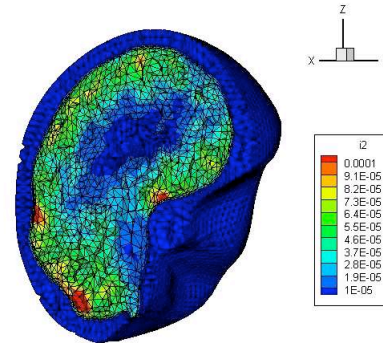


t=4.0 ms

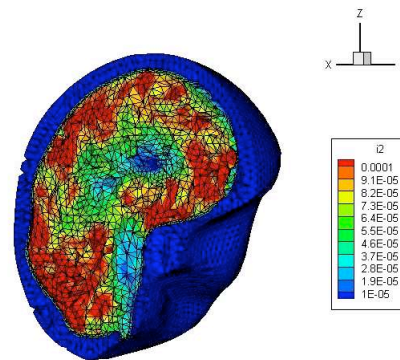


t=6.5 ms

Figure 5.6: Frontal impact: intracranial pressure contours (Pa)



t=4.5 ms



t=6.5 ms

Figure 5.7: Frontal impact: cavitation damage predictions

The dynamics of the shear deformation are slightly different. Fig. 5.8 shows contour plots at different times of the total effective shear stress τ . It continues to rise also after the peak of the pulse, assuming extreme values in correspondence with the parietal lobe, the corpus callosum, the thalamus, and the midbrain (cf. [100], [101], [42]). Its highest value, however, remains below the adopted plastic threshold ($\tau \leq \sigma_0 = 20$ kPa, cf. Fig. 5.8), and hence no permanent shear damage occurs in the present case. Nevertheless, remarkable elastic and viscous shear deformations arise in different brain regions. Contour plots of the viscous shear strain ϵ^v in the first viscoelastic mechanism are depicted in Fig. 5.9. In the current example, ϵ^v can be regarded as measure of transient (axonal) shearing damage of

brain tissue. It will be released after the end of the pulse, in a time sufficiently larger than the mechanism relaxation time ($t \gg 8$ ms, cf. Tab. 5.2).

104

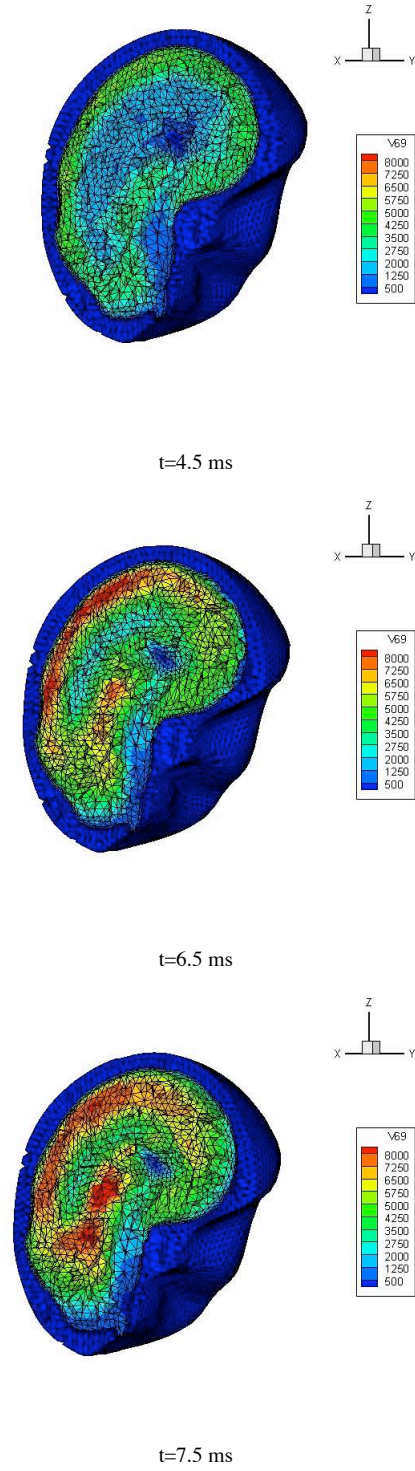


Figure 5.8: Frontal impact: shear stress contours (Pa)

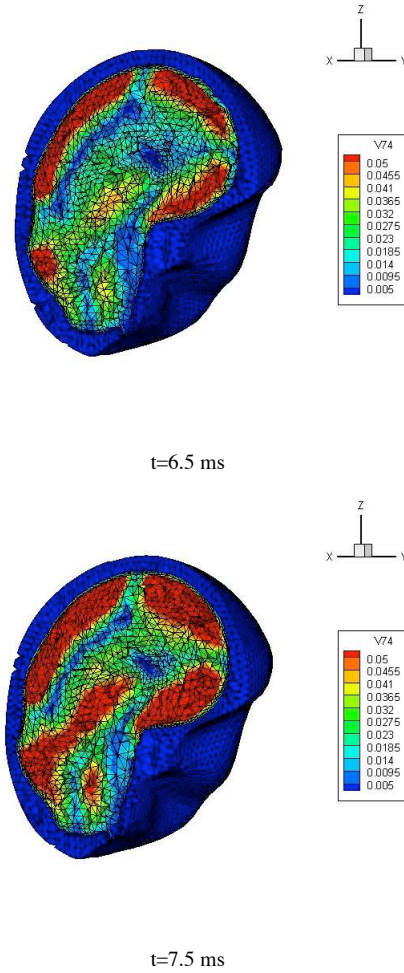


Figure 5.9: Frontal impact: viscous shear deformation predictions

5.3.2 Oblique impact

An oblique impact event was simulated by applying the same pulse of the previous example on a lateral region of the frontal bone, in such a way to induce a mixed translational-rotational motion of the head (Figs. 5.10, 5.11).

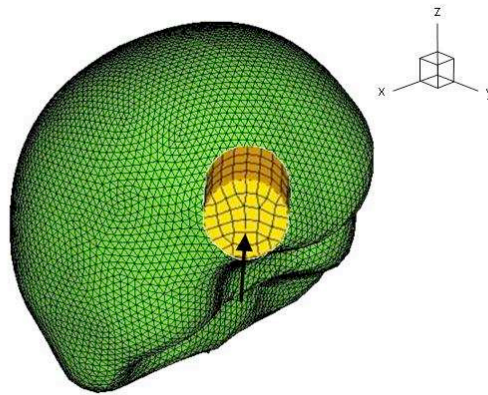


Figure 5.10: Oblique impact injury

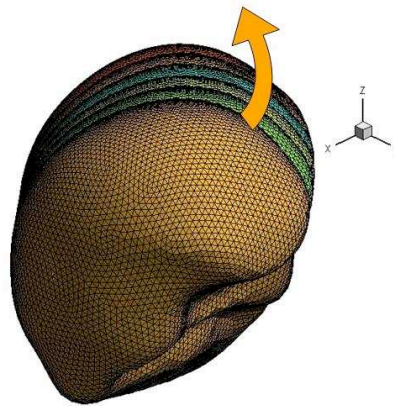
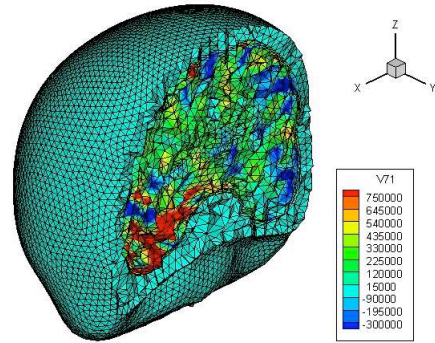
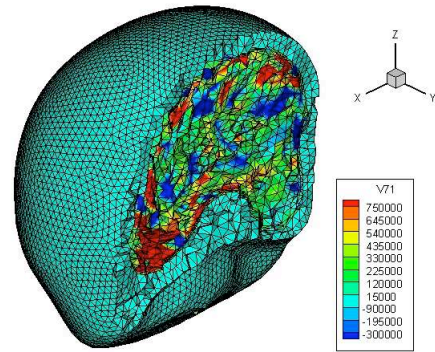


Figure 5.11: Animation of the translational-rotational head motion following oblique impact ($t = 2, 4, 5, 6, 7, 8$ ms)

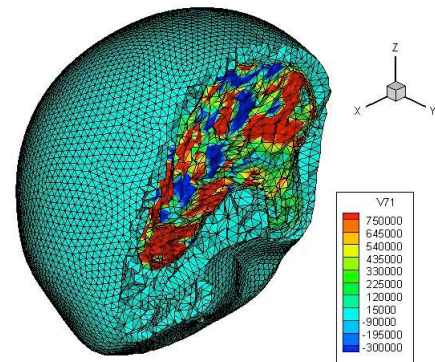
This new simulation leads to the intracranial pressure profiles depicted in Fig. 5.12 over a plane parallel to the impact direction through the center of the impact zone. It is seen that markedly higher positive and negative pressures develop in the present case within the coup and contre-coup regions, as compared to frontal impact. Such high intracranial pressures induce intense and diffused cavitation damage (Fig. 5.13), with peaks of θ^p markedly higher than those observed in the previous example (cf. Fig. 5.7).



$t=3.0$ ms

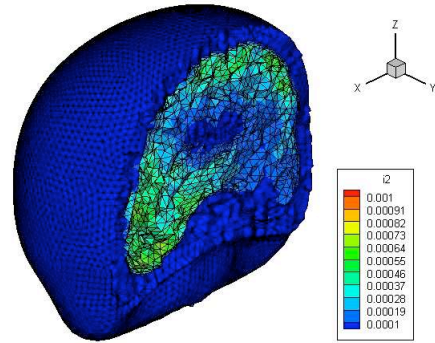


$t=4.0$ ms

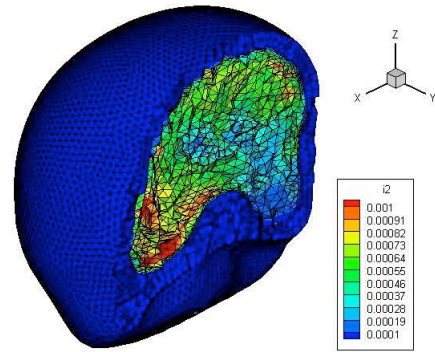


$t=5.0$ ms

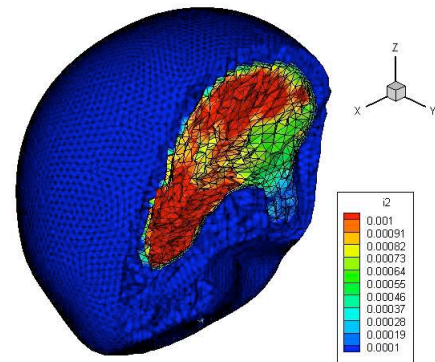
Figure 5.12: Oblique impact: intracranial pressure contours (Pa)



$t=3.0$ ms



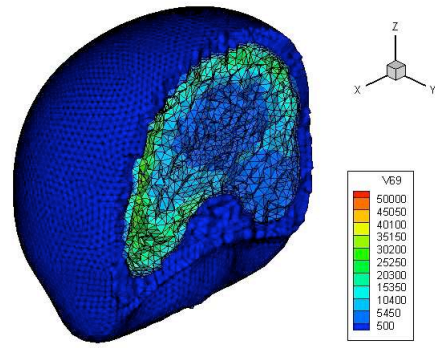
$t=4.0$ ms



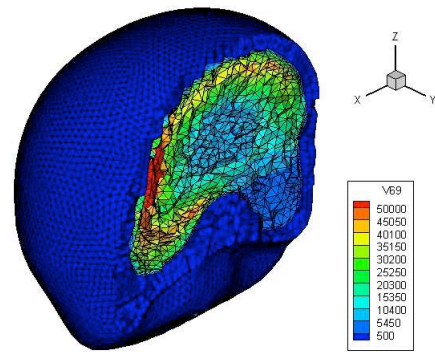
$t=5.0$ ms

Figure 5.13: Oblique impact: cavitation damage predictions

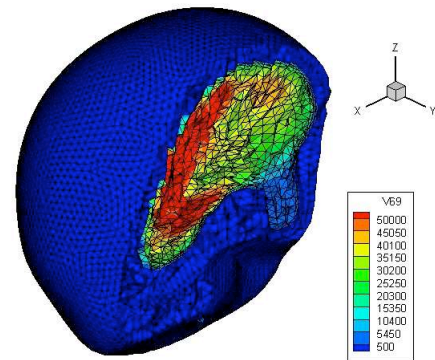
Concerning the shear stress τ , the time history represented in Fig. 5.14 is recorded. It can be noticed that τ profiles follow the contours of the velocity gradient associated with the rotational motion of the head (Fig. 5.11). Its peaks initially appear beneath the cortical surface, and then evolve toward the core regions of the brain (cf. [101]). They are up to 10 times higher than those predicted for frontal impact, which implies the attainment of the yield limit in the elastoplastic network and the development of permanent shear damage ϵ^p , as shown in Fig. 5.15. Therefore, occurrence of DAI can be predicted, evolving from the periphery to the core of the brain. Marked viscous shear deformation ϵ^v in the first viscoelastic mechanism is also observed, with analogous time-space distribution as compared to ϵ^p (Fig. 5.16). In the present case, the difference $\epsilon^v - \epsilon^p$ may be regarded as a measure of transient axonal shearing.



$t=3.0$ ms

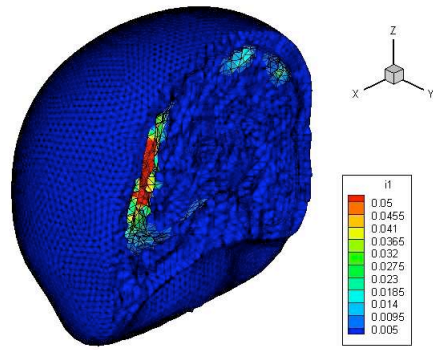


$t=4.0$ ms

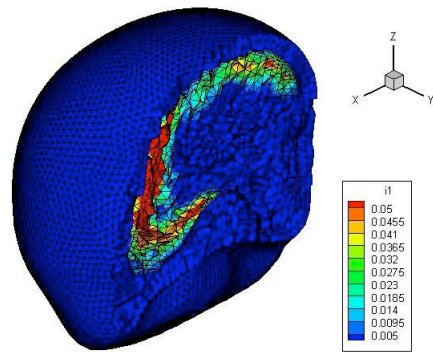


$t=5.0$ ms

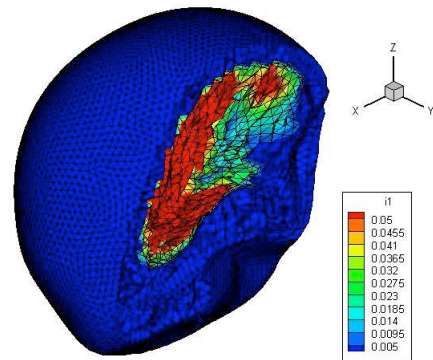
Figure 5.14: Oblique impact: shear stress contours (Pa)



$t=3.5$ ms

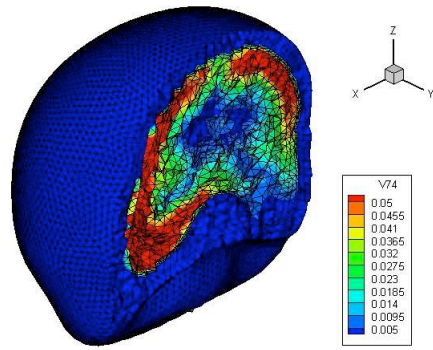


$t=4.0$ ms

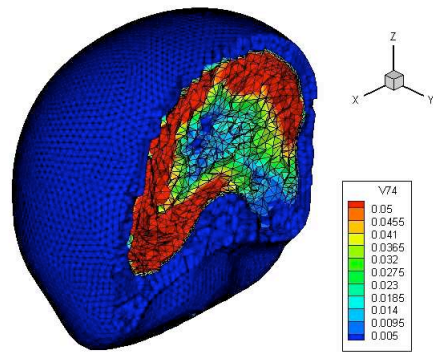


$t=5.0$ ms

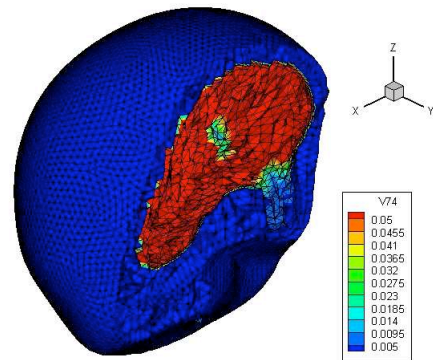
Figure 5.15: Oblique impact: permanent shear damage predictions



$t=3.5$ ms



$t=4.0$ ms



$t=5.0$ ms

Figure 5.16: Oblique impact: viscous shear deformation predictions

Chapter 6

Conclusions

6.1 Summary

The presented soft material constitutive model is able to reproduce the behavior of a wide range of soft materials. The model combines finite viscoelasticity, finite elastoplasticity, and decoupling of volumetric and deviatoric responses. The viscoelastic response is described through Ogden-type models including volumetric deformation. Volumetric plasticity is related to the expansion of voids or bubbles in the material, as physically observed in many polymers and soft biological tissues undergoing crazing, cavitation, or both.

The large number of material parameters required by the model demanded a systematic approach for their identification. An optimization procedure based on Genetic Algorithms is formulated and its versatility is demonstrated via the identification of parameters for polyurea, high-density polyethylene, and brain tissue.

An application to ballistic impact on a polyurea-retrofitted composite plate is simulated and validated, and computational capability for assessing the blast performance of metal/elastomer composite shells is also shown. Clinically relevant injuries, such as DAI and cavitation injury, are shown to be related to specific mechanical damage modes of brain tissue involving plastic and/or viscous deformations. Finite element simulations effectively predict the distribution, intensity, and reversibility/irreversibility of tissue damage, as well as the associated physiological brain dysfunction.

6.2 Outlook

This work is primed for use in relevant engineering and biomechanical applications such as design assessment and optimization of a variety of structures under dynamic loading (e.g., polyurea-reinforced plates and shells), and simulation of impact-induced damage in biological tissues. Future directions of this work may lead to the formulation of head-injury criteria for medical, governmental, and industrial applications; addressing the definition of clinical-biomechanical injury thresholds and tolerances; the simulation of a wide range of injuries, including blast-induced TBI and the effects of growing tumors; neurosurgical simulations; and the design and the assessment of effective protective devices, such as helmets including honeycomb materials, polymers, or foam padding.

6.2.1 Polymeric applications

There is a wide range of uses for computational modeling of soft materials such as polymers and biological tissues. The computational utility is unsurpassed in the way that modeling provides clear perception into the behaviors of polymers under a variety of circumstances that are experimentally problematic. Computational modeling has become a vital instrument in research determining the properties of polymers. With the onset of quicker computer processors, many simulations can be made in an very short amount of time. In addition, studies have shown the power of computational modeling in predicting polymer properties, especially at interfaces and in solution. Thus, computational modeling of polymers can provide a valuable tool to supplement the ongoing research on the interface between phase-separated domains. A specific area of investigation would be using computer simulations to model failure at an interface; an important goal would be to use the simulations to isolate signatures for a specific failure mode. These studies would be particularly helpful in designing high-strength composites.

6.2.2 Medical applications

Ever since the increase in popularity of computational modeling, there have been many contributions to the understanding of human health in regards to disease, injury, and their treatment. Moreover, simulation of soft tissues is an increasingly practical instrument in predicting surgical outcomes and in the training of medics/doctors. The possible uses of computational modeling include laproscopic surgery, craniofacial reconstruction, z-plasty, breast reduction, gastrointestinal surgery, and reconfiguration of musculoskeletal geometry. In these and many other scenarios, a subject-specific simulation environment in which procedures can be practiced is of immeasurable value for the development of surgical techniques. In retrospect, the lack of status given to computational modeling limits the applicability of surgical simulation. The solutions to these problems require collaboration between mathematicians, computer scientists, engineers, and clinicians. Through computational modeling, one visits the most promising directions for algorithm design, use of architectures, surgical simulation interface design, and procedures that lend themselves to simulation by encouraging interdisciplinary cooperation between medicine, engineering, applied math, and computer science. Nonetheless, the modeling of soft materials such as biological tissues has yet to reach its full potential as a contributor to the improvement of the health-care industry. Because of the inherent complexities of the microstructure and biomechanical behavior of biological cells and tissues, there is a need for new hypothetical frameworks to guide the design and interpretation of new classes of experiments. Because of continued advances in experimental technology, and the associated rapid increase in information on molecular and cellular contributions to behavior at tissue and organ levels, there is a high demand for mathematical models to quantify and predict observations across multiple length- and time-scales. Due to the intricate geometries and loading conditions, there is a demand for computational approaches to solve the boundary and initial-value problems of clinical, industrial, and academic applications. Inasmuch, computational modeling of cancer behavior may be useful in the future for predicting tumor growth and guiding treatment options. The modeling can be thought of as slicing a tumor. Mathematical

equations are used to create a computer simulation of tumor growth, allowing physicians to ascertain if the cancer will develop invasive and metastatic qualities.

Moreover, sophisticated musculoskeletal computational models help researchers to better comprehend the loads applied to natural joints under normal and abnormal conditions. When the researchers brought these models to the forefront, they were able to design more effective artificial joints. In academia, researchers use biomechanical and statistical models to create artificial limbs that are designed to function in a diverse set of situations: in patients ranging from frail to heavy-set, and for activities from sitting down to climbing stairs. Many researchers also generate computational models that include variables that surgeons and implant designers can administer (such as implant materials and geometric design), as well as environmental variables beyond their control (including but not limited to patients' varying activity levels and individual bone strength). Continuing work on computational modeling has led to many breakthroughs in statistical optimization methods that consider factors which optimize the design of an implant. This perspective of computational modeling allows researchers to decipher what components are useful, conserving funds and helping to decide where to concentrate efforts and resources.

6.2.3 Neuromuscular applications

Neuroprosthesis has made one of the biggest leaps in computational biomechanics. For the past three decades, clinicians have performed experiments using electrodes to stimulate paralyzed muscles in coordinated patterns. Their work has led to the creation of implanted functional electrical stimulation (FES) systems that allow partially paralyzed patients to hold a fork and feed themselves, brush their teeth, or run a comb through their hair. Over time, biomechanical models have come to play a greater role in FES systems. Basically, as the functions that we would like to restore have become more and more complex, our ability to implement them by intuition and trial-and-error is decreasing. For this reason computational models are needed in the field of neuromuscular science.

6.3 A concluding remark

The principal message is simply that much has been learned through computational modeling. Less than a half a century old, continuum computational modeling of soft materials is undoubtedly still in its infancy and its projected outlook remains promising for improving humanity's quality of life. Continued advances in computers and computational methods are increasing our ability to handle large amounts of data and to model complex initial boundary value problems; and continued improvements in diagnostics are allowing disease and injury to be treated earlier.

Modeling of soft materials has a vital role to play in the development of the needed mathematical models and analyses. Because of the incredible complexity of the biochemical aspects of soft tissues and the chemophysical aspects of polymers, this type of modeling cannot develop in isolation. There is a need for increased interdisciplinary and multidisciplinary research that brings scientists from various fields together in teams, both in research and education. Only in this way can we achieve our ultimate goal: to improve the human condition through knowledge of continuum modeling of soft materials.

Bibliography

- [1] *Technical data from DIAB*, March 2007.
- [2] *Technical data from PLASTICUSA*, July 2007.
- [3] J. H. Adams and D. I. Graham. Diffuse brain damages in non-missile head injury. In *Recent Advances in Histopathology*. Churchill Livingstone, Edinburgh, 1984.
- [4] A. Addiego, A. Dahoun, C. G'Sell, and J. M. Hiver. Characterization of volume strain at large deformation under uniaxial tension in high-density polyethylene. *Polymer*, 47:4387–4399, 2006.
- [5] A. V. Amirkhizi, J. Isaacs, J. McGee, and S. Nemat-Nasser. An experimentally-based viscoelastic constitutive model for polyurea, including pressure and temperature effects. *Philos. Mag. and Philos. Mag. Lett.*, 86:5847–5866, 2006.
- [6] J. M. Ball. Convexity conditions and existence theorems in nonlinear elasticity. *Arch. Ration. Mech. An.*, 63:337–403, 1977.
- [7] G. A. Banyay. Examination of polymeric foam as an on-board vehicular hpr hydrogen storage media. Master's thesis, Russ College of Engineering and Technology of Ohio University, 2006.
- [8] J. S. Bergström and M. C. Boyce. Constitutive modeling of large strain time-dependent behavior of elastomers. *J. Mech. Phys. Solids*, 46:931–954, 1998.

- [9] J. S. Bergström and M. C. Boyce. Constitutive modeling of the time-dependent and cyclic loading of elastomers and application to soft biological tissues. *Mech. Mater.*, 33:523–530, 2001.
- [10] D. W. A. Brand, G. W. M. Peters, and P. H. M. Bovendeerd. Design and numerical implementation of a 3-d non-linear viscoelastic constitutive model for brain tissue during impact. *J. Biomech.*, 37:127–134, 2004.
- [11] D. W. A. Brands, P. H. M. Bovendeerd, and J. S. H. M. Wisman. On the potential importance of non-linear viscoelastic material modelling for numerical prediction of brain tissue response: test and application. *Stapp Car Crash Journal*, 46:103–121, 2002.
- [12] D. W. A. Brands, G. W. M. Peters, and P. H. M. Bovendeerd. Design and numerical implementation of a 3-d non-linear viscoelastic constitutive model for brain tissue during impact. *J. Biomech.*, 37:127–134, 2004.
- [13] K. Branner. *Capacity and Lifetime of Foam Core Sandwich Structures*. PhD thesis, Department of Naval Architecture and Offshore Engineering, Technical University of Denmark, 1995.
- [14] C. E. Brennen. Cavitation in biological and bioengineering contexts. In *5th International Symposium on Cavitation*, Osaka, Japan, 2003.
- [15] G. T. Camacho and M. Ortiz. Computational modelling of impact damage in brittle materials. *Int. J. Solids Struct.*, 33(20–22):2899–2938, 1996.
- [16] L. Cardamone and D. Socci. Modellazione morfo-strutturale dell'estremo cefalico ed analisi numerica del trauma cranico da impatto. Technical report, Bioengineering Laboratory, University of Salerno, Italy, 2005.

- [17] U. Chakravarty, H. Mahfuz, M. Saha, and S. Jeelani. Strain rate effects on sandwich core materials: an experimental and analytical investigation. *Acta Materialia*, 51:1469–1479, 2003.
- [18] P. G. Ciarlet. *Three-dimensional Elasticity*. Elsevier, Amsterdam, 1988.
- [19] F. Cirak and M. Ortiz. Fully c^1 -conforming subdivision elements for finite deformation thin-shell analysis. *Int. J. Numer. Meth. Eng.*, 51:813–833, 2001.
- [20] F. Cirak, M. Ortiz, and A. Pandolfi. A cohesive approach to thin-shell fracture and fragmentation. *Comput. Method. Appl. M.*, 194:2604–2618, 2005.
- [21] F. Cirak, M. Ortiz, and P. Schröder. Subdivision surfaces: A new paradigm in thin-shell finite-element analysis. *Int. J. Numer. Meth. Eng.*, 47(12):2039–2072, 2000.
- [22] R. J. Clifton (presenter), T. Jiao, and S. Grunsel. Deformation and failure of an elastomer at very high strain rates. *15th U.S. National Conference on Theoretical and Applied Mechanics*, 2006.
- [23] M. Colakoglu, O. Soykasap, and T. Özek. Experimental and numerical investigations on the ballistic performance of polymer matrix composites used in armor design. *Appl. Compos. Mater.*, 14:47–58, 2007.
- [24] A. Cuitino and M. Ortiz. A material-independent method for extending stress update algorithms from small-strain plasticity to finite plasticity with multiplicative kinematics. *Eng. Computation*, 9:255–263, 1992.
- [25] V. S. Deshpande and N. A. Fleck. Multi-axial yield behaviour of polymer foams. *Acta materialia*, 49:1859–1866, 2001.
- [26] A. Dorfmann and R. W. Ogden. A constitutive model for the mullins effect with permanent set in particle-reinforced rubber. *Int. J. Solids Struct.*, 41:1855–1878, 2004.

- [27] T. Elsayed, F. Fraternali, A. Mota, and M. Ortiz. A variational constitutive model of polymers and soft biological tissues. *Division of Engineering and Applied Science, California Institute of Technology*, 2007 (preprint).
- [28] E. Fancello, J. P. Ponthot, and L. Stainier. A variational formulation of constitutive models and updates in non-linear finite viscoelasticity. *Int. J. Numer. Meth. Eng.*, 65:1831–1864, 2006.
- [29] N. A. Fleck and V. S. Deshpande. The resistance of clamped sandwich beams to shock loading. *J. Appl. Mech.-T. ASME*, 71(3):386–401, May 2004.
- [30] G. Franceschini, D. Bigoni, P. Regitnig, and G.A. Holzapfel. Brain tissue deforms similarly to filled elastomers and follows consolidation theory. *J. Mech. Phys. Solids*, 2006 (in press).
- [31] S. Fujiwara, Y. Yanagida, and Y. Mizoi. Impact induced intracranial pressure caused by an accelerated motion of the head or by skull deformation: an experimental study using physical models of the head and neck and bones of the skull. *Forensic Sci. Int.*, 43:159–169, 1989.
- [32] T. C. Gasser and G. A. Holzapfel. A rate-independent elastoplastic constitutive model for biological fiber-reinforced composites at finite strains: continuum basis, algorithmic formulation and finite element implementation. *Comput. Mech.*, 29:340–360, 2002.
- [33] E. E. Gdoutos, I. M. Daniel, and K. A. Wang. Failure of cellular foams under multi-axial loading. *Composite: Part A*, 33:163–176, 2002.
- [34] S. Govindjee and S. Reese. A presentation and comparison of two large deformation viscoelasticity models. *J. Eng. Mater. T. ASME*, 119:251–255, 1997.

- [35] S. Govindjee and J. C. Simo. Transition from micro-mechanics to computationally efficient phenomenology: carbon black filled rubbers incorporating mullins' effect. *J. Mech. Phys. Solids*, 40:213–233, 1992.
- [36] S. Govindjee and J.C. Simo. A micro-mechanically based continuum damage model for carbon black-filled rubbers incorporating the mullins effect. *J. Mech. Phys. Solids*, 39:87–112, 1991.
- [37] A. G. Gross. A new theory on the dynamics of brain concussion and brain injury. *J. Neurosurg.*, 15:548–561, 1958.
- [38] M. Grujicic, B. Pandurangan, K. L. Koudela, and B. A. Cheeseman. A computational analysis of the ballistic performance of light-weight hybrid composite armors. *Applied Surface Science*, 253:730–745, 2006.
- [39] W.N. Hardy, T.B. Khalil, and A.I. King. Literature review of head injury biomechanics. *Int. J. Impact Engng.*, 15:561–586, 1994.
- [40] G. A. Holzapfel. *Nonlinear solid mechanics: a continuum approach for engineering*. John Wiley and Sons Ltd., England, 2001.
- [41] G. A. Holzapfel and R. W Ogden. *Mechanics of Biological Tissue*. Springer-Verlag, Heidelberg, 2005.
- [42] T. J. Horgan and M. D. Gilchrist. The creation of three-dimensional finite element models for simulating head impact biomechanics. *Int. J. Crashworthiness*, 8:353–366, 2003.
- [43] E. A. C. Johnson and P. G. Young. The analysis of pressure response in head injury. In *C2006 Digital Human Modeling for Design and Engineering Conference, July 2006*, Lyon, France, 2006. SAE paper no. 2006-01-2368.
- [44] C. Kane, E. A. Repetto, M. Ortiz, and J. E. Marsden. Finite element analysis of nonsmooth contact. *Comput. Method. Appl. M.*, 180(1–2):1–26, 1999.

- [45] A. Katti, N. Shimpi, S. Roy, H. Lu, E. F. Fabrizio, A. Dass, A. Capadona Lynn, and N. Leventis. Chemical, physical, and mechanical characterization of isocyanate cross-linked amine-modified silica aerogels. *Chem. Mater.*, 18:285–296, 2006.
- [46] S. Kleiven. *Finite element modeling of the human head*. PhD thesis, Royal Institute of Technology, Stockholm, Sweden, 2002.
- [47] S. Kleiven and H. von Holst. Consequence of head size following trauma to the human head. *J. Biomech.*, 35:153–160, 2002.
- [48] J. E. Leestma. *Forensic Neuropathology*. Raven Press, N.Y., 1987.
- [49] C. Lin and M. Fatt. Perforation of composite plates and sandwich panels under quasi-static and projectile loading. *Composite Materials*, 40:1801–1840, 2006.
- [50] S. Lindgreen and L. Rinder. Experimental studies in head injury. ii. pressure propagation in percussion-concussion. *Biophys. J.*, 3:174–180, 1966.
- [51] C. Loop. Smooth subdivision surfaces based on triangles. Master’s thesis, Department of Mathematics, University of Utah, 1987.
- [52] V. A. Lubarda, D. J. Benson, and M. A. Meyers. Strain-rate effects in rheological models of inelastic response. *Int. J. Plasticity*, 19:1097–1118, 2003.
- [53] P. Lubock and W. Goldsmith. Experimental cavitation studies in a model headneck system. *J. Biomech.*, 13:1041–1052, 1980.
- [54] D. F. Meaney. Relationship between structural modeling and hyperelastic material behavior: Application to CNS white matter. *Biomech. Model. Mechanobiol.*, 1:279–293, 2003.
- [55] K. K. Mendis, R. L. Stalnaker, and S. H. Advani. A constitutive relationship for large deformation finite element modeling of brain tissue. *J. Biomech. Eng.*, 117:279–285, 1995.

- [56] K. Miller and K. Chinzei. Constitutive modeling of brain tissue: experiment and theory. *J. Biomech.*, 30:1115–1121, 1997.
- [57] K. Miller and K. Chinzei. Mechanical properties of brain tissues in tension. *J. Biomech.*, 35:483–490, 2002.
- [58] K. Miller, W. Taylor, and A. Wittek. Mathematical models of brain deformation behaviour for computed-integrated neurosurgery. In *Research Report of Intelligent Systems for Medicine Laboratory*. University of Western Australia, 2006, ISML/01/06.
- [59] R. A. W. Mines and A. Alias. Numerical simulation of the progressive collapse of polymer composite sandwich beams under static loading. *Composite: Part A*, 33:11–26, 2002.
- [60] W. Mock, Jr. (presenter) and J. Drotar. Penetration protection experiments using polymer materials. *ONR Workshop, St. Michael's, Maryland*, 2006.
- [61] J. Mohanraj, M. J. Bonner, D. C. Barton, and I. M. Ward. Physical and mechanical characterization of oriented polyoxymethylene produced by die-drawing and hydrostatic extrusion. *Polymer*, 47:5897–5908, 2006.
- [62] A. D. Mulliken and M. C. Boyce. Mechanics of the rate-dependent elastic-plastic deformation of glassy polymers from low to high strain rates. *Int. J. Solids Struct.*, 43:1331–1356, 2006.
- [63] A. M. Nahum, R. W. Smith, and C. C. Ward. Intracranial pressure dynamics during head impact. In *Proceedings of the 21st Stapp Car Crash Conference*, 1977. SAE paper no. 770922.
- [64] S. Nemat-Nasser and W.-G. Guo. Thermomechanical response of dh-36 structural steel over a wide range of strain rates and temperatures. *Mechanics of Materials*, 35:1023–1047, 2003.

- [65] G. S. Nusholtz, L. G. Glascoe, and E. B. Wylie. Modeling cavitation during head impact. In *Proceedings of NATO/AGARD Head Impact Conference, Paper 6*, 1996.
- [66] R. W. Ogden and D. G. Roxburgh. A pseudo-elastic model for the mullins effect in filled rubber. *Proc. R. Soc. Lond. A*, 455:2861–2878, 1999.
- [67] R. W. Ogden, G. Saccomandi, and I. Sgura. Fitting hyperelastic model to experimental data. *Comput. Mech.*, 34:484–502, 2004.
- [68] R.W. Ogden. *Non-linear Elastic Deformations*. Ellis Horwood, Chichester, UK, 1984.
- [69] M. Ortiz and J. Knap. Effect of indenter-radius on au(001) nanoindentation. *Phys. Rev. Lett.*, 90(22), 2003.
- [70] M. Ortiz and A. Molinari. Effect of strain-hardening and rate sensitivity on the dynamic growth of a void in a plastic material. *J. Appl. Mech.-T. ASME*, 59(1):48–53, 1992.
- [71] M. Ortiz and A. Pandolfi. Solid modeling aspects of three-dimensional fragmentation. *Eng. Comput.*, 14(4):287–308, 1998.
- [72] M. Ortiz and A. Pandolfi. A class of cohesive elements for the simulation of three-dimensional crack propagation. *Int. J. Numer. Meth. Eng.*, 44:1267–1282, 1999.
- [73] M. Ortiz and A. Pandolfi. Finite-deformation irreversible cohesive elements for three-dimensional crack-propagation analysis. *Int. J. Numer. Meth. Eng.*, 44(9):1267–1282, 1999.
- [74] M. Ortiz and A. Pandolfi. An efficient adaptive procedure for three-dimensional fragmentation simulations. *Eng. Comput.*, 18(2):148–159, 2002.
- [75] M. Ortiz, R. A. Radovitzky, and E. A. Repetto. The computation of the exponential and logarithmic mappings and their first and second linearizations. *Int. J. Numer. Meth. Eng.*, 52(12):1431–1441, 2001.

- [76] M. Ortiz and L. Stainier. The variational formulation of viscoplastic constitutive updates. *Comput. Method. Appl. M.*, 171(3-4):419–444, 1999.
- [77] A. Pawlak and A. Galeski. Plastic deformation of crystalline polymers: the role of cavitation and crystal plasticity. *Macromolecules*, 38:9688–9697, 2005.
- [78] S. J. Perles and N. B. Rewcastle. Shear injuries of the brain. *Can. Med. Assoc. J.*, 96:577–582, 1967.
- [79] M. T. Prange and S. S. Margulies. Regional, directional, and age dependent properties of the brain undergoing large deformation. *J. Biomech. Eng.-T. ASME*, 124:244–252, 2002.
- [80] H. J. Qi and M. C. Boyce. Stress-strain behavior of thermoplastic polyurethanes. *Mech. Mater.*, 37:817–839, 2005.
- [81] S. Reese and S. Govindjee. A theory of finite viscoelasticity and numerical aspects. *Int. J. Solids Struct.*, 35:3455–3482, 1998.
- [82] J. D. Reid and N. R. Hiser. Friction modeling between solid elements. *I. J. Crash*, 9(1):65–72, 2004.
- [83] S. R. Rodrigues, E. A. C. Johnson, and P. G. Young. The influence of projectile mass and velocity on the response of the brain to blunt impact. In *BioMECH 2003*, Rhodes, Greece, 2003.
- [84] C. M. Roland, J. N. Twigg, Y. Vu, and Mott P. H. High strain rate mechanical behavior of polyurea. *Polymer*, 48(2):574–578, 2007.
- [85] J. S. Ruan, T. B. Khalil, and A. I. King. Dynamic response of the human head to impact by three-dimensional finite element analysis. *J. Biomech. Eng.*, 116:44–50, 1994.

- [86] M. C. Saha, H. Mahfuz, U. K. Chakravarty, M. Uddin, Md. E. Kabir, and S. Jeevani. Effect of density, microstructure and strain rate on compression behavior of polymeric foams. *Mat. Sci. Eng. A-Struct.*, 406:328–336, 2005.
- [87] L. M. Schmitt. Theory of genetic algorithms II: models for genetic operators over the string-tensor representation of populations and convergence to global optima for arbitrary fitness function under scaling. *Theor. Comput. Sci.*, 310:181–231, 2004.
- [88] S. J. Strich. Diffuse degeneration of cerebral white matter in severe dementia following head injury. *J. Neurol. Neurosurg. Psychiatry*, 19:163–185, 1956.
- [89] P. Thoutireddy, J. F. Molinari, E. A. Repetto, and M. Ortiz. Tetrahedral composite finite elements. *Int. J. Numer. Meth. Eng.*, 53:1337–1351, 2002.
- [90] M. Übeyli, R. O. Yıldırım, and B. Ögel. On the comparison of the ballistic performance of steel and laminated composite armors. *J. Mater. Des.*, 28:1257–1262, 2007.
- [91] F. Velardi, F. Fraternali, and M. Angelillo. Anisotropic constitutive equations and experimental tensile behaviour of brain tissue. *Biomech. Model. Mechanobiol.*, 5:53–61, 2006.
- [92] P. Wambua, B. Vangrimde, S. Lomov, and V. Ignaas. The response of natural fibre composites to ballistic impact by fragment simulating projectiles. *Composite Structures*, 77:232–240, 2007.
- [93] J. Warren and H. Weimer. Subdivision methods for geometric design: A constructive approach. *Academic Press*, 2002.
- [94] K. Weinberg, A. Mota, and M. Ortiz. A variational constitutive model porous metal plasticity. *Comput. Mech.*, 37:142–152, 2006.
- [95] K. Weinberg and M. Ortiz. Shock wave induced damage in kidney tissue. *Comp. Mater. Sci.*, 32:588–593, 2005.

- [96] Q. Yang, A. Mota, and M. Ortiz. A class of variational strain-localization finite elements. *Int. J. Numer. Meth. Eng.*, 62(8):1013–1037, 2004.
- [97] Q. Yang, A. Mota, and M. Ortiz. A finite-deformation constitutive model of bulk metallic glass plasticity. *Comput. Mech.*, 37:194–204, 2006.
- [98] Q. Yang, L. Stainer, and M. Ortiz. A variational formulation of the coupled thermo-mechanical boundary-value problem for general dissipative solids. *J. Mech. Phys. Solids*, 54:401–424, 2006.
- [99] A. Yi, M. C. Boyce, G. F. Lee, and E. Balizer. Large deformation rate-dependent stress-strain behavior of polyurea and polyurethanes. *Polymer*, 47:319–329, 2006.
- [100] L. Zhang, K. H. Yang, and A. I. King. Comparison of brain responses between frontal and lateral impact by finite element modeling. *J. Neurotraum.*, 18:21–30, 2001.
- [101] L. Zhang, K. H. Yang, and A. I. King. A proposed injury threshold for mild traumatic brain injury. *J. Biomech. Eng.-T. ASME*, 126:226–236, 2004.
- [102] C. Zhou, T. B. Khalil, and A. I. King. A new model comparing impact response of the homogeneous and inhomogeneous human brain. In *Proceedings of the 39th Stapp Car Crash Conference*, 1995. SAE paper no. 952714.